Chair of Mineral Processing

Master's Thesis

Separation of copper from aluminum in an eddy current separator product by dry density separation

Muhammad Ali

June 2024

MONTANUNIVERSITÄT LEOBEN
www.unileoben.ac.at

AFFIDAVIT

I declare on oath that I wrote this thesis independently, did not use any sources and aids other than those specified, have fully and truthfully reported the use of generative methods and models of artificial intelligence, and did not otherwise use any other unauthorized aids.

I declare that I have read, understood and complied with the "Good Scientific Practice" of the Montanuniversität Leoben.

Furthermore, I declare that the electronic and printed versions of the submitted thesis are identical in form and content.

Date 03.06.2024

Signature Author
Muhammad Ali

Acknowlegdement

First and foremost, I would like to express my deepest gratitude to Allah Almighty for granting me the strength, knowledge, and perseverance to complete this thesis. Without His divine guidance and blessings, this work would not have been possible.

I am immensely grateful to my parents for their unwavering support, encouragement, and love throughout my academic journey. Their belief in me has been a constant source of motivation, and I owe all my achievements to their sacrifices and prayers.

I extend my heartfelt thanks to my supervisor, Dr Andreas Böhm, for his invaluable guidance, time, and support. His insightful feedback and mentorship have been crucial in shaping this thesis, and I am deeply appreciative of his commitment and dedication.

I would also like to thank the PROMISE consortium for providing this incredible opportunity. Their support has been instrumental in facilitating my research and enabling me to achieve my academic goals.

Lastly, I wish to express my sincere appreciation to the industry partner Scholz, for their engagement and collaboration in this thesis. Their practical insights and expertise have greatly enriched my work, bridging the gap between academic research and real-world application.

Thank you all for your contributions and support!

Abstract

The global shift toward green technology increases the demand for metals, which causes pressure on primary resources. To fulfil the demand for metals and to decrease the exploitation of primary resources, efficient recycling of metals is essential, but the issue is, that e metals are lost during processing or downgrade due to impurities as the presence of lead in copper is difficult to eliminate and it has to be downgraded. This thesis deals with the analysis of fluidized bed separator performance, which is a newly developed technology for the separation of different metals in scrap based on their density. For characterizing head grades, separation success, and the efficiency of separation, hand sorting, XRF sorting, and physical separation at the analytical grade of feed and product were done in order to evaluate the analysis effort and the increase the accuracy of particle-based analytical methods.

Within the experimental work, samples were taken from the fluidized bed separator, which separates the conductant product of an eddy current process into a heavier and a lighter fraction, based on its threshold density. The efficiency of the fluidized bed separator was elaborated by sink float analysis. The accuracy of hand sorting was analyzed for the copper and brass content in the heavier fraction using XRF analysis. Results indicate that fluidized bed separator was very efficient, which documents that the separator sufficiently enriches metals of a density higher than 4.5 g/cm³. Hand sorting based on visual inspection of the surface faces some limitations in separating the materials compared to XRF sorting. The work reflects the variance in materials recovery based on the employed analytical methods, highlights the strengths, and limitations of each analytical technique, and the amount of different constituents present in the feed samples.

Keywords: Fluidized bed separator, Hand sorting, X-ray fluorescence analysis, Density separation, copper recycling

Kurzfassung

Die weltweite Umstellung auf grüne Technologien erhöht die Nachfrage nach Metallen, was Druck auf Primärressourcen ausübt. Um die Nachfrage nach Metallen zu decken und die Ausbeutung von Primärressourcen zu verringern, ist eine effiziente Metallrecycling notwendig. Das Problem dabei ist jedoch, dass Metall während der Verarbeitung verloren geht oder aufgrund von Verunreinigungen wie dem Vorhandensein von Blei in Kupfer an Wert verliert.

Diese Arbeit befasst sich mit der Analyse der Leistung eines Wirbelschichtabscheiders, einer neu entwickelten Technologie zur Trennung verschiedener Metalle in Schrott basierend auf ihrer Dichte. Zur Charakterisierung der Ausgangsqualitäten, des Trennungserfolgs und der Effizienz der Trennung wurden Handsortierung, Röntgenfluoreszenzanalyse (XRF-Sortierung) und physikalische Trennung auf analytischer Basis von Aufgabe und Produkt durchgeführt, um den Analyse- Aufwand zu bewerten und die Genauigkeit partikelbasierter Analysemethoden zu erhöhen.

Im Rahmen der experimentellen Arbeit wurden Proben aus dem Wirbelschichtabscheider entnommen, der das leitende Produkt eines Wirbelstromscheiders in eine schwerere und eine leichtere Fraktion bei einer eingestellten Trenndichte trennt. Die Trennschärfe der Wirbelschichttrennung wurde durch Sink-Schwimm-Analyse der Produkte ermittelt. Die Genauigkeit der Handsortierung wurde für den Kupfer- und Messinggehalt in der schwereren Fraktion mittels XRF-Analyse analysiert. Die Ergebnisse zeigen, dass die Trenngüte des Wirbelschichtabscheiders sehr gut war, was beweist, dass er zur Anreicherung von Metallen mit einer Dichte > 4.5 g/cm³ verwendet werden kann. Die Handsortierung basierend auf der visuellen Kontrolle der Oberfläche weist im Vergleich zur XRF-Sortierung einige Einschränkungen auf. In der Arbeit wird die Schwankung im Ausbringen der einzelnen Stoffe auf Basis der unterschiedlichen Analysenmethoden diskutiert, die Stärken und Schwächen jeder Technik werden beleuchtet sowie die Menge der verschiedenen Bestandteile in den Aufgabeproben .

Schlagwörter: Dichtesortierung, Wirbelschichtabscheider, Handsortierung, Röntgenfluoreszenzanalyse, Kupfer-Recycling,

Contents

List of Figures

List of tables

1 Introduction

1.1 Background

With the transition towards a green economy, the clean energy transition, and the expansion of the digital industry during the last decades, the demand and use of the earth's natural resources have increased, which raises concerns about the over-exploitation of natural resources. To slow the pace of the depletion of virgin natural metals resources and our dependency on primary metals, a well-established circular economy is needed. As metal can be recycled infinite times, a circular economy is a useful approach to using metals efficiently and for an impactful circular economy, there is a need to maximize the recovery of materials from secondary streams and reuse resources efficiently. (Moraga et al., 2019)

Copper is the most critical metal that will have an important role in the energy transition and digitalization. The demand for copper in the EU will increase by 51 percent by 2050 and for the green transition, copper is required for every form of renewable energy. (Metals for Clean Energy: Pathways to Solving Europe's Raw Materials Challenge, n.d.)

For bringing valuable material back into the value chain, recycling is considered as most effective way. As recycling needs less energy is required in comparison with the primary production, and it also help to achieve sustainability by reduces CO2 emissions and waste management. Similar case is with the copper as it can recycle multiple times without losing its quality. Complex copper scrap streams like electronic waste, and automobile waste mostly contained other valuable metals that are part of these streams like nickel, tin, lead, gold, silver, and zinc. So, the recycling of copper drive the recovery of these valuable metals through sorting and subsequent metallurgical treatment. (The Importance of Recycling, n.d.) For an impactful circular economy and to fulfil the rising demand for copper, it is very important to develop highly efficient separation processes that help maximize the recovery of metal from secondary streams. The material flow of copper in Europe showed that 430kt of copper gets lost during the separation processes (Soulier et al., 2017) that could be recovered with the development of new separation technologies or by further development of the existing hybrid processes that have high separation efficiency.

1.2 Objectives

Materials in recycling streams are mostly bound in complex structures to fulfil various requirements. (Loibl & Tercero Espinoza, 2021) To ensure efficient use of recycled material in future applications, it is essential to recycle these materials with high purity. Additionally, the removal of any present impurities that can reduce material properties is also very important. This research is mainly focused on automobile and household scrap that primarily contains aluminium, copper and iron as materials of value along with other materials. The efficiency of recycling aluminium is dictated by the subsequent metallurgical processes that can only process a very limited amount of copper and iron because it is not possible to remove these elements by refining. Therefore, the purity of aluminium to the maximum extent is very important to avoid its down-

grading and to close the circular loop for a sustainable environment. (Raabe et al., 2022) Getting high-purity copper and iron through sorting will also increase the value of the scrap. As the density difference between aluminium and the other metals can be sufficiently exploited for separation, a newly developed density separator air-dense fluidized bed separator was used to separate the light metals (aluminium) from the heavy metals (copper, zinc, lead, and stainless steel). Experimental analysis was done on input material from Scholz Austria GmbH which was further separated by the fluidized bed separator developed by Blueline.

The outline of the research questions for this thesis are:

1. How efficient does the air-dense fluidized bed separator perform in separating different scrap metals based on density?
2. What are the comparative efficiencies of XRF, hand sorting, and physical separation methods like in metals and their alloys sorting?
3. What are the percentages of the different metals in automobile and household scrap in each stream within the separation plant?

1.3 Purpose of the Research

- Analysing the performance of the air-dense fluidized bed separators in the separation of different scrap metals like light metals (aluminium) from heavy metals (copper, zinc, and lead).
- Assessment of XRF, hand sorting, and physical sorting methods.
- Recommendation about the optimal position of the fluidized bed separator in the scrap processing plant.

1.4 Significance of the Research:

This thesis aims to provide a comprehensive analysis of scrap material composition and develop an optimized recycling strategy as well as compare different sorting and characterization methods. It will contribute to understanding the behaviour and efficiency of processes like hand sorting, XRF sorting, and fluidized bed separation to improve the purity of recovered metals and enhance the efficiency of scrap processing plants.

1.5 Methodology Overview

Quantifying the performance of fluidized bed technology in separating materials based on density and further refining the separation with XRF and hand sorting to analyze the percentage of different elements in scrap.

Comparative analysis of XRF and fire assay to validate the sorting results, especially for XRF performance.

Quantitative analysis of the samples from scrap processing plant streams to calculate the percentage of different metals.

2 Summary

The first part of the thesis is a literature review that mainly focuses on the physics of XRF analysis and fluidized bed separation to prepare the experimental part.

The experimental part was particularly focused on measuring the efficiency of fluidized bed separation by means of Blueline´s "Sort Fluid", a new technology in scrap processing that works on the principle of density separation. Additionally, the analytical methods hand sorting of constituents and point wise handheld XRF analysis were compared in the course of the property analysis of the samples from the fluidized bed sorter. This study was systematically done for the separation of the two main metals and their alloys, aluminum, and copper, present in the scarp, along with the fractional calculation of other metals and materials present in the scrap. In this work, the separation was based on the physical properties of metals, appearance, and elemental composition.

For testing the performance of the fluidized bed separator, the conductive material was used sampled from the eddy current separators in the "shredder heavy section" of Scholz Austria´s shredder plant at Laxenburg. The sort fluid separated the materials into two fractions - a lighter of a nominal density -4.5 g/cm³ and a heavier of a nominal density of +4.5 g/cm³.

To achieve the efficiency of the density separation in the two feed size classes -90 + 30 mm and – 30 mm + 16 mm sink float analysis was committed. In the bigger size fraction, the property analysis at densities 1.4 g/cm³; 2.5 g/cm³ and 3 g/cm³ was directly applied, while for the smaller size class the sample was further incremented into two sub size classes -30 mm +16 and -16 +10 mm.

As there was no material between the density classes 2.8 g/cm^3 (aluminum alloy) and 7.3 g/cm^3 (tin), the lighter fraction should be floating in the liquid with a density of 3.0 g/cm^3, and the heavier fraction should be sinking in the liquid with a density of 3.0 g/cm^3. Results showed that the fluidized bed was quite efficient in separating the lighter fraction from the heavier fraction and vice versa. For the size class -16mm +10mm, more than 99.3% of the particles in the heavier fraction had a density higher than 3.0 g/cm3 for all the samples analyzed, which means that the number of lighter particles in the heavier fraction was very low, and a similar trend was observed in the size fraction +16mm -30mm, in which 99.7% of the particles had a density higher than 3.0 g/cm3. In the lighter fraction, 99.8% of the particles had a density less than 3.0 g/cm3 in the size class -16mm +10mm, and 99% of the particles had a density less than 3.0 g/cm3 in the size fraction +16mm -30mm. In the size fraction -90mm +30mm, 99% of heavier the particles were reported as heavier fractions and 98% of lighter particles were reported as lighter fractions. A graphic representation of the findings in terms of partition curves is given in chapter 5 figures 19 to 23.

Hand sorting combined with hand-held, pointwise XRF analysis was committed on the copper and brass particles present in the heavier fractions to check the efficiency of hand sorting. All particles present in the heavier fraction in the density class greater than 3.0 g/cm^3 including copper and brass were analyzed by XRF. This analysis was used to draw a comparison between XRF analysis and hand sorting in terms of the head grade of total copper in the samples and to analyze the

upgrading of copper and its alloys in the heavier fraction. XRF analysis gave a reasonable estimate of the number of other metals present in the heavier fraction. The comparison showed that XRF was more efficient in material sorting than hand sorting, as hand sorting was affected by the size of particles, aesthetics of materials, coating or paint of the material surface, and the skill of the sorter. Mass balancing of copper and brass in the feed and the products showed that for the size fraction -30mm +10mm, copper was upgraded from 3% in the feed to 15% in the heavier fraction, whereas brass content was increased from 11% in the feed to 46% in the heavier fraction. No copper could be found in the lighter fractions. In case of the fraction -90mm +30mm, copper content was upgraded from 4% to 23%, and brass content was upgraded from 8% to 40%.

Additionally, the composition of the eddy current magnetic reject stream was investigated. The analysis was done with hand sorting to separate metals from the other fractions present in the sample. Although the sample represents the magnetics it is composed of stones, rubber, and residual material as non-metallic fractions and metal composites as metal fractions due to intergrowth with magnetic (iron) parts. Further discrimination of the metallic material in the sample was done with XRF, followed by single particle density measurement of all metallic fractions and stones to find a density relationship between the intergrown parts. The density relation showed that stones, aluminum composites, and magnesium composites had almost 100% of the particles in the density range of less than 4.0 g/cm^3, whereas other metals like iron alloys, copper composites, and zinc composites had 99%, 95%, and 98% particles, respectively, in the density class of more than 4.0 g/cm^3.

This research highlights the comparison of separation technologies to achieve high efficiency and effectiveness in scrap metal recycling processes. It also highlights that the integration of techniques like fluidized beds and XRF not only maximizes material recovery but also enhances the overall quality and value of recycled products.

3 Literature review

3.1 Scrap

Scarp generally denotes materials and products that cannot be used in any application, have reached their end of life, or cannot fulfil their intended purpose. In today's world, scrap serves as a significant sources of raw material especially metals depending on the lifespan of material. Scrap can be classify into three different categories depending on its origins:

Home scrap is classified as the leftovers from metal manufacturing processes. Composition of this scrap is well-known, so it got remelt within the production processes by the plant in which it was manufactured. Since its composition is well-known, it can be recycled infinite times.(Bowyer et al., 2015)

New scrap is classified as clean and new scrap that cannot be processed in its production plant due to a lack of machinery to process it. It is a high-quality and high-value material which is usually sold to other processing plants and the composition of this scrap is typically well-known. (Bowyer et al., 2015)

Old scrap refers to products, used by consumers that reached their end-of-life stage. They cannot be used further in any way. Compared to other types, old scrap requires much more treatment to be used as secondary raw material. As, it is often mixed with other materials or waste and unclean. Hence, for recycling, it needs proper processing. (Bowyer et al., 2015)

3.1.1 Copper and its Demand

Properties like electrical conductance, heat transfer, and corrosion resistance are the causes of copper demand and its recognition. The global transition towards green energy and digitalization results in rising demand of copper which could double by 2050, which is shown in the figure 1. The amount of copper used in 2021 was about 25 Mt and is expected to reach 53 Mt in 2050.(*The Future of Copper Will the Looming Supply Gap Short-Circuit the Energy Transition?*, 2022) In between these year, the higher demand will be from 2025 to 2035 from 31 Mt to 49 Mt the it will be peaked on 2050. During this period, the greatest demand will likely be in the energy sector field.

Figure 1 Forecast about the copper demand.

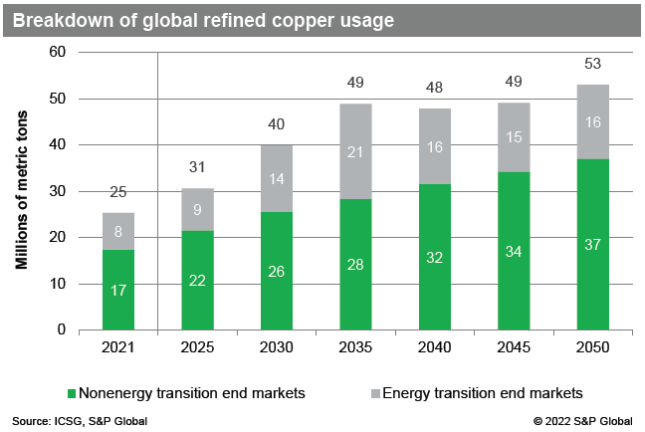

(The Future of Copper Will the Looming Supply Gap Short-Circuit the Energy Transition? 2022)

In Europe too, the demand for copper is expected to increase in the next three decades. According to the study by KU Leuven, the demand for copper in Europe will increase by up to 51%, under a scenario of Europe reaching zero-carbon dioxide emissions by 2050. To reach zero carbon dioxide emissions, the production of renewable energy sources and electric vehicles must increase which requires a rising amount of copper. (*Metals for Clean Energy: Pathways to Solving Europe's Raw Materials Challenge*, n.d.)

3.1.2 Copper scrap and its availability

As the demand for copper is increasing, available copper scrap recycling will also increase for recycling.. Copper can theoretically be recycled infinite times, which makes it sustainable and allows for practicing principles of circular economy. Copper recycling needs less energy as compared to its production from raw materials and also saves up to 86 % of CO_2 emissions. It also prevents waste build-up and landfilling.(*Metals for Clean Energy: Pathways to Solving Europe's Raw Materials Challenge*, n.d.)

Like others, copper scrap is also divided into the three types: new scrap from industry, old scrap from used products, and home scrap from manufacturers. Old scrap usually contains mixtures of materials which necessitates treatment prior to the recycling process. The availability of the scrap can be estimated from the world mass flow of copper, depicted in Figure 2.

Figure 2 Global Copper Stocks and Flows 2009 - 2018 (ICA/Fraunhofer, 2020)

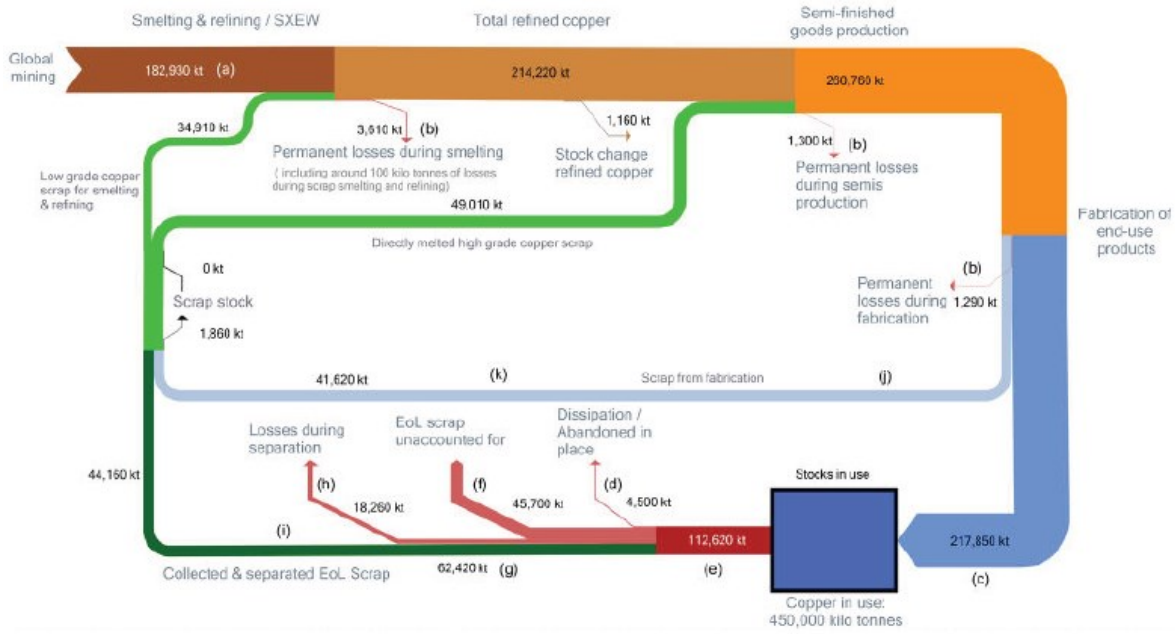

(*The Importance of Recycling*, n.d.)

This flow diagram shows that 214220 kt of total content the copper was produced globally, out of which 112600 kt was present as an end-of-end-of-life product, whereas 4500 kt of the copper scrap remained abandoned in place, 45700 kt remained unaccounted and 18260 lost during separation. From the total copper scrap, 44160 kt copper was collected and separated for recycling. The letter a indicates the input of smelting and refining metal, which is the total input of pure copper, b

indicates the products of copper, i indicates the amount of the recycled copper or output of the system and k indicates scarp from the industries.

Figure 3 Copper stocks and flows in the EU28 (2014)

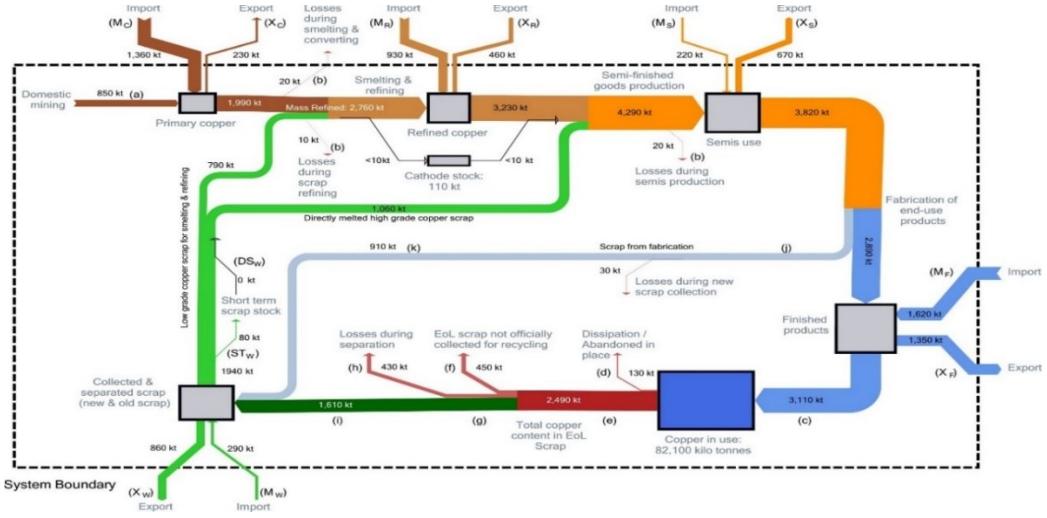

(Soulier et al., 2017)

In Europe, 2490 kt of copper products reached their end of life in 2014. From this amount of total scrap, 130 kt remained in place, 450 kt were not officially collected for recycling, 430 kt were lost during separation and only 1610 kt could be collected and separated for recycling.

Due to the average long life of copper and its alloy in different applications, availability of copper scrap is low compared to other metals. According to the World Bank Group, a 100 per cent recycling rate of copper would not be enough to fulfil the world requirement and can only cover up to 26% of the world's total copper demand. The rest will be fulfilled from primary sources by 2050. In Europe, the amount of secondary copper in relation to the total demand is about 45%, which is expected to increase to 66% by 2050. This however will require improvements in product design, scrap and waste collection process, sorting technologies for scrap processing, and the prevention of scrap leakage. The total demand in copper from recycling, domestic production, and import of primary metal will be increased from 4.3 Mt in 2018 to 5.9 Mt in 2050.

Figure 4 Estimation of copper recycling in the EU includes old and new scrap.

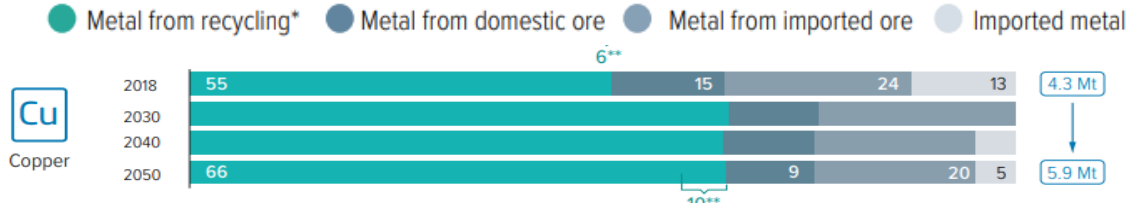

(*Metals for Clean Energy: Pathways to Solving Europe's Raw Materials Challenge*, n.d.)

3.1.3 Copper and its alloy scrap sources

According to the copper usage in the global economy, copper contributes mainly in five sectors that includes consumer electronics, the equipment industry includes military equipment, and coinage with a share of 31%. The building and construction industry has a share of 28%,

infrastructure makes 16%, the transportation sector makes 13% and industrial equipment has a share of 12%. Amount of the recovered copper from old scrap mainly influenced by the source of the end-of-life products, its location and condition.(Meskers et al., 2023a)

Figure 5 End users of copper globally

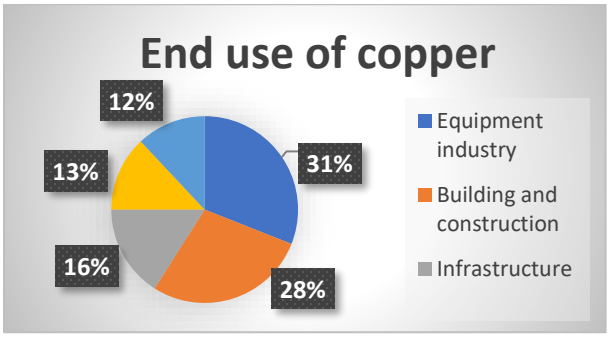

(Meskers et al., 2023a)

In Europe, the end use of copper can be broken down in a similar way to the global economy, as shown in Figure 6.(Meskers et al., 2023a)

Figure 6 The end user of copper in Europe

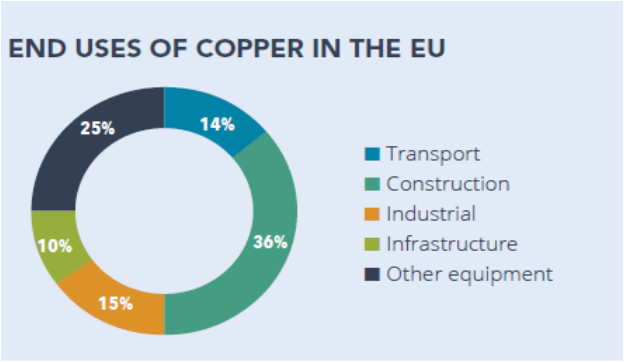

(*Metal Recycling Factsheet*, n.d.)

End-of-life (EOL) vehicles almost have about 0.8 per cent of copper, it does includes vehicle like ships, trains and planes. This share of copper is expected to increase in electric vehicles when it will become part of the scrap stream. Construction and demolition (C&D) waste also contain copper in the form of wiring, door handles, pipes, fittings, and frames along with the other items. This stream roughly containing 0.30% copper grade. (Meskers et al., 2023c)Waste from electrical and electronic equipment (WEEE) that is considered as the biggest source of old copper scrap containing domestic electrical appliances. Copper content in WEEE scrap ranges from 3 mass per cent to 21 mass percent depending on the product. Industrial electrical equipment waste (IEW) including power cable is relatively small in amount, but have copper content usually high: 5–80%. Industrial nonelectrical equipment waste (INEW) includes large transportation equipment ordnance, and other machinery, likely to have a small percentage. Municipal solid waste (MSW) is the most difficult waste stream to process as it has very low copper ranging from 0.05–0.20. (Meskers et al., 2023a)

3.1.4 Copper scrap alloys

Along with copper in pure form, many copper alloys are used in different applications. These alloys have various properties like corrosion resistance, strength, electrical conductivity, machineability, and wear resistance. (Michel, 2013)

The classification of the copper and its alloys is given in the appendix 2, table 53. Copper scrap is commonly separated from end-of-life products like cars, electronics and from municipal waste. Most of these scrap sources contain copper along with its alloys which increases the complexity of using such scrap and necessitates treatments such as sorting or metallurgical processing. The possible use of copper and its different alloys is shown in Figure 7 *Use of copper and its alloy family in different applications.* which reflects the complex composition of copper scrap.

Figure 7 Use of copper and its alloy family in different applications.

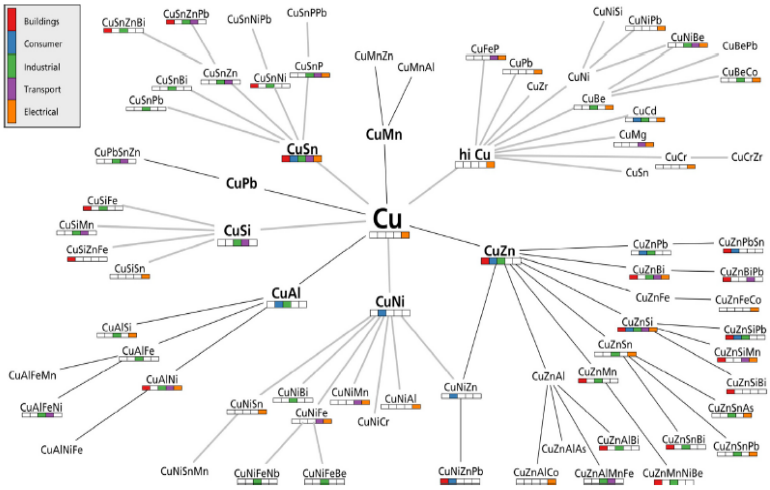

(Loibl & Tercero Espinoza, 2021)

3.1.5 Specification for copper and its alloy scrap

To use copper scrap for secondary processes, it is essential to comply with the specifications of scrap. These specifications primarily result from the requirements of smelters and refiners, which produce new copper from scarp as input material. These specifications are typically met by sorting end-of-life products. Sorting helps to raise the metal content and remove impurities from the scrap. Europe has linked the requirements for the trade in copper scrap and its alloys to the proportion of impurities. These specifications are taken from the report “End-of-waste Criteria for Copper and Copper Alloy Scrap”. (Muchová et al., n.d.) These specifications are given in the appendix 2, table 54.

According to the defined specifications of copper scrap by the European Union, some classes require high-purity copper, while others involve restrictions on some specific elements. This reflects the necessity of proper sorting of copper to reach a higher price for the scrap. (Muchová et al., n.d.)

3.1.6 Economical statistics of copper scrap

Globally, copper recycling market was about 66.95 billion USD in 2023 and it is expected to increase to 89.90 billion USD by 2030 due to increase in copper recycling and demand. European Union makes about 18% of the global recycling industry and Asia is the key player in the copper recycling market. A large amount of copper scrap is produced from electrical and electronic waste, construction waste and automotive waste. With the advancement in sorting technologies and an increase in copper prices due to the expectation of high demand and extraction of copper along with the precious metals from electrical and electronic waste, an increasing trend in copper recycling is expected. (Copper Scrap Market: Global Industry Analysis and Forecast, n.d.) Some industries play a major part in the recycling of copper as listed in Table 1.

Table 1 Copper Scrap Key Players

1. Aurubis
2. Commercial Metals
3. Sims Limited
4. HKS Metals
5. Jansen Recycling Group
6. Kuusakoski
7. Enerpat Group
8. European Metal Recycling
9. Olin Brass
10. Omni Source Corporation
11. Trademark Metals Recycling LLC
12. Mallin Companies
13. David J. Joseph
14. Mid-West Recycling
15. American Metal Recycling

(*Copper Scrap Market: Global Industry Analysis and Forecast*, n.d.)

3.2 Secondary processing of automobile scrap

The type of recycling process, required for each specific metal depends on a collection of many factors, such as accompanying materials, pre-processing and post-processing required for the extraction of the metals. Most pre-processing steps refer to the sorting steps required for the upgrading of the specific metal from other materials and post processing refer to the metallurgical processes that are essential to get the required composition. So, it can be used as secondary raw materials. (Reck & Graedel, 2012)

The secondary production chain of the automobile commonly follows a process that starts from the collection of waste, followed by dismantling, shredding, separation of different metals based on their properties, and to get the final product as separated metal or alloy as shown in Figure 8

Figure 8 Common flow chart of automobile scrap.

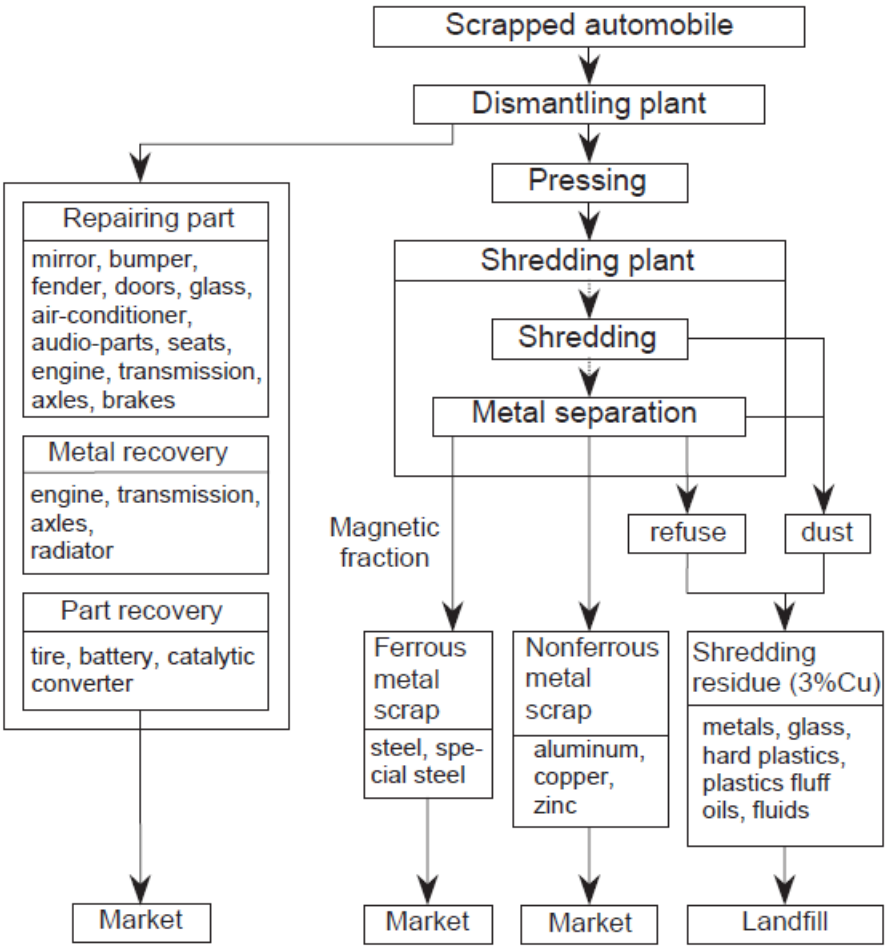

(M. E. Schlesinger et al., 2011)

3.2.1 Collection

In recycling processes, many complexities arise that may be related to the materials or that may arise from the collection phase, where different products of different origin are collected into a combined waste stream. The increase in complexity may dilute the economic value of a material

stream. Separate collection of different materials helps to reduce the complexity of the waste stream´s composition and thus reduces the required processing costs but in some cases, it can increase the transportation costs. While in some sectors complexity is independent of the type of waste collection, as is the case for automobile waste, in this case, proper treatment is required whereas if the material is separately collected and did not have complexity then it does not need any treatment like in the case of aluminum cans. (Loibl & Tercero Espinoza, 2021)

3.2.2 Comminution of automobiles

For simple products to be recycled, the properties used for separation depend strongly on particle size. Breakage of the material will result in the property distribution having distinct peaks. Similarly, the compounds (alloys in the case of metals) in a recyclable stream are firmly connected and distributed in various ways which affects their required particle size for proper separation. Particles may be mixtures of several compounds or consist of a single compound. Liberation is referred as metric of the single compound content. With the breakage, particle size gets finer, and the liberation will increase in a way typical of the processed material and method of particle size reduction. The size of breakage can be ranges from fines to coarse or can be achieve according to the define standards for the post processing. (Meskers et al., 2023b) For the comminution of scrap, a variety of machines and equipment are available, designed by different industries with different specifications. However, hammer shredders are the most frequent type of comminution machines used for automobiles. Whereas rotary shredders are used for the processing of plastic, light metals, wires and paper, the most famous rotary shredders are rotary cutters that have blades or knives (M. Schlesinger, 2013)

3.2.2.1 Hammer shredders

Swing-hammer shredders are widely used since they can handle a variety of input materials, from paper to aluminum scrap, old cars, and electronic scrap including small motors or even fridges. Here, hammers are the key compartments in the hammer shredder. During the shredding process of materials, the size reduction and volume compaction are accomplished mainly by impacts implied by the hammers. The working principle of comminution of metals in a hammer shredder can theoretically be characterized into four stages: the initial stage includes the interaction of materials and the hammer. The second stage is a collision stage in which severe deformation happens due to bending, torsion, and tensile force. The third stage is a grinding stage in which the impact against the wall becomes an important cause of further size reduction. The fourth and last stage is a separation stage in which the shredding material moves away from the cavity shell and the hammer. (Sander & Schubert, 2003)

Design analysis with numerical simulation method showed that for shredding recycled car bodies, the impact is more suitable than grinding due to higher shredding efficiency achieved by impact force. Hammerhead of the shredder with cutouts can reduce the wear damage and increase the shredding efficiency. Hammer with two side cutouts remained highly efficient and durable in industrial practice.(Zhou et al., n.d.) So, designing hammer shredders to achieve high impact is more favourable for automobile shredding.(Zhou et al., n.d.)

3.2.2.2 Purpose of shredding

Scrap typically contains different materials with different shapes and dimensions, the purpose of scrap comminution is to reduce the particle size as long as necessary, to produce particles that consist of only one type of material. The objectives of comminution are:

1. Get proper distribution of scrap size, which is essential for the subsequent steps
2. Increase the bulk density of the scrap
3. Liberate different components that form assemblies.

The main advantage of comminution is that it makes the removal of undesired possible. The available knowledge about non-brittle material comminution is poor, compared to the comminution of materials that are mostly present in primary mineral processing. Scrap streams show different comminution properties due to different material content than natural minerals, such as high ductility of metals, polymers, and inhomogeneity in shape and size. (Capuzzi & Timelli, 2018a)

3.2.2.3 Particle size distribution by screening

Shredded scrap materials have different particles which will further be processed to separate them into different streams according to their properties by different sorting methods. After shredding, particles are characterized by their size. Among all the particle shapes, the sphere is the only geometric form with well-defined unique size and diameter, but shredded particles mostly have other shape forms. All these shapes are mostly irregular and have different sizes. For them, most common method of sizing is sieving. The particle size in sieving is the characteristic size of an aperture the particle passes. Mostly, sieve surfaces have woven wire cloths with square apertures which means size is the length of the side of the square. Surface can also be made with round holes or punched squares. Settling velocity measurement of the particles is also used for size measurement that measurement could be in liquid or air. (Meskers et al., 2023c)

3.2.2.4 Characterization of shredded material by image analysis

For comminution evaluation properties like the size and mass distribution in different size classes, and the median values of the fragments dimensions are considered. Three main dimensions of a fragment, termed a, b, and c should be considered to calculate it´s size, and thereby the rule a > b > c must be fulfilled. Schubert et al defined that dimension b is indicative for the fragment size. They also defined that the evaluation of the deformation process can be done through the degree of compaction and the degree of bending. (Capuzzi & Timelli, 2018b; Sander et al., 2002a)

As, during the comminution of metals, deformation and breakage occur simultaneously, describing the results of comminution and characterisation of the products obtained a highly sophisticated task. Fragment size distribution determination by sieving has limited applicability according to Schubert et al, due to the irregular shapes and shape variability of the metal particles whereas the utilisation of image analysis has proven to be successful. In the project of the fragments at-least two dimension the largest a and medium b must be visible for analysis and care must be taken in

this regard. Determination of the fragment mass distributions is essential for many purposes like distinguishing the effects of deformation and breakage. (Sander et al., 2002b)

3.2.3 Sorting of automobile scarp

For the separation of the different material present in the scrap, sorting is done on the basis of chemical or physical properties of materials. Properties like density, colour, elemental concentration, magnetic properties, and many more are used for sorting. Physical treatments can be from manual sorting to sophisticated automated systems. Selection of the separation process is determined by the material properties, and its combination with other materials. (Meskers et al., 2023c)

3.2.3.1 Hand sorting

Hand sorting is an established dry separation process in which materials are separated based on their types, colours, and appearances. Recyclable materials are separated manually by skilled workers from undesired materials by putting each particle into separate bins for further processing. It is considered as the oldest sorting method and still popular today. Based on the difference in the colour of metals and depending on the skill of workers, different metals and even sometimes their alloys can be separated for further processing. (M. Schlesinger, 2013) In previous years, robots with machine learning processes have been used for separation of different materials from scrap streams. (M. Schlesinger, 2013)

There are several benefits and advantages of the hand sorting process in recycling operations.

- Low capital cost, more applicable in low-cost labour countries
- Unnecessary long-term training for workers is not required.
- High separation efficiency on some of the materials that have defined property differences, such as papers, plastics, metals, glasses, etc.
- Lesser contamination of recycled products

On the other hand, there are some difficulties and disadvantages of hand sorting in the recycling process:

- High labour cost in some countries make its expensive
- In some countries, standards are not defined or implemented resulting into unhealthy and unpleasant work environments that could affect workers
- The presence of dangerous sharp and toxic objects in the waste due to unstandardized collection
- Painted or coated materials can cause errors in the separation efficiency
- Slower process as its need more time to separate all the waste especially complex streams
- Worker's skill, good surface condition with obvious colour difference is required for efficient separation (Khan et al., 2022)

3.2.3.2 Air classifiers

Counter-current flow separation (CCFS) encompasses processes and equipment that separates material by the interaction with a regulated upward flow of fluid. The upward velocity of the fluid

is adjusted according to the settling velocity of the material in the dense fraction. If these processes use a liquid fluid (typically water) to separate the materials, they are termed as wet methods and if air is used as medium, they are termed dry process. Dry CCFS devices are also known as air classifiers. Due to their effectiveness in removing light contaminants such as dust, paper, glass polymer foils from metal streams, they are used for treating various types of solid waste. In automobile recycling industry, they are used for removing light loose particles and fibres from shredded automotive scrap. (Kaas et al., 2022)

Air classifiers mostly have a vertical tube that could be with one or more air injectors, positioned between central section and the tube's base. When the input material enters the tube, it encounters drag induced by the upward airflow which effectively lifts lighter particles upward, whereas denser particles settle downward against the air flow, due to gravity.

The most famous air classifier is the Zig Zag classifier, which is schematically depicted in Figure 9, with an upright rectangular channel of multiple sharp bends. This unique design leads to a range of particle collisions with the channel walls, that influence particle motion and slow down their movement. It results into long exposure of the particles to the air flow. (S. He Y., 2005)

Figure 9 Zig Zag Air classifier

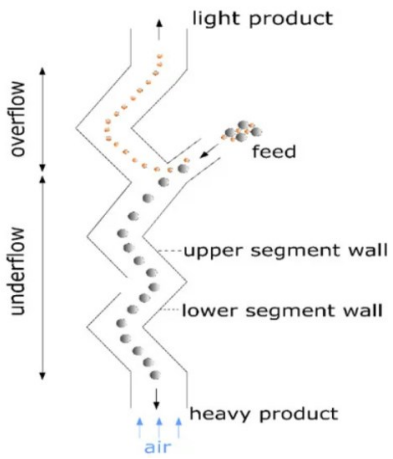

(Kaas et al., 2022)

Due to their effectiveness in separating significantly different density materials, air classifiers are very famous in different recycling industries like electrical and electronic waste processing, waste management industries, and automobile industries , such as plastics and metals. Their low cost and simplicity make them an excellent option for cleaning dense waste like metals especially when undesired organic matter and plastics is present.

However, they are highly sensitive to particle size variations, which ultimately limits their efficiency or necessitates additional investments to reduce particle size variations with prior stages of feed classification. (S. He Y., 2005)

3.2.4 Eddy current separator

Eddy current separation is a sorting method used for separating conductive from non-conductive particles. This involves feeding them to an alternative polarity magnetic field, generated by a rotating permanent magnet. This induces electric currents in conductive particles, known as eddy currents. Factors like size, particle conductivity, shape, and magnetic field strength influenced the magnitude of the induced currents. Secondary magnetic field produced around the particle due to induced eddy current opposes the primary magnetic field. (M. Schlesinger, 2013)When particles with the secondary magnetic field produced by induced eddy currents encounter a magnet with reverse polarity, a repulsive force is generated, resulting in the flipping, and deflecting of the particles from their original direction. The intensity of the induced eddy current affects the particles' degree of deflection . The electrical conductivity over density ratio (σ/ρ) of the particle is the key factor in eddy current separation. Materials with high conductivity and low density are easily deflected by magnets with alternating polarity. (M. Schlesinger, 2013)

Even though copper features a high electrical conductivity, due to its higher density a copper particle is less strongly deflected by the alternating fields. It is thus separatable from lighter metals, such as aluminum, when other operating parameters, such as grain size and particle shape are similar. Stainless steel is also affected but only slightly so.

Table 2 Deflection coefficient of metals and alloys

Deflection coefficient of metals/materials	
Metal / Material	σ/ρ ($M\mathbf{2}/\Omega$-kg 10^3)
Aluminum (Al)	13.0
Copper (Cu)	6.7
Silver (Ag)	6.0
Zinc (Zn)	2.4
Gold (Au)	2.1
Tin (Sn)	1.2
Iron (Fe)	1.2
Lead (Pb) 0.45	0.45
Glass 0.00	0.00
Plastics 0.00	0.00

(Yazici et al., 2011)

Hence conductive particles are separated on the basic of their deflection, which causes the particle to lift off from the end of conveyer belt, as depicted in Figure 10, the higher the value of σ/ρ, the higher the deflection of the particle. Non-conductors like plastic and paper remain unaffected by magnetic fields, so they simply follow a drop curve, induced only by the belt velocity at the end of the conveyer belt.

Figure 10 Eddy's current separation of materials

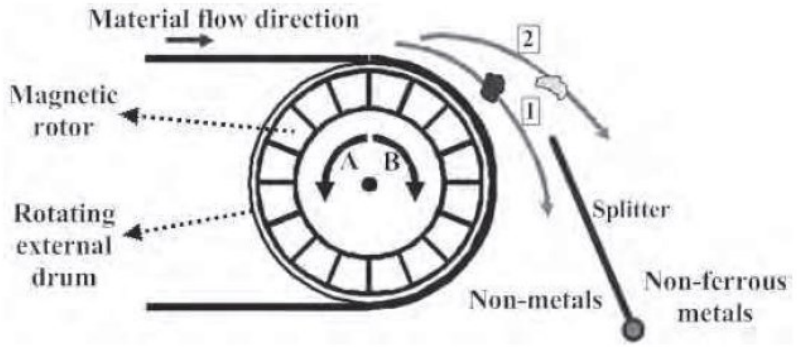

(Yazici et al., 2011)

3.2.4.1 Factor affecting eddy current separation.

Factors other than material that influence how far particles fly off:

- Field strength of the rotating magnetic field.
- Feed rate to the belt and rotation speed of the magnetic drum.
- Radius of the drum, a larger drum reduces throwing force if other variables remain constant.
- Particle size and mass - larger particles generate larger eddy currents, which in turn create greater secondary magnetic fields, that cause these particles to fly farther than smaller ones.
- With uniform-sized feed, eddy current separator works well.
- Particle shape as more eddy current is generated into nonspherical particle. So, flatty particle will fly farther than a ball bearing of equivalent mass (Jujun & Xu, 2012)

3.2.4.2 Limitation of eddy current separator

One of the biggest limitations of eddy current separators is the processable particle size. For the particles smaller than 1mm, the efficiency of the eddy current separator is low as the secondary magnetic field produced in smaller particles is weak and this limits the effect of particle deflection.. (M. Schlesinger, 2013)

3.3 XRF analysis

3.3.1 Spectroscopy and Atomic Structure

Spectroscopy is the study of the interactions between matter and electromagnetic radiation. In X-rays spectroscopy, X-ray are used as radiation source. It is quite commonly used characterization technique in the field of materials(Donais & George, n.d.). The theoretical foundation for the characterization is based on variations of X-ray fluorescence of different atomic structures. Each element in the periodic table has a unique atomic number (Z), which corresponds to the number of positively charged protons. In an atom, the number of neutron (which are neutral) and the number of negatively charged electrons are equal to the number of protons but in the case of isotopes number of neutron are different than electron and protons. At specific distance from nucleus,

electrons are present in their designated shells. Depend on the element, each element has specific number of electrons that are present in the shells as per their unique electron shell configuration. In spectroscopy, energy pattern that produced due to this unique configuration of electrons is measured. Electrons in the innermost shell, known as the K shell, are most strongly bound to the nucleus, due to the strongest attraction between the positively charged protons and the negatively charged electrons. Nucleus attraction on the electron decrease with the increase in distance of the shell from nucleus meaning that electrons in L shell, M shell, and so on are less tightly bound. This difference in attraction levels among the shells results in a variety of observable effects, related to the energy and location of electrons when electromagnetic radiation hits an atom.(Donais & George, n.d.)

3.3.2 XRF spectroscopy and its phenomena

XRF spectrometry involves the excitation of electrons from their orbital shells by high energy photons (X-rays) from an X-ray source. The specific energy of these photons can eject an inner electron from the atom, creating an ion which results in atomic instability. Stability is restored by filling the vacant spaces via outer shell electron transition which results in the release of excess energy. This release of energy from atoms can be done into one of two possible ways. One way is auger effect and other way is through fluorescence, where the atom releases characteristic X-rays, consisting of photons with energy levels specific of the element's identity. If the electron is remove from the K shell as a result of the energy carried by the photon and transition is happened from the L to the K shell, then energy level is referred as the Kα energy. In this, K is the representation of the shell from which electron expel and α referred to the transition from one shell further out to K. If the energy level of the inducing photon is different than the other transitions are also possible. (Donais & George, n.d.) If an electron falls from M to K, then it will be termed Kβ energy. Similarly, if the transition of an electron happens from M to L to fill the vacant space, then it will refer as Lα energy. The energy of these photons can be detected by a photon transducer. Energy data, collected by the transducer, can be used to identify the observed element according to its characteristic energy signatures. (Donais & George, n.d.)

3.3.2.1 Auger-effect

The other observable phenomenon, that can happen instead of fluorescence, involves the relaxation of an electron transition from the excited state back to its original shell without the emission of a photon. Due to the complex quantum-mechanical process, the energy released during the transaction is transferred to another electron within the atom. These emitted electrons carry a kinetic energy calculated by the following Equation (1).

$$E_{(Kinetic)} = E_{(Excited\ State)} - E_{(Ground\ State)} - E_{(Binding)} \quad (1)$$

In this phenomenon, there are three electrons involved. The first is the photoelectron which is emitted when the photon is absorbed. The subsequent relaxation process results in an outer electron filling the vacancy and causing a release of energy, which can be described in the following Equation (2).

$$E_{(Excited\ State)} - E_{(Ground\ State)} \quad (2)$$

This process involve the transaction of a third electron in the atom, binding with an energy of $E_{(Binding)}$.

However, quantum-theoretical models treat the relaxation and emission of the Auger-electron as a single process, denying the existence of separatable intermediate states during relaxation. The atom is left in a double-ionized state. Auger electron spectroscopy is used to measure the energy of electrons that emitted due to Auger phenomenon and can be correlated to the elemental composition of surface-near layers. The probability of photon emission (fluorescent yield) denoted as ω, and Auger-probability denoted as p (Auger), complement each other:

$$P(Auger) + \omega = 1 \quad (3)$$

Both, fluorescent and auger electrons are functions of atomic number and the affected (sub-)shell. For instance, ω_K is around 50% for Z = 32 and higher for heavier atoms. The Auger-probability significantly dominates over the emission of fluorescent radiation for light elements. For example, $\omega_K \approx 1.4 \times 10^{-3}$ for carbon and $\omega_K \approx 7 \times 10^{-4}$ for beryllium. The challenges encountered in the analysis of light elements by X-ray fluorescence (XRF) are largely due to the low count rates of photons, which results from the low fluorescent yields for these elements.(Burkhard Beckhoff, 2006)

3.3.2.2 Detectability of light elements by XRF spectroscopy

Not all the elements in the periodic table can produce detectable XRF signals. Hydrogen and Helium atoms, for example, feature only K shell electrons, so they cannot produce X-ray fluorescence as described above. In the case of lighter elements such as (Li, B, C, N, O), Auger decay processes are more highly favoured as compared to the fluorescence.(Donais & George, n.d.)

3.3.3 XRF Instrumentation

XRF instruments detect the energy or wavelength of the X-rays emitted by an atom, depending on the detector. In an XRF instrument, the first key component is the source of the X-rays used to initiate the excitation process. Several sources have been developed and used in XRF spectrometry instruments over the years. The most widely used X-ray source today is the X-ray tube. (Donais & George, n.d.)

3.3.3.1 X-rays tube

X-ray tubes feature a cathode, an accelerator voltage, a heating circuit, and an anode enclosed in a high-vacuum chamber, which is schematically depicted in Figure 11 The simple design of the X-ray tube. When the analysis is initiated, the cathode, usually made of tungsten filaments, gets heated by a heater circuit, which causes electron emission. Thereby the anode, usually a metal like Tungsten (W), Rhodium (Rh), or molybdenum (Mo) or Tungsten alloy, acts as the target for these electrons.

Electrons are directed towards the anode target using a Wehnelt electrode. To accelerate electrons towards the target, an electric field is created using negative potential to the cathode and grounding the anode. X-rays, emitted in all directions from the anode target, can only exit through a specially designed window and this window acts as a barrier between atmospheric pressure and vacuum

inside the tube. The configuration of this window can vary, based on the tube's application, thus specifying the emitted X-rays..(Burkhard Beckhoff, 2006)

Figure 11 The simple design of the X-ray tube

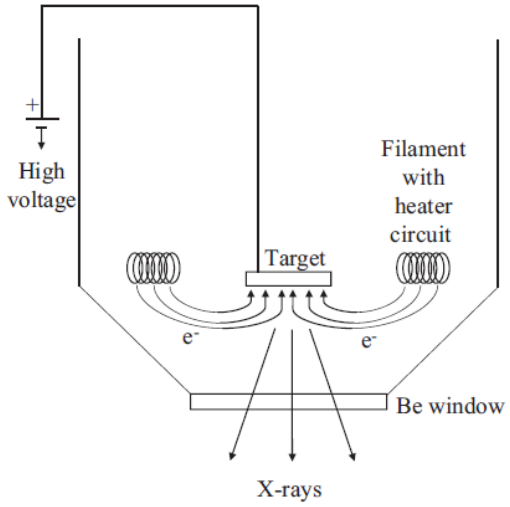

(Donais & George, n.d.)

There are different geometries of the X-ray windows are available. In side-window geometry, the exit window is aligned perpendicular to the axis of the tube. A thin beryllium film is often used in spectroscopic X-ray tubes to minimize X-ray absorption at low energies. Adjustment in the distance between the anode and the exit window can be resulted in increase in the intensity of the emitted X-ray beam. Some tubes employ a dual-anode geometry, with a thin layer of a lighter element covering a heavy element target, like rhodium. End-window geometry have a smaller anode-cathode distance, typically limiting the maximum voltage to around 60 kV which ultimately reduce the X-rays power. (Burkhard Beckhoff, 2006)

Transmission-anode X-ray tubes feature their target material as a thin layer located on the internal side of the beryllium exit window. Electrons hit the target at a right angle, and the excited photons pass through the target and the beryllium window in the same direction. These tubes are ideal for low-power applications, as the thin anode foils cannot handle high heat loads.(Burkhard Beckhoff, 2006)

3.3.3.2 Design of the Cathode

The current emission in X-ray tubes is controlled by the cathode's temperature, which in turn depends on the filament current. Current emission control through the cathode temperature requires emitters with very low heat capacity in the millisecond range for rapid cooling. Thin tungsten wires and foils are used in the shapes of a coil, helix, hairpin, ring, or flat meandering foil. If the applied current is below a certain threshold, no emission occurs. Conversely, large filament currents cause saturation of the anode current which depends on the height of the applied voltage. Temperature can reach up to 2300◦C, under extreme conditions. Therefore, cathodes at

such high temperatures are only switched on for a few seconds at a time, to realize short exposure times. The Wehnelt electrode is used to have proper shape of electron beam and to control the electron pattern in the vicinity of the filament.(Burkhard Beckhoff, 2006)

3.3.3.3 Design of the Anode

A standard anode consists of a thin target embedded into a massive copper body. Commonly used target materials are copper, molybdenum, and tungsten but metals like magnesium, aluminum, chromium, iron, nickel, rhodium, and silver are also used. To create high-intensity X-ray beams, rotating tungsten anodes are used. Rapid abrasion due to the high thermo-mechanical stress specially in the surface region is considered as the disadvantage of this technology. This results into "heel effect" due to fast decline of the X-ray intensity. Due to this, a part of the produced radiation is absorbed in the deeper lying layers of the anode, before it leaves the anode.(Burkhard Beckhoff, 2006) To limit this effect, an enhanced technology based on the Rhenium–Tungsten–Molybdenum composite material was developed. It contains a mixture of up to 10 % Re in the 1–2 mm thick W-cover which improves the elastic properties of the anode and considerably reduces the occurring abrasion. Adding a few percent of titanium and zirconium in the molybdenum and tungsten body nearly doubles the heat storage capacity of the anode due to improve in metallurgical properties which reduce the abrasion of the anode. (Burkhard Beckhoff, 2006)

3.3.3.4 Vacuum Envelope of X-Ray Tubes

X-ray tubes are positioned within a tube envelope for vacuum isolation and electric insulation. For this purpose, glass, metal, and ceramic are most used materials. Borosilicate glasses tubes have high specific resistance, capability to withstand temperature changes, and good dielectric strength are mostly used. These glasses combined with Ni‑CO‑Fe alloys are also used to ensure the necessary electrical contacts. (Burkhard Beckhoff, 2006)

Due to the high voltage, the anode and cathode tend to evaporate and form thin metal layers on the glass envelope, thus effecting the dielectric strength negatively. Use of metal for the central part of the glass envelope extend the lifetime of such tubes and avoid this effect by establishing a definite electrical potential. This can also remove a fraction of secondary electrons from the anode because the metal part is equidistant to the anode and the cathode and thus effects both electrodes. (Burkhard Beckhoff, 2006)

Metal-ceramic-composite tubes are also used, as these tubes have several advantages over standard glass tubes. Ceramics allows for easier mechanical treatment and can be manufactured with a high precision and metal tube parts can be joint to create a vacuum tight ceramic insulator. The surface conductivity of ceramic is low, resulting in short distances high voltages insulation. (Burkhard Beckhoff, 2006)

3.3.3.5 Modern X-Ray Tubes

Commercially available X-ray tubes can be roughly divided into the following three main categories.

Low-Power X-Ray Tubes with capillary optic, allow for focusing of X-ray beams onto small spots on a sample. Capillary optics' efficiency is effect significantly by the size of the source. It should

have the same dimension to the desired focal spot on the sample. The combination of a low-power high-brilliant X-ray tube with a poly-capillary concentrator enables achieving such high intensities making them indispensable for X-ray fluorescence microanalysis.(Burkhard Beckhoff, 2006)

High-power X-ray tubes are usually water-cooled with the maximum possible voltages for up to 60‑120 kV. The nominal focal spot can be normal, fine, long fine, or broad. These tubes are used in X-ray fluorescence analysis and X-ray diffractometry.(Burkhard Beckhoff, 2006)

Field emission cathodes logically follow the low-power X-rays tendency, utilizing the phenomenon of field emission with a cold cathode rather than thermo-emission. Conventional field emission tubes use a needle-shaped metal cathode to pull electrons from the needle tip out of the cold cathode using high potential between the cathode and anode. Metal cathodes are replaced with carbon-based cathodes that can be in the form of a single fibre, a bundle of fibres, or sharp-edge graphite nanotube: This replacement avoids the smoothness of the sharp tips and edges of cathodes that occur due to the bombardment from the residual ionizing gas on the metal cathode.

Triodes, similar in their design to field emission tubes, contain a cathode, an anode, and a gate electrode. Depending on the cathode design, the electron pulling potential can vary between 2 kV and about 150 V. A. This high voltage between the modulator and the anode creates the electric field which accelerates the emitted electrons. One special design uses a bundle of carbon fibres as the emitter, coated with a glass mantle and fixed inside the modulator case. Field emission cathodes do not require heating, thus simplifying the tube design and eliminating the need for a cooling system.(Burkhard Beckhoff, 2006)

3.3.3.6 Radioactive source

Radioisotope sources have been preferred for use in field instruments due to their high levels of consistency of radioactive decay that is independent of external variables like temperature, chemical-infected surroundings, pressure, and a power supply. These instruments have radioactive materials to use as sources which are shielded to direct radiation to the desired direction. In XRF, the excitation sources are mainly gamma radiation emitters, X-rays result from decay processes, which produce continuum or simple line spectra. Examples of radioactive sources include $^{26}Fe_{55}$ and $^{48}Cd_{109}$. Due to regional safety and security regulations, transport, storage, and use of such instruments depend on the type of radioisotope sources they feature. Hence, due to convenience and safety reasons, they have largely been replaced by tube sources. (Donais & George, n.d.)

3.3.3.7 Filter

Filters in XRF instruments enable the selection of the energy level of X-rays received from or transmitted to a sample. Filter can reduce interferences and background scattering of the X-rays, that help to have a more specific analysis for some elements. Filters are commonly used in XRF for optimizing the analysis. In some instruments, they have to be manually inserted, whereas some have filters mounted internally for computer-controlled selection. If the filters is placed between the X-ray tube and the sample then they are termed primary filters, but if they are placed between the sample and the detector then they know as whereas secondary filters. Filters typically consist of thin sheets of one or more elements, including copper (Cu), titanium (Ti), and aluminum (Al).

The choice of filter is determined by the elements, that should be detected in the analysis, which is closely linked to the given research question. (Donais & George, n.d.)

3.3.3.8 Detectors

Detectors are the materials that collect radiant energy (photon emitted by the sample) and convert it into an electrical signal that is subsequently displayed by the instrument´s software. Most commonly available detectors used in commercial XRF instruments are scintillation counters, gas-filled detectors, and semiconductor detectors.

Gas-filled detectors contain a chamber filled with an inert gas that becomes ionized when the photon from the sample enters the chamber. This ionization of the gas results in free electrons which in turn further ionize other atoms causing them to lose some of their electrons. These electrons move toward an anode, leading to a drop in voltage in the chamber. Decrease in voltage is detected as a pulse which then amplified and counted by a multichannel analyzer. Unabsorbed X-rays proceed through the exit window. (Donais & George, n.d.)

Scintillation detectors count flashes caused by the interaction of the photons, that are released by a sample, with a crystal. Theses modern detectors have an entrance window, a photomultiplier, a scintillation crystal, and a pulse-height analyzer. When the X-rays pass through the window, they produce a considerable number of visible light photons during interaction with crystal scintillators, such as sodium iodide (NaI) and cesium iodide (CsI)) and follows the de-excitation process. Photodetectors convert the photons into signals, which are then monitored by the pulse-height analyzer and processed by the software of the instrument. Scintillation detectors are based on materials with higher Z material and density. Hence, they can detect photon of a wide X-ray energy range. However, the energy resolution offered by these detectors is poor.(Burkhard Beckhoff, 2006; Donais & George, n.d.)

Gas proportional scintillation counters (GPSC) are effective detectors for energy-dispersive X-ray fluorescence analysis. In a GPSC, atoms are not ionized but instead produce a light pulse due to the de-excitation of gas atoms caused by an applied electric field. A suitable photodetector, like a photomultiplier tube is used to collect these secondary scintillation photons. Due to the generation of electron-ion pairs, signal amplification is achieved without spatial charge accumulation effects. GPSCs show remarkable performances for large detection areas in a 0.1‑100 keV X-ray energy range. (Burkhard Beckhoff, 2006)

Semiconductor detectors

These detectors work on the principle of electron-hole pairs creation due to X-ray interaction from a sample with the semiconductor crystal .(Burkhard Beckhoff, 2006) The primary electron created by the ionization due to X-ray interaction excites other bound electrons in the conduction band. These secondary electrons can, in turn, excite additional electrons, depending on their energy level. This produce electron-hole pairs that are collected at the device's electrodes which is in contact with the semiconductor made junction with it. The resulting voltage drop due to missing electrons occurs in pulses, which are processed by the multichannel analyzer. The energy level of the photon that reaches the detector influences the magnitude of the occurring pulse proportionally. This

energy level is characteristic of the element present within the sample. (Burkhard Beckhoff, 2006)The number of pulses produced reflects the energy of the original X-rays as well as the concentration of the excited element within in the sample. Some of the common semiconductor detectors are silicon drift detectors (SDDs), high purity germanium, Si(PIN) diode detectors, and lithium-drifted silicon (Li(Si)) . (Burkhard Beckhoff, 2006)

Si(PIN) diode are three-layer solid state detectors with a p-type layer, an intrinsic middle layer, and an n-type layer. High purity germanium, lithium-drifted silicon, and silicon drift detectors consist of high purity germanium and silicon, respectively. These semiconductor transducers can detect atoms across a wide Z range, but they require cooling for operation. Si(PIN) diodes and SDDs are Peltier cooled, which makes them more suitable for use in portable instruments as compare to the high purity germanium, and lithium-drifted silicon detectors that are liquid nitrogen cooled. (Donais & George, n.d.)

Silicon drift detectors are the recent technology that allows higher count rates than conventional Silicon drift detectors are the most recently developed technology that allows higher count rates than the conventional Si(PIN) devices. An electric field parallel to the surface is applied which result in ionized electrons by the X-ray detection that drift towards an anode at the centre. This field is created by numerous concentric ring electrodes etched into the surface. SDDs are mostly in PXRF instruments due to reduction in their production cost with technology development. (Corbeil, 2009)

All these detectors have a finite lifetime and need replacement after every five to ten years. (Donais & George, n.d.)

3.3.3.9 WAVELENGTH DISPERSIVE INSTRUMENTS

Wavelength dispersive XRF (WDXRF) is a method that separates emitted X-rays into bands of different wavelengths using Bragg diffraction on a single crystal or synthetic multilayer to disperse fluorescent X-rays. The spectrometer utilizes Bragg diffraction on crystals to disperse X-rays according to Bragg`s equation, given in Equation (4):

$$n\lambda = 2d \sin \theta \qquad (1)$$

Thereby, n denotes the reflection order, λ is the wavelength of incident X-rays, d is the lattice spacing of the crystal and θ is the incident angle. According to this equation, λ must be smaller than 2d. (Burkhard Beckhoff, 2006)

These instruments have an X-ray source, a sample holder, a monochromator that separate the wavelengths, and a detector. In these instruments, characteristic energy can be described either by using its wavelength or by equivalent energy. The light waves emitted from the sample after exposure to the exciting X-rays, enter a monochromator which consists of collimators and a crystal. Waves of light become parallel to one another by the collimator alignment before entering the crystal. The crystal then separates these wavelengths into bands according to their wavelengths. Rotation of the crystal, by use of a goniometer allows very precise variations in the angle between its face and the incident beam. Diffracted radiation then proceeds through the exit collimator to the detector, then both rotate together on a second goniometer. The crystal rotates at θ while the

exit collimator/ detector simultaneously rotates at angle 2θ with these rotations typically being computer controlled. (Burkhard Beckhoff, 2006; Donais & George, n.d.)

Crystals

Several types of crystals are used in WDXRF spectrometers based on their 2d value and resolution or reflectivity. WDXRF spectrometers are often equipped with temperature-stabilizing systems to stabilize the 2d value of the crystals structural lattice.(Burkhard Beckhoff, 2006)

Synthetic Multilayers

For the analysis of lighter elements with longer wavelength X-rays, dispersion materials with a larger 2d value are used. Langmuir‑Blodgett films such as lead stearate have been utilized for ultralight elements due to their high 2d values and very low reflectivity. Synthetic multilayers are more efficient than the Langmuir‑Blodgett film and are classified differently. Synthetic multilayers formed by multiple periodic stacks of refraction layers, which mostly consist of a heavy element, and transmission, or spacer layers. Refraction coefficients of the layers, the thickness ratio of the transmission layer and refraction layer, the sharpness of the layer boundaries, the total layer number, and many more can affect the operating properties of synthetic multilayers. (Burkhard Beckhoff, 2006)The optimal substance pair in synthetic multilayers should have low absorption and a large Fresnel coefficient, i.e., a significant difference in refraction indices between the spacer and the refraction layer. SMLs have several advantages over natural crystals, such as much higher physical stability or reflectivity, a smaller thermal expansion coefficient, and can suppress higher order reflections. The best choice of material for the spacer layer is mostly determined by the element to be analyzed. (Burkhard Beckhoff, 2006)

Detectors

Scintillation Counter and gas proportional counter detectors are most used in energy dispersive XRF spectrometers. (Burkhard Beckhoff, 2006)

3.3.3.10 Types of WDXRF spectrometers

WDXRF instruments can feature sequential or simultaneous designs.

In these instruments, detector can move either manually or automatically after receiving a sufficient signal to achieve the necessary precision for analysis.(Donais & George, n.d.) These instruments often have two different X-ray tube sources, one for shorter and one for longer wavelengths. These instruments analyze different elements one after another rather than simultaneously. (Donais & George, n.d.)

3.3.3.11 ENERGY DISPERSIVE INSTRUMENTS

EDXRF instruments measure the energy of photons of the X-rays emitted from the sample. These instruments feature an X-ray source, a sample holder and a semiconductor detector. However, they do not need a monochromator as they sort X-rays according to their respective energies, not their wavelengths. When X-rays, emitted from the excited sample fall on the semiconductor detector, it sorts them according to their respective energies using a multichannel analyzer and then displays the spectrum within a few minutes. The simplicity of their design makes them suitable for portable field equipment. In EDXRF instruments all data are collected simultaneously without ignoring

unexpected elements for the sample with the known composition having lower concentration of impurities. However, collecting highly accurate and precise data with EDXRF instruments is a challenge due to poor energy resolution and susceptibility peak overlapping, especially for medium and lighter elements. (Burkhard Beckhoff, 2006; Donais & George, n.d.)

3.3.4 Types of XRF instruments

3.3.4.1 Handheld Instruments

These instruments are designed to be used on-site to perform fast analyzes without the need for special sampling methods and elaborate sample preparation. They are always energy-dispersive and operate at short operating distances, usually less than 5mm. Therefore, the excitation powers can be considerably low, usually between 1–5 W is already sufficient. This allows operation, only powered by a rechargeable battery. The most common technologies for handheld ED XRF include miniature X-ray tubes, the silicon PIN detector, pulse processing electronics, and fast fundamental parameters algorithms. Silicon drift detectors are also used in handheld instruments which have improved their performance so far, that an analysis by a handheld XRF takes just a few seconds. (Crocombe, 2013)

As the sample area, that can be analyzed is a circle with only a few millimetres in diameter, the exact positioning is crucial and therefore supported by a video camera. The small, analyzed surface also limits the average composition of heterogeneous samples. For the samples that have variable composition at different section of the similar sample. (Leopold, 2021)

These instruments are mostly controlled by integrated minicomputers for quantification without intensive calculations. Additionally, the display size is too small for a qualitative analysis by spectral interpretation. Hence, these instruments are most used for the known material classes with standard-based quantification models. These material classes are tested to confirm the composition of the required elements in the sample. Otherwise, the material class must be determined by a so-called positive material identification (PMI) first, then the standard-based quantification is done in the second step. (Leopold, 2021)

Handheld instruments are usually used to identify alloys, both for scrap metals and material stored in inventories, ore composition in mining, samples at archaeological sites and the determination of toxic elements in consumer goods.

As, with the handheld XRF, measurements are taken in air without barrier, it can cause severe attenuation of the low-energy fluorescence X-rays. This results into less effective detection for lighter elements with a Z number below about Si (depending on instrument design). (Corbeil, 2009)

In these instruments, special attention must be given to radiation shielding and protection of the operator because of the use of open beams. (Leopold, 2021)

3.3.4.2 Portable Instruments

To avoid the problems associated with handheld XRF, such as inaccurate sample positioning and the risk of radiation exposure of the operator due to an open beam path, portable XRF instruments were developed. These instruments feature similar technical components as handheld instruments

but the path of beam is protected by enclosure. In these instruments, samples can be placed on a table which is a part of the casing, this enables longer measuring times. Portable instruments can have weights of up to 15 kg and thus be operated on-site with a battery supply. (Leopold, 2021)

3.3.4.3 Tabletop Instruments

Tabletop XRF instruments excite a relatively large sample surface, usually about 20–30 mm in diameter, which enables better averaging and higher X-ray fluorescence intensities. They require a homogeneous and flat sample surface for accurate results, which can be ensured by appropriate sample preparation. The X-ray sources are mostly X-ray tubes, depending on the specifications of the instruments and their applications. As these instruments are typically covered and always enclose the sample, there is no danger of radiation exposure by the operator. Depending on the specification, the sample chamber of some instruments can be equipped with a helium flush. This enables the possibility of analysing lighter elements usually down to Mg or Na, by reducing air absorption effects. These instruments can be equipped with either energy dispersive or wavelength dispersive detectors depending on the manufacturer. However, the detection of light elements by helium flush requires the use of a semiconductor detector, to efficiently capture the low-energy X-ray fluorescence emissions of lighter elements. Light elements can also be measured done gas filling of sample chamber, if the length of the air path of the fluorescence radiation is enough. Usually, this limits the downward analytical range to S or Ca. With the good accuracy, flexibility, and fast analysis of energy dispersive detectors, most tabletop instruments now feature EDS detectors. They are commonly used for waste or jewellery analysis, determination of toxic elements in consumer goods, and many other analytical tasks. (Leopold, 2021)

3.3.4.4 Instruments for Position-Sensitive Analysis

These instruments are used for micro-analysis by focusing the primary radiation beam on a small surface area of the sample. This is achieved using collimators that limit the radiation to a spot of about 0.2–2 mm in diameter. X-ray optics, like poly-capillary optics, can focus the beam to a size of less than 10 µm. The intensity of the required X-rays is the limiting factor for using collimators since it quadratically decreases with the diameter of the collimator. During operation, tube radiations from a large solid angle are collected by the X-ray optics and focused onto a small surface area on the sample. This results in the collection of sufficiently high fluorescence intensities from small sample surfaces. Therefore, the term micro-XRF is used for this type of X-ray analysis.

The sample is mostly excited from above, which helps to ensure correct sample positioning and allows analysing of irregular samples at different positions. These instruments are primarily used to determine the element composition or to non-destructively characterize a layered material system within finished products. To determine the mass fractions or layer thicknesses of a sample, it is scanned under the incident beam and the resulting data are displayed as linear or areal distributions. Analytical performance is dependent on excitation intensity, detector type, or measuring medium (air, vacuum) is like that of conventional energy dispersive instruments (Leopold, 2021)

3.3.4.5 Macro X-Ray Fluorescence Spectrometer

These instruments have an excitation source along with beam-shaping optics, a detector, and mostly an optical microscope at the measuring head. The measuring head is mounted onto a motor-driven carriage to move in front of the sample. This allows for each distribution analyzes and point measurements of large samples. However, in these instruments' measurements are taken in air, which limits the detectable element range. As, X-ray beam-guiding components are not covered, so it requires special precautions for radiation. These instruments are famous for the art objects investigation, especially when they cannot be moved. These instruments are known as macro-X-ray fluorescence (MXRF) spectrometers. (Leopold, 2021)

3.3.5 Metal and alloys XRF analysis

X-ray fluorescence spectrometry is a fast, reliable, and non-destructive method used in metallurgical facilities for alloy identification. Their portable design and battery-based energy supply make them feasible for use in the field. XRF manufacturers have combined the high speed and non-destructive nature of the analysis by these devices with an expert identification software that makes them suitable for use without extensive expert knowledge.

Carbon and low alloy steels are best analyzed using optical emission spectroscopy due to good detectability of light elements. XRF can be used for carbon and low alloy steels with wavelength dispersive detectors but is not accurate enough for such cases, therefore, OES is preferred(Leopold, 2021) For the remaining alloys, XRF analysis is preferable. In other alloys, non-metallic elements, such as carbon, oxygen, and nitrogen, are present in small fractions and mainly used to modify the physical properties of the steel. (Corbeil, 2009)

3.3.5.1 Typical Performance Data

Assessing the analytical performance of an XRF instrument is difficult because the performance, as well as the quality of data generated from the XRF, depend on many instruments' specific factors such as:

- Measurement geometries within the instrument, like relative distances and angles between the source, the sample, and the detector
- Detector characteristics, such as its energy resolution, thickness, effective surface area, and type
- Excitation source
- Measurement time
- Matrix of the material analyzed(Corbeil, 2009)

3.3.5.2 Software

In advanced XRF devices, calibration and data analysis are performed by software. Modern XRF analyzers not only feature empirical calibration software but also standardless calibration software. This software provides very versatile instrument calibration over 0–100% concentration range for each analyte without user participation or an extensive set of calibrants. This facilitates automated measurement, analysis, and decision-making processes.(Corbeil, 2009)

3.3.5.3 Sample Condition

The penetration range of X-rays is relatively short in metals, especially in steels, copper, and nickel-based alloys. The following Figure 12 shows the maximum depth penetration of the characteristic X-rays in a particular metal surface for five common alloys. These values are equivalent to the depth at which characteristics of the metals can still be detected.

Figure 12 Maximum penetration depth from characteristic X-rays of elements reach the surface of an alloy

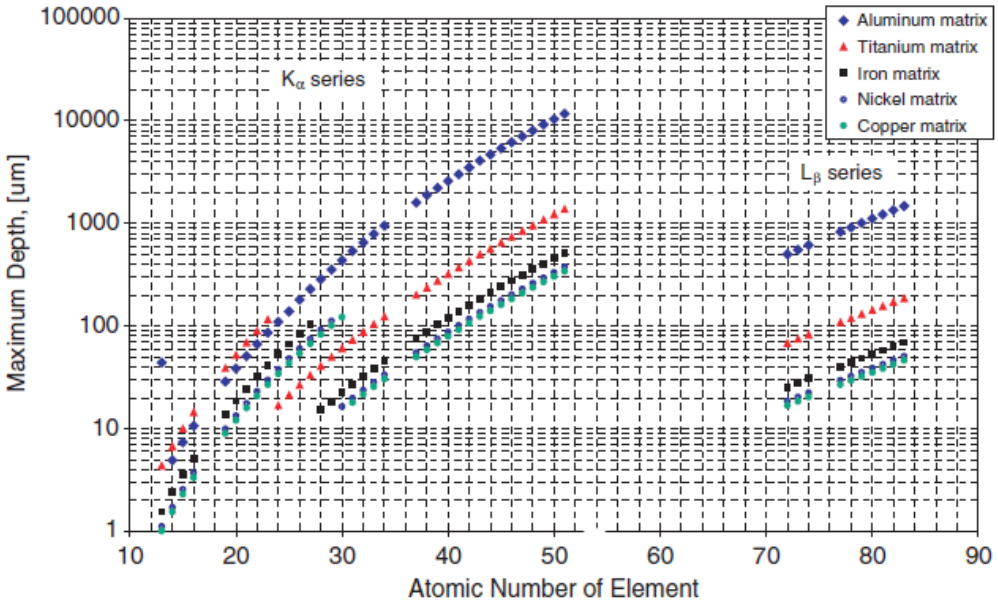

(Corbeil, 2009)

For the lighter elements, from Al to Sb, the analysis thickness can reach the up to 500 µm. For heavier elements, which are analyzed by L-lines, the thickness is only 70 µm and the depth of the low energy fluorescence radiation of carbon in iron is only about 0.3 µm. (Leopold, 2021)

In practical application, XRF analysis of alloys is considered as a surface technique, since such analysis process signals from just a few micrometres below the sample surface. This can result into conditions that:

The alloy is homogenised, and signal collect from critical penetration thickness is comparable with the grain size of the alloy then it will the accurate information about the composition.

Or X-rays may originate from surface elements which can distort the results of the analysis and give inaccurate information. (Corbeil, 2009)

For XRF analysis, the surface of the alloy being analyzed must be kept free of debris. Furthermore, it must be known whether alloys are plated or clad with another metal. The surface of the alloy should be clean and therefore ideally prepared by machining and etching, to obtain accurate results. If machining and etching is not possible, the sample can be prepared by palletizing chips from the sample. (Burkhard Beckhoff, 2006)

Surface preparation is very important, especially for an alloy analysis, as sometime alloys can have a film on its surface due to some soft metals like lead when rubbed. This will result in an inflated lead concentration. The thickness of the analyzed sample also effects the result. If the sample was thinner than the maximum penetration depth, the results would depend not only on the actual composition of the sample but also on its thickness, a very undesirable effect which impacts the intensity of the emitted X-rays. To prevent this effect, thin samples are staked to obtain a thickness that exceeds the critical penetration depth. Small objects like screws, pins or thin wires are mostly placed in a special sample cup to be analyzed. (Corbeil, 2009; Leopold, 2021)

For field analysis of alloys, shape and size of its front end that meets the analyzed instrument is also an important consideration. When analysing joints and welded alloys, the identities of joined parts and weld seams have to be known. In this case, the analyzer must have a front end, narrow enough to reach into the corner weld. The measuring aperture should also be shaped in such a way that it is possible to analyze only the weld seam. (Leopold, 2021)

3.4 Fluidization and fluidize bed

Fluidization is a process which occurs when a fluid, either gas or liquid, is used to lift the bed of granular materials upwards, making them behave like a fluid. At different gas velocities, this bed shows different behaviours. At a low superficial gas velocity, gravity primarily acts on the particles since the fluid passing through the bed has too low energy to lift the weight of the particles. Thus, the bed remains in a packed state as shown in Figure 13 A. The point at which gas velocity balance the upward drag force and the downward gravitational force termed “superficial gas velocity” or “minimum fluidization velocity”,. This results in the particles becoming suspended within the fluid and the bed of material is fluidized, as shown in Figure 13 B. At this stage of fluidization, the pressure drops across the bed, since the fluid flow balances the net weight of the particles, described in Equation (5).

$$\Delta P = M g_s / A_c \tag{5}$$

In equation (5), M_s represent the mass of the solid particles composing the bed, ΔP represents the pressure drop across the bed, , A_c represents cross sectional area of the bed, and g the gravitational constant. (Khawaja & Moatamedi, 2020)

Figure 13, 13A Fixed bed, 13B Minimum fluidization, 13C Smooth fluidization, 13D Bubbling fluidization, 13E Slugging (Axiel slugs), 13F Slugging (Flat slugs), 12H Lean phase fluidization

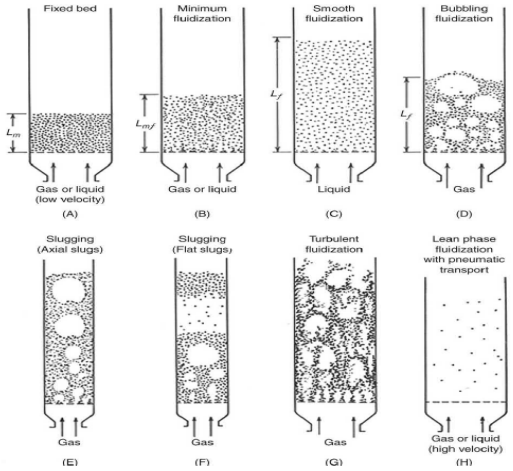

(Khawaja & Moatamedi, 2020)

During fluidization, superficial fluid velocity, particle density, particle size, and the fluid properties influence the material´s behaviour. If the fluidization media is liquid, once it passes through the granular particle, it will expand uniformly. This effect is termed "uniform fluidization" and is shown in Figure 13 C.

In the case of gas fluidization, small granular particles reach uniform fluidization at relatively low superficial velocities. However, larger granular material will start to bubble fluidize without first passing through the uniform fluidization state when the gas velocity exceeds the minimum fluidizing velocity. This is also shown in Figure 13 D. The frequency of this bubble formation and the size of bubbles depends on the particle size and density, the physical gas properties, and the height of the bed. Increases in fluid velocity through the bed result in increases in the bubble forming frequency and simultaneously the bubbles start to merge and form bigger bubbles. The point at which bubbles size reach the cross-sectional area of the bed, slugging is observed. Its depend on the particle properties, fluid properties and cross-sectional diameter of the bed. (Khawaja & Moatamedi, 2020) Axial slugs with round edges are shown in Figure 13E, with flat edges in Figure 13 F.

With a further increase in fluid velocity, the upper boundary of the bed suddenly becomes less distinct, which leads to a bubble break-up. This is turbulent fluidization, as shown in Figure 13 G. With further increase in gas velocities, a point reached when the particles moved out of the vessel, as shown in Figure 13 H. This phenomenon is known as lean-phase fluidization with pneumatic transport. (Khawaja & Moatamedi, 2020)

3.4.1 Characteristics of the Dense Air-Fluidized Beds

The separation performance of an air dense medium fluidized bed (ADMFB) strongly depends on the uniformity and the dynamic stability of the gas-solid fluidized bed. Therefore, design and operation parameters related to fluidized bed should be carefully controlled for efficient separation.

3.4.1.1 Theory of the Gas-Solid Fluidized Bed Used in Dry Coal Beneficiation

Liquid or gas fluidized bed separators are used to separate the material on the base of density. In the case of gas, particles are suspended into the bed like a fluid at a certain gas velocity to maintain a certain bed density. Like the separation in a liquid medium, ADMFB also separates particles by sinking denser particles to the bottom and floating lighter on the top surface with the reference of threshold density of ADMFB. The phenomenon of separation in such a bed can be explained by analysing different forces acting on the particles within the bed. These forces are the effective buoyancy force due to hydrostatic pressure distribution (F_b), the drag forces and gravity (F_{gr}). Drag force contributed to the relative motion between the particles to be separated and the fluidized bed particles (F_d) and between particle and gas (F_g). (Mohanta et al., 2013)According to Nguyen and Grace, due to the relative motion between particles and gas, drag force can be neglected. So. the following Equations (6) and (7) explain the resultant forces. (Chikerema & Moys, 2012; Mohanta et al., 2013)

$$F_r = F_{gr} - F_b - F_d \tag{6}$$

$$\frac{\pi}{6} d_p^3 \rho_p g - \frac{\pi}{6} d_p^3 \rho_{bed} g - C_d \pi \left(\frac{d_p}{2}\right)^2 \left(\frac{u_r^2 \rho_{bed}}{2}\right) = \frac{\pi}{6} d_p^3 \rho_p \frac{du_p}{dt} \tag{7}$$

Where u_r is the relative velocity of the spherical particles and fluidised particles, ρ_p is the density of spherical particles d_p is the diameter of the spherical particle, u_p is the falling velocity of the spherical particle, and C_d is the drag coefficient.

For the gravity settling in the fluidised bed, the falling velocity u_o reaches the terminal settling velocity u_t, at that point $\frac{du_p}{dt}$ become zero. Then the terminal velocity can be expressed as

$$u_t = \sqrt{\frac{4g(\rho_p - \rho_{bed})d_p}{3C_d \rho_{bed}}} \tag{8}$$

Particles can be ideally separated according to the bed density when u_r becomes equal to zero. When the density of particles becomes equal to the bed density, the position of the particles depends on their relative velocity and solids fluid medium. However, in practice material that has to be separated is a mixture of particles with different sizes and densities. (Chikerema & Moys, 2012; Mohanta et al., 2013)

The drag force has a different influence on the heavier feed particles than on the lighter particles, it contributes negatively to the heavier feed particles, which settle to the bottom and positively to the lighter input particles, which float towards the top surface of the bed. Thus, the optimum level of drag force that depends on the gas velocity is key for an efficient separation. Low gas velocity results in the misplacement of the low-density feed particles more intensely than of the high-

density particles. Similarly, high gas velocity causes the misplacement of high-density feed particles more intensely than the low-density ones. Therefore, the gas fluidization velocity must be chosen according to the optimal velocity for feedstock separation. (Mohanta et al., 2013)

3.4.1.2 Fluidize bed density

In a dense air fluidize bed (DAFB), stable dispersion fluidization and microbubbles are very important to achieve efficient separation conditions. A well distributed bed density in the three-dimensional space that will not change over time, along with low viscosity and high fluidity of the bed medium are the main requirements for an efficient bed separator. Equation (9) can be used for bed density calculation.

$$\rho_{bed} = (1-\varepsilon)\ \rho_p + \varepsilon\ \rho_a \quad (9)$$

Here ρ_p is the density of the solid particle (in g/cm^3), ρ_a represents density of the air (in g/cm^3), ρ_{bed} is the average density of the fluidized bed (in g/cm^3), and ε is the bed porosity in fractions. (Chikerema & Moys, 2012)

In the fluidize bed, when the air flow velocity is above the minimum fluidization velocity (u_{mf}; in m/s) in a suitable range, ε remains constant. Then ρ_{bed} is calculated according to Equation (10).

$$\rho_{bed} = (1-\varepsilon)\ \rho_p \approx W/LA \quad (10)$$

Here, L is the depth of the bed (in m), W is the total weight of fluidize medium solids (in kg) and A is the cross-section area of the bed (m^2). The constancy of the bed density depends on parameters like bed pressure drop, bed height, expansion ratio of bed, particle movement behaviour, gas flow rate, bed porosity, and properties of the feed and medium particles. (Chikerema & Moys, 2012)

3.4.1.3 Minimum Fluidization Velocity

The velocity of a superficial gas or liquid required to initiate fluidization is termed minimum fluidization velocity (Umf) . It is an important property of the fluidizing fluid and the particles, independent of bed depth. This velocity gives an indication of the minimum required flow rate to achieve fluidization. It can be calculated experimentally or predicted using different models present in literature. (Grace et al., 2020)

3.4.1.4 Measuring Umf Experimentally

The minimum fluidization velocity can be estimated by calculation but also be determined experimentally. There are several methods for measuring Umf .

Pressure Drop vs. Superficial Velocity Method

Most common and often regarded as the standard method is the pressure drop vs superficial velocity method. In this method, a sample of the bed particles to be tested is filled in a cylindrical column with a depth of at least 50 times the mean particle diameter and an inside diameter of at least 20 times the mean particle diameter. For the measurement, a medium distributor at the bottom should be perfectly horizontal and distribute the incoming gas or liquid uniformly with a pressure drop across the bed and it should not less than 10% of the bed weight-minus-buoyancy at the minimum fluidization velocity. One side of the column should relate to pressure measuring manometer and column should be equipped with pressure measurement a port just above the distributor. Whereas, the other side of the manometer should be left open to the atmosphere, in the

case the top of the vessel is open to the atmosphere or connected to a port opening in the freeboard region.(Grace et al., 2020)

Bed particles are poured into the column and the bed is fluidized for at least two minutes to create a steady surface, then fluid flow is reduced stepwise, and time-averaged pressure drop across the bed is recorded at each step until the velocity reaches the point where particles are in motion. Then, the superficial velocity of the fluid is increased stepwise, with the time-mean pressure drop recorded at each step. The pressure drop is then plotted against the superficial velocity in both cases. This plot, schematically shown in Figure 14 shows the graphical determination of U_{mf} at the intersection point of two extrapolated straight lines:

(i) The inclined line is fitted to the decreasing pressure within the packed bed portion of the pressure profile. This represents the pressure drop, resulting from the increase in fluid velocity before fluidization. First the pressure drops increase with the fluid velocity but then starts to decrease with the onset of fluidization.

(ii) The horizontal line correponds the flat section of the trace beyond the velocity at which fluidization began. Once the bed has become fluidized, the pressure drop remains constant even with the increase in fluid velocity. (Grace et al., 2020)

Figure 14 Graphical identification of the minimum fluidization velocity

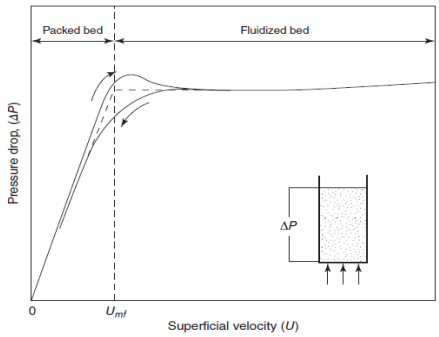

(Grace et al., 2020)

As shown in Figure 14, often a form of hysteresis is observed, due to difference in pressure drop profiles. Depending on the packing of particles, the pressure drop can be greater with the increasing fluid velocity, than for decreasing velocity curve. The preferred value for U_{mf} is on the decreasing-flow inclined line while finding the intersection. Checking magnitude of the pressure drop is also important. As identified if the pressure drop value is less than the difference of bed weight to the buoyancy per unit cross-sectional column area then fluid is not evenly distributed across the bed and bed is likely to be subject to substantial channelling.

Other experimental methods are also available to determine the minimum fluidization velocity.

Visual Observation: This method can only be used for transparent columns that involves the observing of bed with the increase in fluid velocity. It works best with uniformly sized bed particles. For a bed particle mixture with a broader size range, segregation will occur at low

velocities. So, it is recommended to fluidize the bed vigorously before decreasing the flow to the range of interest. (Grace et al., 2020)

Sinking of a Weight: For this method, a dense object is placed on the surface of the bed and the fluid velocity is increased until the object sinks. This method can result in the underestimation of U_{mf}, as the object can cause a higher local fluid velocity, leading to premature submersion. (Grace et al., 2020)

3.4.1.5 Umf Prediction Based on Particle and Fluid Properties

The point at which the drag force exerted by the fluid is balanced by the difference of bed weight to buoyancy of the particles, transition from packed bed flow to fluidization occurs which help in predicting minimum fluidization velocity. The gas velocity at which bed is packed, at that point drag and pressure drop through the bed are proportional to each other. So, the minimum fluidization velocity can be predicted, the point at which the pressure drop across a fixed bed becomes equal to the buoyed weight on the particles per unit cross-sectional area of the bed. (Grace et al., 2020)

For the prediction of the minimum fluidization velocity, more than 100 empirical and semi-empirical equations have been suggested in different articles. Mostly, they are functions of the dimensionless Archimedes (A_r) numbers and Reynolds (R_{emf}) numbers. (Anantharaman et al., 2018) Pressure drop for a fixed bed of a height *H*, voidage ε_{mf}, and particles of a diameter *dp* and sphericity ϕ can e calculated according to the well-known Ergun equation, shown in Equation (11).

$$-\frac{\Delta P}{H} = \frac{150 U_{mf} \mu (1-\varepsilon_{mf})^2}{(d_p \phi)^2 \varepsilon_{mf}^3} + \frac{1.75 \rho_f U_{fm}^2 (1-\varepsilon_{mf})}{\phi d_p \varepsilon_{mf}^3} \quad (11)$$

Here, at low Reynolds numbers, the first term on the right-hand side, that arises from viscous forces is dominant, whereas at large Reynolds numbers, the left-hand side term, corresponding to the inertial drag is dominant. (Grace et al., 2020)

Wen and Yu modified the Ergun equation and eliminated the dependence on voidage and sphericity (Anantharaman et al., 2018) by introducing the following approximations listed in the Equations (12)-(14).

$$\phi \varepsilon_{mf}^3 \approx 1/14 \; and \; \frac{(1-\varepsilon_{mf})}{\phi^2 \varepsilon_{mf}^3} \approx 11 \quad (12)$$

This can be solved for numerical values of ϕ = 0.67 and ε_{mf} = 0.47 and thus resulting in the following Equation (13) for U_{mf}.

$$U_{mf} = \frac{\mu}{\rho d_p} [\sqrt{\{33.7^2 + 0.0408 Ar\}} - 33.7] \quad (13)$$

Equation (14) gives, the Archimedes number Ar:

$$Ar = \frac{g \rho_f (\rho_p - \rho_f) d_p^3}{\mu^2} \quad (14)$$

Wen and Yu values are the most widely used ones. Other values are also calculated in literature but all these results in over- or under-prediction of minimum fluidization velocity, depending on

other factors like the particle sphericity and the determination of the average particle diameter. (Grace et al., 2020)

Equations (15) and (16) can be applied for both gas-fluidized and liquid-fluidized beds. These predictions are usually accurate within range of ±20% for liquid–solid fluidization and for Geldart group B and D particles gas–solid fluidization but for Geldart group A powders only about ±40%. Higher accuracy for Geldart group B and D particles than for group A powders is due to Van-der-Waals and other interparticle forces that are not included in the variables used to derive the Equation (15). Such forces are significant for group A particles due to the nature of these particles like sphericity and density, but for group B and group D solids, they play only a secondary role. For the prediction of U_{mf} , equation (15) is recommended, when experimental measurements are not possible.(Grace et al., 2020)

For small and large particles (low and high Archimedes numbers), Eq. (13) approaches the following limits:

$$U_{mf} = \frac{0.00061 \cdot g \cdot (\rho_p - \rho_f) \cdot d_p^2}{\mu} \quad (Ar \leq 10^3) \tag{15}$$

$$U_{mf} = 0.202 \cdot \sqrt{\frac{g \cdot (\rho_p - \rho_f) \cdot d_p}{\rho_f}} \quad (Ar \leq 10^7) \tag{16}$$

These two relationships are identical to the low and high Reynolds number limits for the terminal settling velocity of single particles, except for the numerical constants. (Grace et al., 2020)

3.4.1.6 Classification of Gas Fluidization Particles

Based on fluidization characteristics, Geldart classification is the most popular and useful one. He classified particles into four powder groups (groups A, B, C, and D) in terms of their overall gas fluidization properties.

Instead of alphabetical order, Geldart powder groups have increasing particle size order C, A, B, and D. (Grace et al., 2020)

Group C (cohesive): This group consists of fine particles with the particle diameter less than 20 μm. Due to small size, these particles have interparticle cohesive forces so, they do not fluidize readily. In these particles, due to van der Waals force, they dominate the hydrodynamic forces in the fluidized bed.

Group A (aeratable): In group A, interparticle forces between particles play an appreciable, but not dominant role. This group consists fine but easily fluidized particles with size range of 30–100 μm. When the upward gas flow reaches the minimum fluidization velocity through a bed of a group A material, it fluidizes smoothly. Additional flow leads to bed expansion, with the existence of the particulate fluidization regime before reaching the minimum bubbling velocity.

Group B (bubble readily): Group B materials has negligible interparticle forces. Bubbles form immediately with a little increase in the minimum fluidization velocity. Group B particles ranges from 100 to 800 μm with the of good quality fluidization, though less so than for group A powders.

Group D: This group contains coarser particles as compared to other groups. They can be fluidized but less smoothly than for group A and B powders. Geldart's classification was for air under at ambient conditions. (Grace et al., 2020; Scala et al., 2013)

Figure 15 Geldart classification of particles for air at ambient conditions.

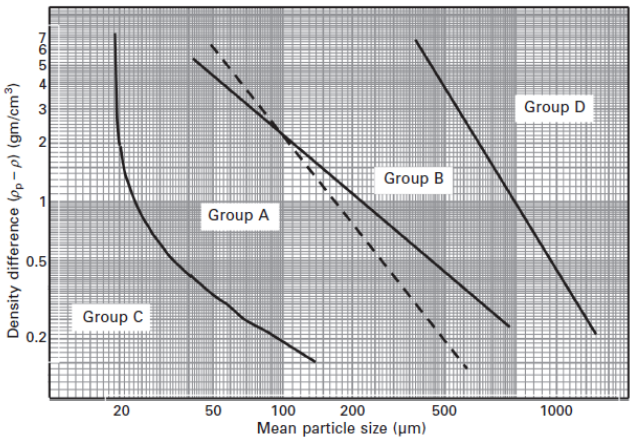

(Scala et al., 2013)

3.4.1.7 Fluid Properties

Properties of fluid that could be gas or liquid have influence on the fluidized beds properties. In the case of gas, these fluid properties are:

Density: Gas density effect the drag forces; higher density leads to increased drag on particles that results into earlier and more vigorous fluidization. Pressure effect directly to the density and temperature effect inversely. Roles of temperature and pressure on gas-fluidized beds can be assessed by assuming ideal gas behaviour as it gives a good approximation. (Grace et al., 2020)

Viscosity: For small particles, high viscosity causes greater drag but has a small effect for larger particles. Gas viscosity increases with the temperature increase but almost independent of pressure. (Grace et al., 2020)

Absorptivity: In case of gaseous components present in bed that can absorb on the particles surface and can affect van der Waals interparticle forces. This influences the properties of fluidized beds, especially for fine particles.(Grace et al., 2020)

3.4.1.8 Individual Particle Properties

Solid particles have several properties like density, size, shape, and distribution that play a key role in determining fixed bed properties. Voidage and roughness of the particles also have impact in fluid‑particle interactions.

Particle Diameter

Solid particles can never manufactured in the uniform particle size but can obtained using different physical techniques such as sieving, sedimentation etc. Particle size is important in fluidization processes and expressed as a diameter. For particle size analysis, sieving is commonly used. For nonspherical particles, the size of the particle can be approximate by the maximum direction in the

second of three principal (orthogonal) directions. Various sphere-equivalent diameters are also widely used to describe the diameter of non-sphere, the most appropriate average for fluidization is the Sauter mean:

$$d_{p32} = 6\, V_p / S_p \qquad (17)$$

where V_p is the particle volume and S_p is its exterior surface area. For a sphere particle, Sauter mean gives actual diameter. Particle size effect the fluid behavior due to interaction between particles and effect the minimum fluidization velocity as it is a parameter in the formula for minimum fluidization velocity. Geldart classification gives an indication of the effect of particle size on fluidization. (Grace et al., 2020)

Particle Shape

Most of the particles used are not completely, only a few particles are sphere. To get the degree of deviation from spherical shape, single "shape factor" can be used. Sphericity is the most common shape factor, defined as

$$\text{Sphericity} = \phi = \frac{\text{Surface area of a sphere of the same volume as the particle}}{\text{Actual exterior surface area of the particle}} \text{(Grace et al., 2020)}$$

Sphericity is 1 for sphere and value of sphericity decreases with the deviation from a sphere. It is difficult to measure actual exterior surface area of particles accurately in practice. So it can be estimated through a microscope by assuming that it is its two-dimensional analogue based on (2D) viewing particles, so it depend on its orientation:

$$\phi = \text{Circularity} = \frac{\text{Perimeter of sphere of the same projected area}}{\text{Actual projected perimeter of the particle}}$$

Both are not perfect indicators of complex shapes, but sphericity is most used by measuring the deviation from a sphere shape. (Grace et al., 2020)

Density and Internal Porosity

Density of the non-porous particles, ρ_p, is simply equal to the density of the material composed by the particles. For porous particles, the particle density is given by:

$$\rho_p = Material\ density \times (1 - particle\ porosity)$$

Whereas fraction of the internal pores in the particles is the particle porosity. In practice, bulk density is commonly determined and used. It is given in the equation (18):

$$\rho_{bulk} = \rho_p \times (1 - \varepsilon_{bulk}) \qquad (18)$$

where ε_{bulk} is the bulk voidage of the loose-packed bulk particulate material. Density of the particles influence the minimum fluidization velocity and fluidization behavior of the particles.

Surface Roughness

In a fluidized bed, when the particles slide over each other, smooth particles have less friction than the particles with the rough surface. So, in the case of rough surface, frictional forces can ultimately influence drag. Surface properties also affect the van der Waals forces, frictional forces, bulk voidage, and electrostatic interparticle and particle–wall forces particles which ultimately influence fluidize behavior. (Grace et al., 2020)

3.4.2 Effect of Particle size, shape and density on fluidized bed separation

For a fluidized bed, stable bed for maintaining the cut-off density and efficient separation is very important that mainly depend on the hydrodynamics of fluidized bed. Along with stability, optimization of the process is also very important that depend on operating parameters such as particles size, shape, density of the feed and medium particles used. Selection of the medium with the optimum properties like shape, density and size is important for efficient process and can be chosen. (Chikerema & Moys, 2012) The particle size, shape and density have great effect on the placement of the particles in the bed. In the case of coal separation, direct relationship is observed related to the positioning of particles have density less than the bed, as these particles float at different heights according to their relative density of the bed. The position of particles with the increase in densities and approaching that of the bed showed descending order. (Prusti et al., 2015)

Particle shape also effect the position of the particle in fluidized bed as in the case, coal with an increasing density and small projected area will move down gradually in the bed whereas larger particle with the increasing density rapidly fall to the bottom of the bed. Formation of dissimilar dead zones along the larger size and shape particles can result in a change in the particles' effective density and therefore their positioning in the bed. Even though, has a significant effect the on the separation efficiency of the air-fluidized bed, the particle size effect is very difficult to control. (Prusti et al., 2015) Three different particle shapes that contained flat, blockish, and sharp-pointed prism particles showed that due to smallest surface area to volume ratio, blockish particles are less subject to medium viscosity effects and separated better than flat and the sharp-pointed particles.(Chikerema & Moys, 2012)

(Prusti et al., 2015) observed that movement of the coal particles also influence with the particle shape. Triangular prisms particles generally have higher positions in the bed as compared to the cubic rectangular prism and spherical shapes that showed descending order, irrespective of size or density. Lower dead zone area that formed upon the triangular particles is the cause of their position in comparison to the other shapes in which spherical having the largest. A larger dead zone along the particles results into increases in the effective density of a particle due to the deposition of medium and accumulated fines in the dead zone. Due to this reason particles attain a heavier apparent weight and leads to a deeper position in the bed than expected (Prusti et al., 2015)

Particle size also effect the separation of the particles studied by Chikerema & Moys, 2012 determined that particle with the less diameter need different optimization parameters to have high separation efficiencies that the particles with high diameter. Yang et al., 2015 determined that decreasing particle size results into the decreasing performance of ADMFB due to the reduction in settling velocity and increase in the remixing effect caused by bubbles. Increase in bed to the particle diameter ratio, increase the minimum fluidization point due to the involvement of more prominent wall effect. (Rao et al., 2010)

As in the air fluidized bed separator, fluid behaves like a pseudo fluid, medium particles can accumulate on the particle surfaces thereby altering their apparent densities. It causes negative effect on the separation performance of the particle specially having near cut density as they might be recovered as sinks. All the main forces that include the buoyancy, gravitational, and drag forces acting on the fluidized bed particles are affect by the particle size, density and shape. (Chikerema & Moys, 2012)

4 Sample description and methodology.

4.1 Plant description.

The shredding plant of Scholz Austria GmbH located in Laxenburg operates with a focus on recycling a mix of automobile and electronic household scrap (White goods). It utilizes advanced mechanical and magnetic separation techniques to recover different materials efficiently, on the basis of their physical properties.

4.1.1 Equipment and Processes

4.1.1.1 Hammer Shredder

After the collection of automobiles and household materials, these materials are shredded with the hammer shredder to further process the material by physical separation. The basic purpose of the shredding is to liberate different materials so that these materials can easily be separated. Shredder works at the capacity of 30-40 tons/hour.

Function: Reduces the size of incoming scrap material. Particles larger than 90mm are reintroduced into the shredder.

4.1.1.2 Air Classifier

The air classifier is used to separate the material using differences in the terminal velocity on the bases of their size, density, and shape. The zig zag classifier separates very fine particles like dust, metal dust and separate them. These fine particles are then collected in filter system and disposed according to safety standards, the coarse and heavy material is further processed by magnetic separation.

Function: Separates dust and very fine scrap particles to ensure clean output, reduce airborne contaminants and collect fine particles to avoid their exposure to environment.

4.1.1.3 Magnetic Separator

Equipment: Magnetic drum separator to separate for ferro magnetic mostly iron material from non-magnetic particles, which are further processed in the so called “shredder heavy” part of the plant.

Function: Separates ferro magnetic materials from the shredded scrap efficiently but stainless steel remains in the system due to their low-magnetic nature.

4.1.1.4 Screening

Sizes: +90mm, -90/+30mm, +10/-30mm, and -10mm

Two types of screens a vibrating screen with circular excentric drive and a flip flop screen for the smaller size (10 mm) are installed. Function: Classifies shredded materials into different size fractions and preparation of the eddy current separation.

Particles larger then 90mm are recycled to the shredder for the further reduction.

4.1.1.5 Hand sorting

Function: Conducted on +90mm materials to manually remove non-ferrous metals such as copper and brass before re-shredding of the remaining +90mm fraction.

4.1.1.6 Eddy Current Separators

Function: Two units in operation to separate non-ferrous metals like aluminum and copper from the other non-conductive materials in different sized streams. To protect the acceleration belt at

the drum with the magnetic wheel from hazardous damage remaining ferromagnetic material has to be removed by a second “protection” magnetic separator before eddy current separation. The magnetic material is collected separately (RGW stream).
Details: One separator handles the +30/-90mm stream, and the other manages the -30/+10mm stream.

4.1.2 Material Collection at different plant position

Magnetic separation: Magnetic material separated from the air classified shredder discharge is collected as E40 material for iron recycling by EAF (iron scrap).
Sub-10mm Material: the -10mm fraction is currently collected without separation, although separation of contained metals is possible in the + 1 mm size range, as previous investigations proved.
Eddy current separation: Both installed eddy current separators produce two streams one of non-conductive materials known as “rubber” and one of conductive materials known as “aluminum”. The feed size fraction for the one separator is +10/-30mm and for other is +30/-90mm.

4.1.3 Material Flow

After the collection of automobiles and household scrap, it enters the hammer shredder for processing and then it passes through the air classifier. The underflow of the air classifier passes to the magnetic separator whereas the overflow is collected in the filter system as rejected dust. The magnetic separator then separates the E40 product which is magnetic ferrous material and passes the non-magnetic material to the screens. The screens classify the material into +90mm, -90mm +30mm, -30mm +10mm, and -10 mm fraction. After hand sorting of copper and brass from +90mm, the larger +90mm fraction is recycled to the shredder, while smaller fractions +10mm -30mm, -30mm +90mm are directed towards eddy current separators for separation. Eddy current separator separates materials into conductive fractions (aluminum) and non-conductive fractions (rubber). The fine fraction of -10mm is collected separately without processing. Along with the two products from the eddy current separator, a third fraction is also collected which mainly contains magnetic material. This fraction is separated due to the attraction of the particles towards the strong magnets of the eddy current separator.

Figure 16 Flowsheet of plant process

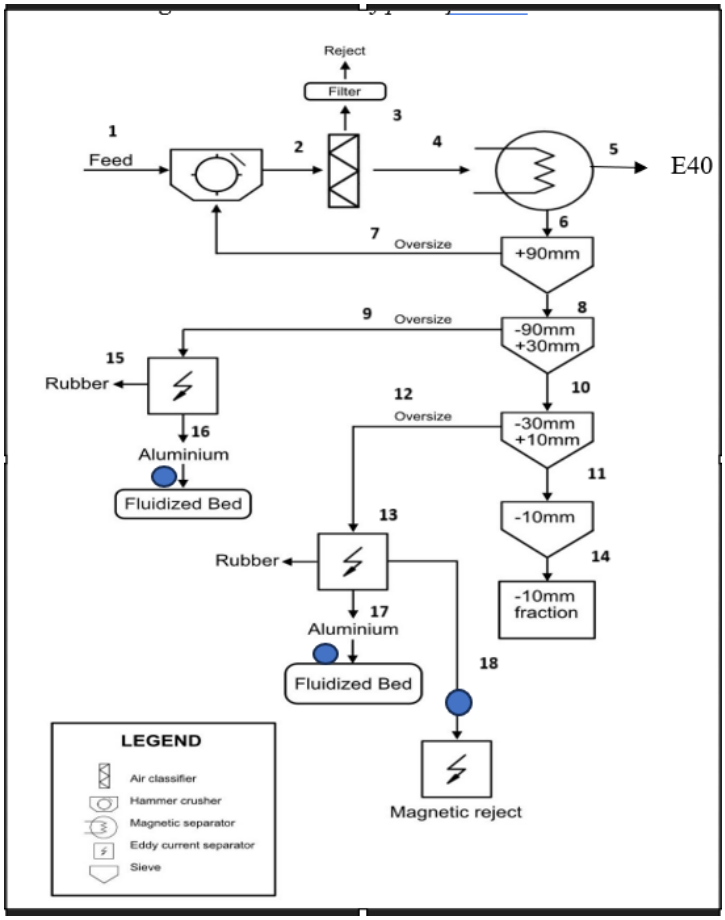

4.2 Samples Description

In this study, samples for the first experiments were taken from the aluminum stream of the size fraction +10mm -30mm and size fraction -90mm -30mm as well as eddy current magnetic reject stream was also sampled. These streams are represented with the number 16, 17 for aluminum and 18 for eddy current reject material in the Figure 16

4.2.1 Fluidized bed separated eddy current product sample

From Scholz Austria GmbH, eddy current separated aluminum fraction of the size class +10mm -30mm, and +30mm -90mm was sent to the Blueline where it was density-sorted using a dense air fluidized bed separator. The transport and sampling were done by Scholz Austria GmbH.

Fluidized bed separator separated the sample on the base of density differences in the feed material. The density separation was done using dense air fluidized bed separator with the threshold of 4.5 g/cm^3. After the separation, the light fraction should contain materials with the density of less than 4.5 g/cm^3 like aluminum and its alloys, magnesium and its alloy, and plastics. In contrast, the heavy fraction should have materials with the density higher than 4.5 g/cm^3 like iron, copper its alloys and zinc.

The sample separated with the dense air fluidized bed were transported to the Montan Universität, Leoben. The 4 samples comprised the two-density fraction +4.5 g/cm³ and – 4.5 g/cm³ in each of the size fractions -30/ + 10 mm and -90 + 30 mm,

Figure 17 Image a (lighter fraction -90mm +30mm), b (heavier fraction -90mm +30mm), c (lighter fraction -30mm +10mm), d (lighter fraction -30mm +10mm)

4.3 ” RGW” sample – a magnetic product of the protection magnet of eddy current separator -30 + 10 mm

The second sample was also taken from Scholz Austria GmbH shredding plant, but from a different stream in April. The stream is indicated in the Figure 16 as number 18. Sample mass comprised about 18 kg.

Figure 18 Image of the eddy current magnetic reject sample

4.4 Methodology

The systematic investigations comprised the method of property analysis combined with XRF assisted hand sorting. The property analysis adapted to the needs of the different samples followed a multidimensional approach. First, the property size was addressed by screen analysis, followed by magnetic analysis in size classes and classifying the non-magnetic fraction by sink float analysis.

4.4.1.1 Sampling

Samples were taken from both the heavier and lighter fractions of fluidized separated -30mm +10mm size class, 3,848g material was taken from a total of 96,500g sample of lighter fraction, and 3,291g was taken from a total of 27,600g sample in the heavier fraction.

Sampling was done by coning and quartering to ensure a representative and uniform sample composition.

After sampling, the lighter and heavier fractions were further divided by sieving into two sub-classes: -16mm +10mm and +16mm -30mm.

4.4.1.2 Separation Techniques

After sieving, magnetic separation was done for both size classes for extraction of magnetic materials from the sample. For this purpose, two hand magnets with the strength 0.1T and 0.7T were used. First magnet of 0.1T was used then a 0.7 T magnet was used. These magnets were used in a way that every particle in the sample was affected by its magnet force.

After magnetic separation, visible copper and brass was manually separated by hand sorting from each size class of the sample. Only brass and copper were hand-sorted from the heavier fraction of samples.

The performance of the fluidized bed sorter was analyzed, by materials' separation using sink float analysis. In this analysis, particles were classified into density classes using sodium polytungstate solution: less than 1.4 g/cm³, less than 2.5 g/cm³, less than 3 g/cm³, heavier than 3g/cm³. The

density of the liquids was checked with the aerometers whereas sodium polytungstate solution was used as density liquid.

Materials in the density range of 1.4 to 2.5 g/cm³ were identified as magnesium and its alloys, while material with the density 2.5 to 3.0 g/cm³ range was classified as aluminum and its alloys.

After density separation, samples were washed, dried at 100 °C, and weighed to back-calculate the fractions of materials in the feed.

X-ray fluorescence analysis was performed on each particle in the heavier fraction in the density class greater than 3.0 g/cm³ to further separate and determine the percentages of different elements including zinc, iron alloys, lead, and the efficiency of hand sorting based on physical appearance.

4.4.1.3 Validation

To check the consistency in the percentage of copper and its alloys along with the separation process, additional two samples from the heavier fraction were analyzed using same procedures.

All the masses obtained in the different property classes are listed in balance sheets given in tables in the results section and in the appendix.

4.4.2 Analysis of fluidized bed separated -90mm +30mm fraction

4.4.2.1 Sampling

Sampling was done similarly to the -30mm +10mm fraction, samples were taken from both lighter and heavier fraction. From lighter fraction, 7,055.97g from 67,300g was taken and from heavier fractions, 7,304g from 17,000g was taken.

4.4.2.2 Separation

Density was measured by Archimedes principle, whereas density separation was done in similar classes as previously described, and magnetic materials were isolated using the same method. For Archimede's density measurement, measuring balance with 0.01g precision was used for the low-weight particles whereas for the heavy particles due to the low limit of the measuring balance with the least count of 0.1 g, measuring balance with the precision of 1 g was used. For the calculation of the material, 0.997 g/cm³ density of the water was considered.

4.4.2.3 XRF and Hand sorting

Following density separation, hand sorting in a similar manner as done for 10/30mm fraction and XRF analyzes were conducted to determine the composition and percentage of copper, its alloys, and other metals.

4.4.3 Analysis of Eddy Current Magnetically Rejected Sample

4.4.3.1 Sampling and Preparation

19 kg of material was taken as a sample from the Scholz plant at stream number 18 as shown in Figure 16 Flowsheet of plant process and transported to Montan University Leoben. From 19 kg material, 9 558g were subsequently used for experimental analysis.

The sample was hand sorted and divided into material classes such as stones, metals, residual materials, and rubber, and then XRF analysis was done on the metal class for metal identification. The quantification of the classes of hand sorting by mass assigned to the individual types of material classes is given in table number 47 in the appendix.

4.4.3.2 Density Separation and Analysis

After XRF analysis, each metal class separated with XRF, and stones underwent density separation to get the density relationships among the different material classes. For the density separation, sample was further reduced by coning and quartering. The reduced masses of the sample used for density separation is given in the table number 49 in the appendix.

5 Results

To quantify the efficiency of air dense fluidize bed, the sample was analyzed on the basis of density. To analyze the efficiency of hand sorting and made a comparison between hand sorting and XRF, hand sorting was done only for copper and its alloys on the bases of their physical appearance and XRF analysis was done for all the material in heavy fraction in the density class greater than 3.0 g/cm³ along with the hand-sorted copper and its alloys. For the sample of eddy current magnetic reject material, hand sorting was done to analyze different materials in the sample, extended for metals by XRF and then density measurement was done to have density relation between metals and stones.

5.1 Hand sorting of size class of the sort fluid sample for copper and brass and efficiency check of the sorting results by XRF

The hand sorting of the sample was done for the copper and brass on the basis of their physical appearance and this separation was extended and confirmed by using XRF. For hand sorting, density class of greater than 3.0 g/cm³ was analyzed as there was no copper or brass particle in any other density class.

5.1.1 First sample -30mm +10mm

For the first sample, size fraction -16mm +10mm, the following results were obtained:

Table 3 Results for hand sorting copper and brass for 1st sample of -16mm +10mm size fraction.

1st sample -16mm +10mm	mass	Unit
Total brass	1571.68	g
Total hand-sorted fraction	1254.54	g
%percentage of hand-sorted brass	75.896	%
Efficiency of hand-sorted brass	95.082	%
Total copper	433.37	g
Total hand-sorted copper	424	g
%percentage of hand-sorted copper	97.837	%

The results were drawn using the total masses of copper and brass present in the samples that included classification by hand sorting and XRF. The hand-sorted brass was 76w% which means about 24w% of the particles could not be separated from the other fraction using hand sorting. Similarly, the percentage of the hand-sorted copper was 97.837 w% and almost all particles belong to copper class that means efficiency was 100%. The efficiency of the hand sort brass was about 95w% as also confirmed by XRF which means that 95w% hand-sorted particles were brass.

For the first sample, size fraction +16mm -30mm, the following results were obtained:

Table 4 Results for hand sorting copper and brass for 1st sample of +16mm -30mm size fraction.

1st sample +16mm -30mm	mass	Unit
Total brass	270.68	g
Total hand-sorted fraction	259.2	g

%percentage of hand-sorted brass	95.7588	%
Efficiency of hand-sorted brass	100	%
Total copper	98	g
Total hand-sorted copper	98	g
%percentage of hand-sorted copper	100	%

The percentage of the hand-sorted brass out of total brass was 96w% and the efficiency was 100% for this fraction as all hand-sorted particles considered as brass, were brass particles, confirmed by XRF. Similarly, the percentage of the hand-sorted copper was 100% and almost all particles belonged to the copper class.

5.1.2 Second sample -30mm +10mm

For the second sample, size fraction -16mm +10mm, the following results were obtained:

Table 5 Results for hand sorting copper and brass for 2nd sample of -16mm +10mm size fraction.

2nd sample -16mm +10mm	**mass**	**unit**
Total brass	2532.49	g
Total hand-sorted fraction	1790.58	g
%percentage of hand-sorted brass	70.207	%
Efficiency of hand-sorted brass	99.297	%
Total copper	697.64	g
Total hand-sorted copper	561	g
%percentage of hand-sorted copper	80.413	%

The percentage of the hand-sorted brass out of total brass was 70w% and the efficiency was 99.297% for this fraction. Similarly, the percentage of the hand-sorted copper was 80w% and efficiency was 100%. The low percentage of copper in this class was due to the aim of obtaining the copper with high precision, so the particles with some doubts were excluded.

For the second sample, size fraction +16mm -30mm, the following results were obtained:

Table 6 Results for hand sorting copper and brass for 2nd sample of +16mm -30mm size fraction

2nd sample +16mm -30mm	**mass**	**unit**
Total brass	580.21	g
Total hand-sorted fraction	409.31	g
%percentage of hand-sorted brass	70.5451	%
Efficiency of hand-sorted brass	100	%
Total copper	197	g
Total hand-sorted copper	197	g
%percentage of hand-sorted copper	100	%

The percentage of the hand-sorted brass out of total brass was 70.5w% and the efficiency of the hand sort brass was 100 % for this fraction. Similarly, the percentage of the hand-sorted copper was 100w% and almost all particles belonged to the copper class.

5.1.3 Third sample -30mm +10mm

For the third sample, size fraction -16mm +10mm, the following results were obtained:

Table 7 Results for hand sorting copper and brass for 3rd sample of -16mm +10mm size fraction.

3rd sample -16mm +10mm	mass	unit
Total brass	1506.91	g
Total hand-sorted fraction	1006.17	g
%percentage of hand-sorted brass	66.770	%
Efficiency of hand-sorted brass	100	%
Total copper	473	g
Total hand-sorted copper	447	g
%percentage of hand-sorted copper	94.5	%

The percentage of the hand-sorted brass out of total brass was 66.70w% and the efficiency of the hand sort brass was about 100% for this fraction. Similarly, the percentage of the hand-sorted copper was 97.837w% and almost all particles belonged to the copper class.

For the third sample, size fraction +16mm -30mm, the following results were obtained:

Table 8 Results for hand sorting copper and brass for 3rd sample of +16mm -30mm size fraction

3rd sample +16mm -30mm	mass	unit
Total brass	195.51	g
Total hand-sorted fraction	169.9	g
%percentage of hand-sorted brass	86.7474	%
Efficiency of hand-sorted brass	100	%
Total copper	142	g
Total hand-sorted copper	142	g
%percentage of hand-sorted copper	100	%

The efficiency of the hand-sorted brass was 100 % and the percentage of the hand-sorted brass out of total brass was 86.7w%. Similarly, the percentage of the hand-sorted copper was 100w% and almost all particles belonged to the copper class.

5.1.4 Sample -90mm +30mm

For the sample with size fraction -90mm +30mm, the following results were obtained:

Table 9 Results for hand sorting copper and brass for a sample of +30mm -90mm size fraction

Sample -90mm +30mm	mass	unit
Total brass	2954.36	g
Total hand-sorted fraction	1886.73	g
%percentage of hand-sorted brass	63.86	%

Efficiency of hand-sorted brass	100	%
Total copper	1714.23	g
Total hand-sorted copper	1714.23	g
%percentage of hand-sorted copper	100	%

The percentage of the hand-sorted brass out of total brass was 63w% and efficiency was 100%. Similarly, the percentage of the hand-sorted copper was 100w% and almost all particles belong to the copper class.

5.2 Addition XRF analysis of fluidized separated samples

After hand sorting, XRF analysis was conducted for each sample to analyze the percentage of copper in the hand-sorted copper, the percentage of copper in its alloys like brass, and the presence of different elements in the sample. Separation was also carried out for common elements like zinc and its alloys, lead, and iron with the other elements separated as other fractions. For all samples, the non-magnetic heavy fraction with the density greater than 3.0 g/cm³ was analyzed including hand-sorted copper and brass.

5.2.1 First sample -30mm +10mm

For the first sample, size fraction -16mm +10mm, the following results were obtained:

Table 10 XRF separated fractions from the first sample -16mm +10mm fraction.

Elements present	**g**	**XRF Cu (%)**
Mass of hand-sorted copper confirmed by XRF	424	90.06
Mass of zinc present in the sample	735.8	
Mass of iron present in the sample	48.47	
Additional mass of copper identified by XRF	378.83	51.02
Mass of lead present in the sample	8.37	
Additional mass of copper identified by XRF	9.37	90.85
Hard sort brass fraction confirmed by XRF	1192.85	53.89
Mass of other fractions present in the sample	196.45	
Mass of other fractions present in the hand-sorted brass	61.69	
Total mass	3055.83	

The largest amount of the metal present in the heavier fraction sample was copper and its alloys which was about 1571.68g of brass and 433g of copper. The second largest fraction present in the sample was zinc and its alloys which were about 735.8g. Whereas, iron, lead, and other fractions were not significantly present in the sample. The copper content analyzed by XRF was hand-sorted brass contained 53.89% copper, other than hand-sorted brass contained 51.02% copper whereas copper content given by XRF in the copper fraction was 90.06%.

For the first sample, size fraction +16mm -30mm, the following results were obtained:

Table 11 XRF separated fractions from the first sample +16mm -30mm fraction

Elements present	**g**	**XRF Cu (%)**
Mass of hand-sorted copper confirmed by XRF	98	90.85
Mass of zinc present in the sample	188.82	
Mass of iron present in the sample	5.2	
Additional mass of brass identified by XRF	11.48	43
Hard sort brass fraction confirmed by XRF	259.2	50.01
Mass of lead present in the sample	38.4	
Total mass	601	

The largest amount of the metal present in the heavier fraction sample was copper and its alloys which was about 270.68g of brass and 98g of copper. The second largest fraction present in the sample was zinc which was about 188.82g. Whereas, iron, and lead were not significantly present in the sample and there was no other fraction than the listed elements. The content of copper given by XRF in the hand-sorted brass was 50.01%, in other than hand-sorted brass it was 43% whereas copper content given by XRF in the copper fraction was 90.85%.

5.2.2 Second sample -30mm +10mm

For the second sample, size fraction -16mm +10mm, the following results were obtained:

Table 12 XRF separated fractions from the second sample -16mm +10mm fraction.

Elements present	**g**	**XRF Cu (%)**
Mass of hand-sorted copper confirmed by XRF	561	95
Mass of zinc present in the sample	1337.61	
Mass of iron present in the sample	8.88	
Additional mass of brass identified by XRF	754.49	51
Mass of lead present in the sample	102.55	
Additional mass of copper identified by XRF	136.64	86.8
Hard sort brass fraction confirmed by XRF	1778	53
Mass of other fractions present in the sample	300.26	
Mass of other fractions present in the hand-sorted brass	12.58	
Total mass	4992.01	

The largest amount of the metal present in the heavier fraction sample was copper and its alloys which was about 2532.49g of brass and 697.64g of copper. The second largest fraction present in the sample was zinc which was about 1337.61g. Whereas, iron, lead, and other fractions were not significantly present in the sample. The copper content present in the hand-sorted brass confirmed by XRF was 53%, in other than hand-sorted brass it was 51% whereas copper content given by XRF in the copper fraction was 95%.

For the second sample, size fraction +16mm -30mm, the following results were obtained:

Table 13 XRF separated fractions from the second sample +16mm -30mm fraction

Elements present	**g**	**XRF Cu (%)**
Mass of hand-sorted copper confirmed by XRF	197	96.6
Mass of zinc present in the sample	280.97	
Mass of iron present in the sample	183.23	
Additional mass of brass identified by XRF	170.9	49
Hard sort brass fraction confirmed by XRF	409.31	56
Mass of other fractions present in the sample	171.09	
Total mass	1412.5	

The largest amount of the metal present in the heavier fraction sample was copper and its alloys which was about 580.21g of brass and 197g of copper. The second largest fraction present in the sample was zinc which was about 280.97. Whereas iron, and other fractions were not significantly present in the sample. In this sample no particle of lead was present. The copper content given by XRF in the hand-sorted brass was 56%, in other than hand-sorted brass it was 49% whereas copper content in the copper fraction given by XRF was 96.6%.

5.2.3 Third sample -30mm +10mm

For the third sample, size fraction -16mm +10mm, the following results were obtained:

Table 14 XRF separated fractions from the third sample -16mm +10mm fraction.

Elements present	**g**	**XRF Cu (%)**
Mass of hand-sorted copper confirmed by XRF	447	94
Mass of zinc present in the sample	667.65	
Mass of iron present in the sample	9.01	
Additional mass of brass identified by XRF	500.74	52
Mass of lead present in the sample	14.9	
Additional mass of copper identified by XRF	26.42	94
Hard sort brass fraction confirmed by XRF	1006.17	58
Mass of other fractions present in the sample	115.13	
Total mass	2787.02	

The largest amount of the metal present in the heavier fraction sample was copper and its alloys which was about 1506.91g of brass and 473.42g of copper. The second largest fraction present in the sample was zinc which was about 667.65g. Whereas, iron, lead, and other fractions were not significantly present in the sample. The copper content given by XRF in the hand-sorted brass was 58%, in other than hand-sorted brass was 52% whereas the copper content given by XRF in the copper fraction was 94%.

For the third sample, size fraction +16mm -30mm, the following results were obtained:

Table 15 XRF separated fractions from the third sample +16mm -30mm fraction

Elements present	**g**	**XRF Cu (%)**
Mass of hand-sorted copper confirmed by XRF	142	92.6
Mass of zinc present in the sample	392.44	
Mass of iron present in the sample	8.71	
Additional mass of brass identified by XRF	25.91	50
Hard sort brass fraction confirmed by XRF	169.6	51.67
Total mass	738.66	

The larger fraction present in the sample was copper and its alloys which was about 195.51g of brass and 142g of copper. The second largest fraction present in the sample was zinc which was about 392.44g. Whereas, iron, lead, and other fractions were not present in the sample. The copper composition given by XRF in the hand-sorted brass copper content was 51.67%, in other than hand-sorted brass was 50% whereas copper content by XRF in the copper fraction was 92.6%.

5.2.4 Sample -90mm +30mm

For the sample, size fraction -90mm +30mm, the following results were obtained:

Table 16 XRF separated fractions from the sample +30mm -90mm fraction.

Elements present	**g**	**XRF Cu %**
Mass of hand-sorted copper confirmed by XRF	1714.23	91.35
Mass of zinc present in the sample	1031.83	
Mass of iron present in the sample	91.21	
Additional mass of brass identified by XRF	1067.63	50
Hard sort brass fraction confirmed by XRF	1886.73	56
Mass of iron composites present in the sample	799.00	
Mass of other fractions present in the sample	193.53	
Total mass	6784.16	

The larger fraction present in the sample was copper and its alloys which was about 2954.36g of brass and 1714.23g of copper. The second larger fraction present in the sample was zinc which was about 1031.83g. Whereas, iron, its composites, and other fractions were not significantly present in the sample. The copper content given by XRF in the hand-sorted brass was 56%, in other than hand-sorted brass was 50% whereas the copper content given by XRF in the copper fraction was 91.35%.

5.3 Calculation of metals grade in the samples of the fluidized bed separation

5.3.1 For the first sample of size fraction -30mm +10mm

In the first experiment for the first sample, fluidized separated lighter and heavier fractions were sampled and further separated on the basis of density, magnetic properties, visual properties, and chemical composition. Firstly, the sample was divided into two fractions based on the size, -16mm +10mm fraction and a +16mm -30mm fraction. From the total 7863g of the sample, 75.9w% of

the mass belongs to the -16mm +10mm and 24.1w% of the total mass belongs to the +16mm -30mm which showed a larger amount of the particles belong to the -16mm +10mm fraction. For each size fraction, materials were further separated based on magnetic properties with the handhold magnet of 0.7T intensity. In the lighter fraction for the size class -16mm +10mm, the fraction of magnetic particles was very low with 0.96w% and in the size fraction +16mm -30mm, there was no magnetic particle. The calculations showed that there were only 0.68w% of the magnetic particles were present in the feed of light fraction. In the heavier fraction for the size class -16mm +10mm, the magnetic particles fraction was 5.30w% and in the size fraction +16mm -30mm, there was a 10.04% magnetic particle fraction. The calculations showed that there were only 6.20w% of the magnetic particles were present in the size class -30mm +10mm of the heavier fraction whereas in the feed without size and density separation, 1.90w% particles were magnetic.

Density separation showed that all the copper and brass present in the feed were in the heavier fraction, there was no brass and copper present in the lighter fraction. In the heavier fraction, no brass and copper particles were present in the density class less than 3.0 g/cm3. After hand sorting and XRF analysis, the total percentage of copper present in copper fraction and brass fraction was used to back-calculate the amount of copper in feed. For the size fraction -16mm +10mm in the heavier fraction, there was 13.3% copper, 48.38% brass with 53.2% copper content and for the size fraction +16mm -30mm, there was 22.38% copper, 61.47% brass with 53.2% copper content was present in the non-magnetic fraction. In the total heavy fraction of size -30mm +10mm, copper was 15 % and brass was 50.9 % in the non-magnetic fraction. The calculation for the total feed without density separation showed that in the -16mm +10mm size fraction, there was 3.28% copper, 11.9% brass present as a non-magnetic fraction and for the size fraction +16mm -30mm, there was 3.49% of copper, 9.65% brass present. In the total feed of -30mm +10mm with magnetic separation but without size and density separation, copper was 3.34% in copper fraction, brass was 11.3% with 53.2% copper content. The lighter fraction calculations showed that about 68% aluminum and 8.33% magnesium were present and analyzed by density separation. In the heavier fraction, else than copper and brass, zinc, iron and lead were present along with the composite material referred to as others. The percentage of zinc, iron, lead and others in the non-magnetic fraction in the feed was 5.88%, 0.318%, 0.046% and 2.1% respectively. The fluidized bed was very efficient in upgrading copper content for both size classes -16mm +10mm and +16mm -30mm. Calculation showed that copper was upgraded from 3.28% in the feed to 13.3% in the heavier fraction in the -16mm +10mm size class and 3.49% to 22.3% in the +16mm -30mm size class. Brass upgrading showed the same behaviour as upgrading. About 11.9% was present in the feed of the -16mm +10mm size class upgraded to 48.39% and 9.65% was present in the +16mm -30mm size class which was upgraded to 61.47%. In the feed, total copper was 3.34% and 11.3% brass was present which upgraded to 15% and 50.9% respectively.

Table 17 mass balance of the first sample of the size class -30mm +10mm.

Product Sortfluid		Sample 1 Size class		Quality % Magnet 0,7T		2,5-3,0 g/cm³	1,4 - 2,5 g/cm³	Visual, hand sort and XRF >3.0 g/cm³ NON MAG					
"10/30 mm"		mm	m%	MAG	NON MAG	"Al"	"Mg"	Cu	Zn	Fe	brass	Pb	others
Product	m%										(53,2% Cu)		
		"10/16"	70.74	0.96	99.0	85.5	12.1	0	0	0	0	0	0.0
Lighter fraction	77.8	"16/30"	29.26	0.00	100.0	91.65	7.19	0	0	0	0	0	1.2
		LG	100.00	0.68	99.3	87.29	10.65	0	0	0	0	0	
		"10/16"	80.89	5.30	94.7	0.40	0.22	13.3	22.7	1.49	48.39	0.26	7.95
Heavier fraction	22.2	"16/30"	19.11	10.04	89.96	0.13	0.00	22.3	42.9	1.18	61.47	0.0	8.7
		SG	100	6.20	93.8	0.35	0.17	15.0	26.5	1.43	50.9	0.208	8.10
Feed	100.00	"10/16"	72.991	2.02	98.0	64.6	9.17	3.28	5.57	0.37	11.9	0.063	1.95
		"16/30"	27.009	1.57	98.4	77.3	6.06	3.49	6.73	0.19	9.65	0.000	2.34
NE Prod	"10/30 mm"	Total	100	1.90	98.1	68.0	8.33	3.34	5.88	0.318	11.3	0.046	2.1

5.3.2 For the second sample of size fraction -30mm +10mm

In the second experiment, separation was done like in the first experiment. In this experiment, only the heavy fraction was sampled whereas, for the lighter fraction, results from the first experiment were used. For the analysis, 6745g of the sample was taken from the heavier fraction. From the total 10593.7g of the sample, 75.4w% of the mass belongs to the -16mm +10mm and 24.6w% of the mass belongs to the +16mm -30mm which showed a larger amount of the particles belong to the -16mm +10mm fraction. In the new heavier fraction for the size class -16mm +10mm, the magnetic particles fraction was 4.69w% and in the size fraction +16mm -30mm, there were 4.0w% magnetic particles. The calculations showed that there was 4.54w% of the magnetic particles were present in the total heavier fraction whereas in the total feed magnetic particles were 1.53w%.

In the heavier fraction, no brass and copper particles were present in the density class less than 3.0 g/cm3. For the size fraction -16mm +10mm in the heavier fraction, there was 13.2w% of copper and 48.1w% of brass with 53.2 w% copper content and for the size fraction +16mm -30mm, there was 13.4w% of copper, 39.3w% and brass with 53.2w% copper content. In the feed of heavy fraction of size fraction -30mm +10mm without size separation, copper was 13.3w% and brass was 46.1w%. The calculation for the total feed without density separation showed that in the -16mm +10mm size fraction, there was 3.17w% copper and 11.5 w% brass and for the size fraction +16mm -30mm, there was 2.34w% of copper, and 6.91 w% was brass as a non-magnetic fraction. In the total feed without size and density fraction, copper was 2.94w% and brass was 10.23w%. In the heavier fraction, else than copper and brass, zinc, iron and lead were present along with the composite material referred to as others. Percentages of zinc, iron, and lead in the non-magnetic fraction of feed were 5.32w%, 0.632w%, and 0.337w% respectively. Similar behaviour was observed in upgrading copper content for both size classes -16mm +10mm and +16mm -30mm for the second sample as in the first sample. Calculation showed that copper was upgraded from 3.17w% in the feed to 13.2w% in the heavier fraction in the size class -16mm +10mm and 2.34w% to 13.4w% in the size class +16mm -30mm. Brass upgrading showed the same behaviour. About 11.5w% was present in the feed of size class -16mm +10mm upgraded to 48.1w% and 6.91w% was present in the size class which was upgraded to 39.3w%. In the feed, total copper was 2.94w% and 10.23w% was brass which upgraded to 13.3w% and 46.1w% respectively.

Table 18 mass balance of the second sample of the size class -30mm +10mm

Product		Sample 2		Quality %									
Sortfluid		Size class		Magnet 0,7T		,5-3,0 g/cm	1,4 - 2,5 g/cm^3	Visual, hand sort and XRF >3.0 g/cm^3 NON MAG					
"10/30 mm"		mm	m%	MAG	NON MAG	"Al"	"Mg"	Cu	Zn	Fe	brass	Pb	other
Product	m%										(53,2% Cu)		
		"10/16"	70.74	0.96	99.0	85.5	12.1	0	0	0	0	0	
Lighter fraction	77.8	"16/30"	29.26	0.00	100.0	91.7	7.19	0	0	0	0	0	
		LG	100.00	0.68	99.32	87.3	10.65	0	0	0	0	0	
		"10/16"	78.13	4.69	95.3	0.588	0.00	13.2	25.4	0.2	48.1	1.9	5.9
Heavier fraction	22.2	"16/30"	21.87	4.00	96.0	0.271	0.00	13.4	19.0	12.4	39.3	0.0	11.6
		SG	100	4.54	95.46	0.519	0.00	13.3	24.0	2.85	46.1	1.520	
Feed	100.00	"10/16"	72.38	1.85	98.2	65.2	9.19	3.17	6.08	0.04	11.5	0.466	
		"16/30"	27.62	0.70	99.3	75.6	5.93	2.34	3.34	2.18	6.91	0.000	
NE Prod	'10/30 mm'	GESAMT	100	1.53	98.5	68.0	8.29	2.94	5.32	0.632	10.23	0.337	

5.3.3 For the third sample of size fraction -30mm +10mm

In the third experiment, separation was done like the first experiment. In this experiment, only a heavy fraction was sampled whereas, for the lighter fraction, results from the first experiment were used. For the analysis, 3983g of the sample was taken from the heavier fraction. From the total 7831.7g of the sample, 73.66w% of the mass belongs to the -16mm +10mm and 26.34w% of the mass belongs to the +16mm -30mm. In the new heavier fraction for the size class, magnetic particles fraction was 8.11w% into -16mm +10mm size fraction and in +16mm -30mm size fraction, there were 21.04w% magnetic particles. The calculations showed that there were 11.15w% of the magnetic particles present in the heavier fraction feed of size -30mm +10mm without size separation. In the total feed without size and density separation, the magnetic fraction was 3.00w%.

In the heavier fraction, no brass and copper particles were present in the density class less than 3.0 g/cm3. For the size fraction -16mm +10mm in the heavier fraction, there was 15.5 w% of copper and 49.5w% brass with a copper content of 56.2w% and in the size fraction +16mm -30mm, there was 15.2w% of copper, and 20.9w% of brass present as a non-magnetic fraction. In the feed of heavy fraction without size separation, copper was 15.4w% and brass was 42.7w% in non-magnetic fraction. The calculation for the total feed without density separation showed that in the -16mm +10mm size fraction, there was 3.66w% copper and 11.7w% brass and in the size fraction +16mm -30mm, there was 2.82 w% of copper, 3.89w% brass as a non-magnetic fraction. In the total feed without size and density separation, copper was 3.43w%, and brass was 9.48w%. In the heavier fraction, else than copper and brass, zinc, iron and lead were present along with the composite material referred to as others. Percentages of zinc, iron, and lead in the non-magnetic fraction of feed were 5.90 w%, 0.009 w%, and 0.083 w% respectively. The calculation for the third sample showed that copper was upgraded from 3.66w% in the feed to 15.5w% in the heavier fraction of the size class -16mm +10mm and 2.82w% to 15.2w% for the size class +16mm -30mm. Brass upgrading showed the same behaviour. About 11.7w% was present in the feed of size class -16mm +10mm upgraded to 49.5w% and 3.89w% was present in the size class +16mm -30mm

which was upgraded to 20.9w%. In the feed, total copper was 3.43w% and 9.48w% was brass which upgraded to 15.4w% and 42.7w% respectively.

Table 19 mass balance of the third sample of the size class -30mm +10mm

Product		Sample 3		Quality %									
Sortfluid		Size class		Magnet 0,7T		2,5-3,0 g/cm^3	1,4 - 2,5 g/cm^3	Visual, hand sort and XRF >3.0 g/cm^3 NON MAG					
"10/30 mm"		mm	m%	MAG	NON MAG	"Al"	"Mg"	Cu	Zn	Fe	brass	Pb	Others
Product	m%										(56,2% Cu)		
		"10/16"	70.74	0.96	99.0	85.5	12.1	0	0	0	0	0	
Lighter fraction	77.8	"16/30"	29.26	0.00	100.0	91.7	7.19	0	0	0	0	0	
		LG	100.00	0.68	99.32	87.29	10.65	0	0	0	0	0	
		"10/16"	76.50	8.11	91.9	0.43	0.00	15.5	21.9	0.296	49.5	0.489	3.8
Heavier fraction	22.2	"16/30"	23.50	21.04	79.0	0.11	0.00	15.2	41.9	0.930	20.9	0.000	0.0
		SG	100	11.15	88.85	0.35	0.00	15.4	26.6	0.445	42.7	0.374	
Feed	100.00	"10/16"	72.02	2.64	97.4	65.4	9.24	3.66	5.16	0.070	11.7	0.115	
		"16/30"	27.98	3.92	96.08	74.6	5.85	2.82	7.80	0.173	3.89	0.000	
NE Prod	'10/30 mm	GESAMT	100	3.00	97.0	68.0	8.29	3.43	5.90	0.099	9.48	0.083	

5.3.4 Size fraction -90mm +30mm

For the size fraction -90mm +30mm, particles from lighter and heavier fractions of the sample were further separated based on density, magnetic properties, visual properties, and chemical composition. Firstly, the sample was separated based on magnetic properties. In the lighter fraction, the fraction of magnetic particles was very low about 1.31w% in the feed, and in the heavier fraction, the magnetic particles fraction was 6.12w% in the feed. Calculations showed that there was only 2.28w% of the magnetic particle was present in total feed. For the density base separation, the Archimedes principle was used.

In the lighter fraction, copper was present in the density class greater than 3 g/cm3 but it was very low 0.23w% in the non-magnetic fraction. In the heavier fraction, no brass and copper particles were present in the density class less than 3.0 g/cm3. In the heavier fraction, there was 23.5 w% copper and 40.4w% brass as a non-magnetic fraction. The calculation for the total feed without density separation showed that copper was 4.92w% and brass was 8.16w%. In the heavier fraction, else than copper and brass, zinc, iron and lead were present along with the composite material. The percentage of zinc, iron, and composite materials in the non-magnetic fraction of feed without density separation was 2.85 w%, 0.25w%, and 2.21w% respectively. The calculation for the sample of size fraction -90mm +30mm showed that copper was upgraded from 2.85w% in the feed to 23.5w% in the heavier fraction and 8.16w% was brass which upgraded to 40.4w% respectively.

Table 20 mass balance of the sample of the size class -90mm +30mm

Product	Sortfluid	m%	Quality %									
			Magnet		Sink float		visuell und Hand-RFA >3,0 g/cm³ NON MAG					
			MAG	Non MAG	2,5-3,0 g/cm³	1,4-2,5 g/cm³						
					"Al"	"Mg"	Zn	Cu	brass	Fe composite	Fe	others
			%	%					(52,2 %Cu)			
	Light fraction	79.8	1.31	98.7	74.4	22.3	0	0.23	0	0	0	1.74
"30/90 mm"	Heavier fraction	20.2	6.12	93.9	0.737	0.265	14.1	23.5	40.4	10.9	1.25	2.65
	Feed	100.0	2.28	97.7	59.6	17.9	2.85	4.92	8.16	2.21	0.25	1.92

5.4 Density class recovery to analysis fluidized bed performance

To quantify the performance of the fluidized bed performance, all samples taken from the fluidized bed stream was separated in different density class of 1.4 g/cm^3, 2.5 g/cm^3, 3.0 g/cm^3 and greater than 3.0 g/cm^3. In the lighter fraction, most of material should be in the density class less than 3.0 g/cm^3 as in the sample magnesium, aluminum has density less than 3.0 g/cm^3. Other metals iron, copper, zinc, and lead have density greater than 7.0 g/cm^3 that should be reported in the heavier fraction.

5.4.1 First samples of size fraction -30mm +10mm

To analyze the recovery of the material in density classes, the liquid density separation method was used. Analysis for the heavier fraction of size class -16mm +10mm showed that all material sank in the liquid had a density less than 1.4 g/cm^3, only 99.78% of material sunk in the liquid with density 2.5 g/cm^3, and 99.38% material sunk in the liquid with density 3.0 g/cm^3 which float in the density liquid of more than 3.0 g/cm^3. These particles will have a density of more than 3.0 g/cm3. For the +16mm -30mm size class, 100% of the material sunk in the liquids with a density of 1.4 g/cm^3 and 2.5 g/cm^3, whereas only 99.87% of material sunk in the liquid with a density of 3.0 g/cm^{3}which has density greater than 3.0 g/cm^3.

According to the graphs, in the heavier fraction most of the material has a density greater than 3.0 g/cm^3 whereas in the lighter fraction most of the material has a density less than 3.0 g/cm^3. As fluidized bed-separated material with a threshold density of 4.0 g/cm^3, the material in heavier fraction should have a density greater than 4.0 g/cm^3 and the lighter fraction should have a density less than 4.0 g/cm^3. According to that, the density partition curves of the lighter and heavier fractions could indicate the density separation efficiency of the fluidized bed separator. Results showed that the fluidized bed was quite efficient in density sorting.

Figure 19 Graphs represent the recovery of materials in different density classes in a heavier fraction for the first sample +10mm -30mm

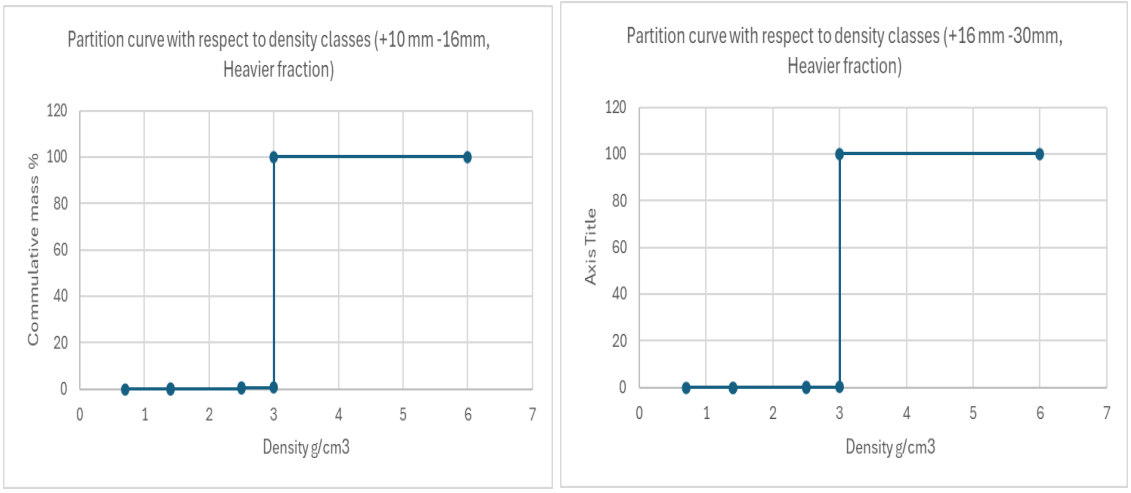

For the lighter fraction, the analysis showed that only 0.18% of the material had a density greater than 3.0 g/cm^3 for the size class -16mm +10mm and only 0.98% of the material for the size class +16mm -30mm had density greater than 3.0 g/cm^3. This showed that only 0.98% heavier material was reported in the lighter fractions for the size class +16mm -30mm and only 0.18% heavier material was reported in the lighter fraction for the size class -16mm +10mm. Analysis of lighter fractions showed that more than 99% of particles had a density between 1.4 g/cm3 to 3.0 g/cm3 for both size classes. It also showed that a fluidized bed was quite efficient for the density sorting of lighter materials.

Figure 20 Graphs represent the recovery of materials in different density classes in the lighter fraction for the first sample +10mm -30mm

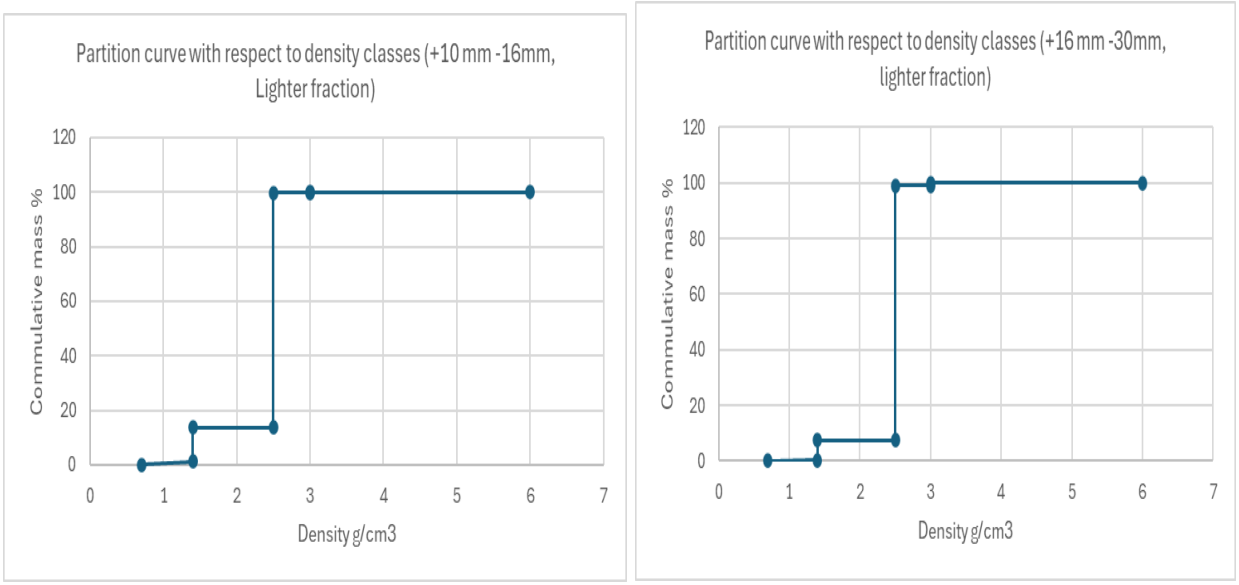

5.4.2 Second samples of size fraction -30mm +10mm

For the second sample, results of the lighter fraction were used from the first experiment whereas only the heavier fraction was sampled and analyzed again. In the heavier fraction of the second sample, the analysis showed that only 0.59 % material had a density of 3.0 g/cm^3 or less for the size class -16mm +10mm and only 0.37% material. Whereas the size class +16mm -30mm had a density of 3.0 g/cm^3 or less. This showed that 99.41% of particles were heavier than 3.0 g/cm^3 and only 0.59 % lighter material was reported in the heavier fraction for the size class -16mm +10mm and only 0.27 % lighter material was reported in the heavier fraction for the size class +16mm -30mm. Analysis of heavier fraction of the second also showed that fluidized bed was quite efficient for density sorting of lighter materials. It also indicated that most of the material in heavier fractions had a density greater than 3.0 g/cm^3.

Figure 21 Graphs represent the recovery of materials in different density classes in a heavier fraction of second sample, size +10 mm -30mm

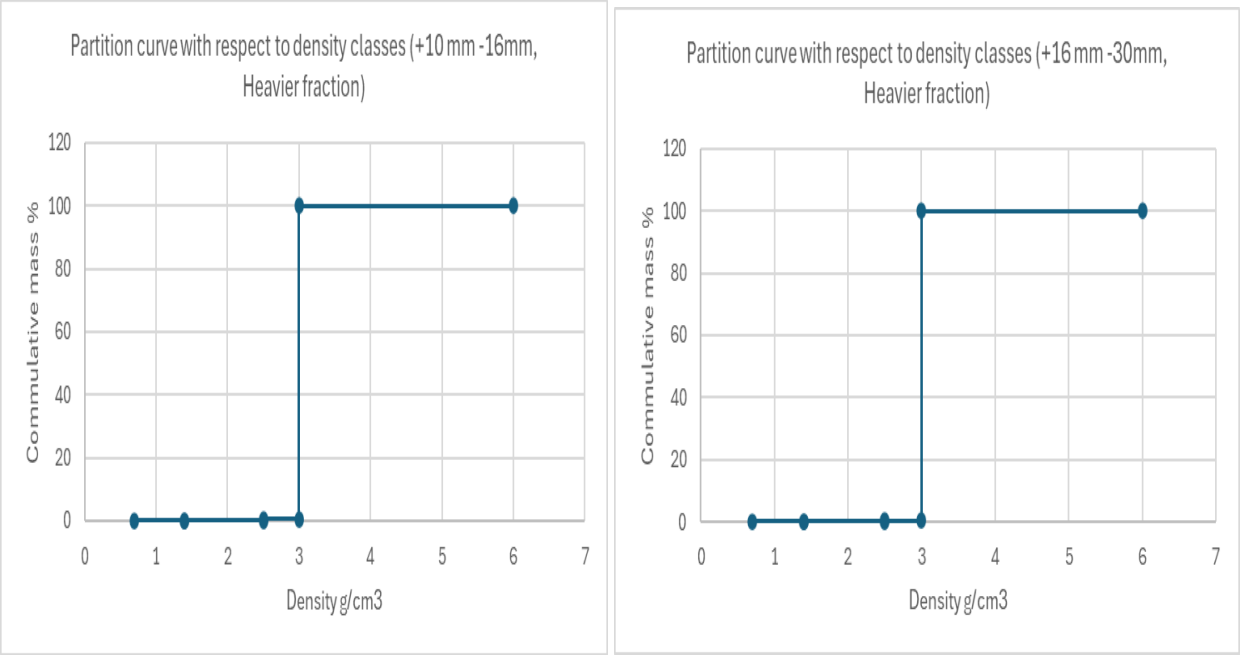

5.4.3 Third samples of size fraction -30mm +10mm

For the third sample, results from the first experiment were used for the lighter fraction whereas only a heavier fraction was sampled and analyzed again. In the heavier fraction of the third sample, the analysis showed that for the size class -16mm +10mm, only 0.43 % of the material had a density of 3.0 g/cm^3 or less. Whereas only 0.11 % of the material of the size class +16mm -30mm had a density of 3.0 g/cm^3 or less. This showed that 99.57 % of particles were heavier than 3.0 g/cm3 and only 0.43 % lighter particles were reported in the heavier fraction for the size class -16mm +10mm. Whereas for the size class, +16 mm -30 mm only 0.11 % lighter material was reported in the heavier fraction. Analysis of the heavier fraction of the third also showed that the

fluidized bed was quite efficient for the density sorting of lighter materials. It also indicated that most of the material in heavier fractions had a density greater than 3.0 g/cm^3.

Figure 22 Graphs represent the recovery of materials in different density classes in a heavier fraction of third sample, Size +10mm -30mm.

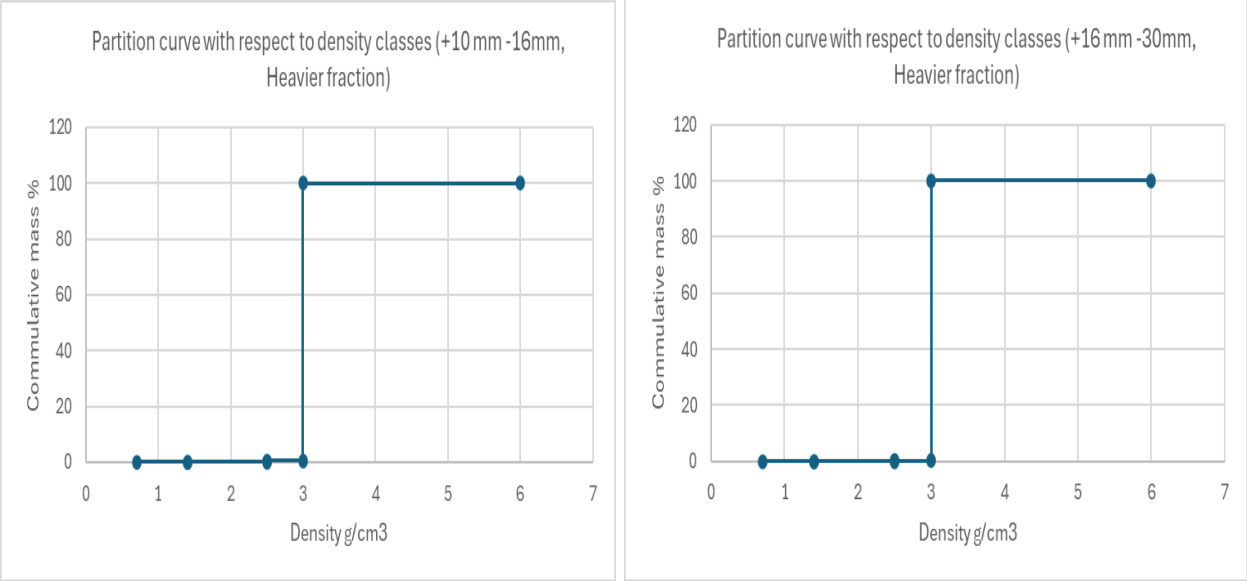

5.4.4 Sample of the size fraction -90mm +30mm

For the sample of size fraction -90mm +30mm, density was determined by Archimedes principle and material was divided into sample density fraction as for -30mm +10mm. Analysis of heavier fractions of -90mm +30mm showed that only 1% of the material has a density of 3.0 g/cm^3 or less whereas the remaining fraction had a density of more than g/cm^3 and in lighter fractions 2.21 % of the material of this size class had density greater than 3.0 g/cm^3. This showed that 99% of particles were heavier than g/cm^3, only 1 % lighter material was reported in the heavier fraction and 2.21% heavier material was reported in the lighter fraction. Analysis of -90mm +30mm size fraction showed that the fluidized bed was quite efficient for density sorting of heavier materials but showed some variation in the results for sorting of lighter fractions as compared to the lighter fractions in other samples of the size classes -30mm +10mm.

Figure 23 Graphs represent the recovery of materials in different density classes in -90mm +30mm sample.

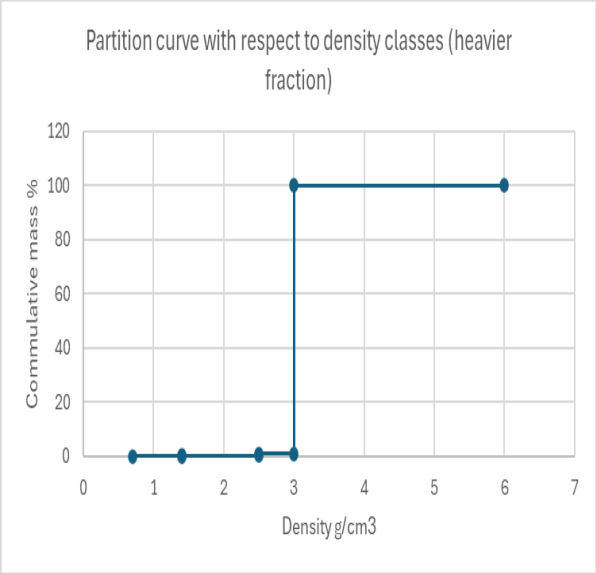

5.5 Sorting of eddy current magnetic reject sample

Eddy current magnetic reject sample was sorted into different materials present in the sample according to their physical nature. First separation was done with a magnet and then the magnetic fraction was hand-sorted in which polymers were separated as rubber fraction, glass and stones were separated as ceramics, metals other than copper as metallic material and other fractions as residual material. Then metallic material was further separated into iron, composite particles containing copper, composite particles containing aluminum and composite particles containing zinc.

Table 21 Percentage of different materials of -16mm +10mm eddy current magnetic reject sample

10/16mm fraction		
Material	mass (g)	Percentage of each fraction
Ceramics	2155	31.24
Rubber	462	6.70
Metallic materials	3626	52.57
Residual	385	5.58
Non magnetic fraction	111	1.61
Copper containing material	158.85	2.30
Sum	6897.85	100.00

Results showed that rubber and ceramics were the two largest non-metallic fractions in the sample whereas largest portion of sample contained metallic materials that was about 54.7% with 2.30% copper particles.

Table 22 Percentage of different materials of +16mm -30mm eddy current magnetic reject sample.

Material	mass (g)	Percentage of each fraction
Ceramics	644	24.21
Rubber	221	8.31
Cast metallic material	1425	53.57
Residual	183	6.88
Non magnetic fraction	35	1.32
Copper encooperated material	152.3	5.72
Sum	2660.3	100.00

The size fraction of +16mm -30mm of the sample showed the same fraction of different materials present in the sample. Metallic materials had the largest fraction in the sample which was about 59.2% with 5.72% copper particles.

5.6 Density separation of eddy current magnetic reject material

After hand sorting of the sample, hand-sorted metallic material was further separated according to their element composition using XRF. Metallic material was divided into an iron particle fraction, copper composite particle fraction, zinc composite particle fraction and aluminum composite particle fraction. In this sample, besides iron, almost every other metallic material existed in composite form, and they are composite with iron and polymers.

After further separation with XRF, further reduction of the sample was done by coning and quartering for the density analysis of the particles. Density was measured with Archimedes' principle with the use of a measuring scale having a precision of 0.01g to get the density relation for every fraction of metals and stones. A total 1925 g sample was analyzed with the 286 g stones and the rest of the mass belongs to the magnetic metallic fraction. After calculating density, a hindered settling ratio (HR) curve was made for the material to analyze the density behaviour of the particles.

Figure 24 Graph HR density curve of magnetic metallic material and stones in eddy current magnetic reject sample.

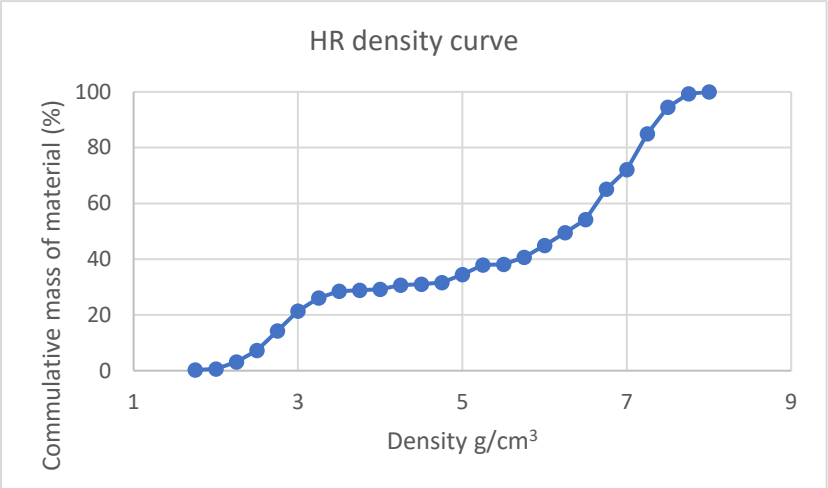

This curve shows that about 30% of the material that included stones aluminum composites and magnesium composites belonged to the density class less than 4.0 g/cm3 and 70% of the remaining material that included iron alloys, copper composites, and zinc composites had density more than 4.0 g/cm3.

Density analysis of every material fraction showed that about 99% of stones, 100% aluminum composite particles and the only particle of magnesium composite belong to the density class less than 4.0 g/cm3 whereas 99% iron particles, 94% copper composite particles and almost 94% zinc composite particles fall in the density class greater than 4.0 g/cm3.

Table 23 Classification of metallic material and stones of eddy current reject sample in density classes

Density cla	% of stones	% iron particles	% iron+copper particles	% iron+aluminium particles	% iron+zinc particles	% mg+iron particles
1.75		0.294557333			1.883393384	
2	0.9004274					100
2.25	9.6839745		3.006699277	4.747509154		
2.5	17.595123			12.27114025		
2.75	15.373835		1.552530838	61.98586392		
3	21.021652			6.98288342		
3.25	17.85439		1.592407486	14.01260325		
3.5	13.758671		0.273819651			
3.75	2.5506271	0.724212391				
4					5.707500819	
4.25					23.12479528	
4.5			1.799766057			
4.75		0.636731078	0.996916206			
5		0.963401805	12.80572097			
5.25		2.967720503	8.169396002		6.591876842	
5.5	1.2612991					
5.75		5.302032003	1.600382816			
6		4.608825646	5.080284985		14.03537504	
6.25		5.564475943	2.560080817		22.5761546	
6.5		5.374010298	6.002764781		16.95872912	
6.75		17.65350756	13.37728626			
7		8.498975693	13.5952786		9.12217491	
7.25		24.76939261	5.061675883			
7.5		16.19733127	2.610591238			
7.75		5.80809479	18.04019566			
8		0.636731078	1.874202467			
	100	100	100	100	100	100

6 Discussion

6.1 Magnetic separation

The magnetic separation of the sample was done using two magnets with different intensities. One magnet had an intensity of 0.1T and other was with 0.7T. Weak and strong magnets show huge differences in the separation of magnetic particles. Weak magnets almost did not attract any material present in the sample, but strong magnets separated magnetic particles and showed different results. Magnetic particles mentioned in all the above results were attracted by a strong magnet as that magnet could attract weak magnet particles as well. As magnetic separation was done with the handhold magnet, the orientation of particles also affected separation especially in the case of large particles. Some of the particles show non-magnetic behaviour from one side and magnetic behaviour on the other side. Some particles contain iron joints and welding that showed magnetism on the specific side. This behavior was not more common but particles of the size class +30mm -90mm showed this behavior.

Figure 25 images of the particles that showed magnetism on one side and non-magnetic behaviour on other side.

6.2 Density separation

Density separation was done with the liquid fluids in different density classes. Density separation showed very good results for the separation based on density as it was confirmed with the XRF analysis of the heavier fraction. XRF results showed that almost all particles present in the density fraction greater than 3.0 g/cm3 belong to the metal classes that have a density of more than 3.0 g/cm3. No aluminum or magnesium alloy was reported in the density class greater than 3.0 g/cm3. So, due to the density of the aluminum in the range of +2.5 g/cm3 to -3.0 g/cm3 and XRF analysis of the heavier fraction and some particles of lighter fraction, it could be concluded that particles in the density range of +2.5 g/cm3to -3.0 g/cm3 were belong to aluminum. A similar conclusion was drawn for the particles in the density class -2.5 g/cm3 to +1.4 g/cm3 and concluded that these particles were magnesium alloys.

Figure 26 left image shows particles with the density class -2.5 g/cm3 to +1.4 g/cm3 and the right image shows the particle with the density class +2.5 g/cm3 to -3.0 g/cm3

6.3 Hand sorting of copper and brass

Hand sorting of copper and brass was done to analyze the separation of the material based on physical appearance. As copper and brass have different appearance than the other fraction present iron, lead, zinc, aluminum, and magnesium. So, it was easier to separate these fractions from other materials. However, during hand sorting, it was observed that some particles had a coating which made it difficult to identify them by visual inspection. In the case of copper, more than 90% of the copper present in the sample was efficiently separated by hand sorting in all cases else than the second sample with the size fraction -16mm +10mm. It was the case because during hand sorting aim was to separate copper with high precision, to observe the effect of high precision separated copper on the total percentage of copper analysis by XRF in that fraction. Results of this fraction showed that the amount of the hand-sorted copper was reduced from 90% in other samples to 80% in this sample to get the precision, but the composition of the copper analyzed by XRF almost remained the same.

Figure 27 Left image shows particle of copper identified by XRF and right image shows particle of hand-sorted copper.

In the case of brass, hand sorting showed high variability in the results compared to the copper. In all the cases, efficiency of hand sorting was more than 95% which means more than 95% of hand-sorted particles were brass but the percentage of the sorted brass with the reference of total brass had large variability. This variability in the results was due to coating of brass with the other material, due to the unclean surface of the brass, the presence of a large number of copper alloys with different appearance, and the decrease in particle size which made sorting more difficult. With the course of work and assistance by the XRF system, hand sorting results improved. This may also explain, why the third sample of the size fraction 10/30mm, that was separated first, showed lower percentage of hand separated brass than the first sample of the size fraction, that was done at the end.

Figure 28 Left image shows particle of brass identified by XRF and right image shows particle of hand-sorted brass.

For the size fraction +30mm -90mmmm, effect of particle size was also observed as some particles were large and some were small. This particle size variation made the hand sorting difficult. As in the case of large particles, some particles had a portion with brass appearance eventually some coated portion or with an appearance of other elements. In that case, the elemental decision was based on the elemental composition of the largest portion of the particle confirmed by XRF.

6.4 XRF analysis

After hand sorting, XRF analysis was done for hand-sorted copper, hand-sorted brass, and the heavier fraction of all samples. XRF analysis was done to separate samples into different metals according to their composition. The sample was separated as copper, copper alloys like brass, zinc alloys, iron alloys, lead, and other fractions containing composite materials, tin, and silver.

Particles with more than 80% of copper were considered copper fraction, particles with the copper range of 35-80% were considered copper fraction, and particles with a copper range of 35-80% were considered copper alloy. In the case of less than 35% of the copper, particles were classified on the basis of an element with the higher fraction.

Results from the XRF depend on the instrumentation of the XRF as discussed in the literature. Different XRFs have different penetration depths to identify the present element depending on the

X-rays source. The element identification and results' accuracy also depend on the instrument's detector. For the lighter element, the accuracy of the XRF is mostly very low.
During the analysis, some particles that had a coating on one side showed a different composition on the other side of the particles. Similarly, particles that had some uncoated sections due to wear of coating also showed high variability in the results if the reading were taken with the slide change in the position of the particle.

Figure 29 Images of the same particle with the coated and uncoated side showing huge variability in XRF results.

For some particles results showed variability with the change in the cross-section of the particle which indicates that the size and position of the particle also affect the results. Some big particles also showed variability in the results that could be high at different sections of the particles. The bigger particles that showed high variability in the results were classified based on the range of elements present and based on the maximum number of readings with nearest range. For some coating particles, one side had a high percentage of an element while on the uncoated it was not the case, sometimes it contained minor percentage of that element.

Figure 30 Particles with different shape, size and that showed variability with change in cross-section.

Some particles showed that they contained silver, but the percentage of the silver was very low that results silver was not in the detection level. Particle shape also affected the results as some

parts of the particles were not exposed due to deformation. However optical observation indicated the presence of a certain element in the particle. Some particles had silver parts as could be observed from the material, but XRF results did not show silver, when the position of the particle changed or the specific part was exposed to the XRF scanning surface, results showed the presence of silver in the particle.

Particle shape, size, coating of other materials on the particle, and surface cleanliness affects the results and showed variability in the single particle. (Crocombe, 2013)

Presence of large number of alloys of different metals and the large variability in the results due to shape and coating factors, classification of the sample based on the specific composition was very difficult. So, materials that were the alloys of the same metal were classified in that class. Material classified as brass had copper composition varying between 35 and80w%. Particles in the sample that were composite of two different metals were considered as "other fraction". Samples with large particles showed large variability in the results like the iron fraction in the second sample.

Figure 31 Image of the composite particles consider as other fraction in XRF analysis.

XRF is suitable for the qualitative analysis of the metal and its alloys but for quantitative analysis of metal and its alloys, XRF results depend on a lot of factors like surface condition, particle shape, particle size, liberation of the particle, elements present in the alloy system and XRF instrumentation.(Crocombe, 2013)

6.5 Comparison between hand sorting and XRF sorting

XRF and hand sorting of the samples were done to separate copper and its alloys. During hand sorting, copper and brass was separated from all samples. Then these separated fractions along with the remaining material in the density class greater than 3.0 g/cm^3 of heavier analyzed by XRF. XRF gave information about the composition of the material which was used to get the efficiency of the hand sorting. Additional copper and brass present in the sample was also determined by XRF.

Hand sorting depends on the skills of the sorting worker to analyze the material, it is labor intensive, needs low initial capital cost. However, results showed that it's not possible to 100% separate a material from the sample with hand sorting which means it's less accurate for sorting. Results also showed that hand sorting was an inconsistent method due to the coating of the materials with other materials, surface condition, and similar aesthetics of some metals. On the other hand, XRF is also considered as surface technique but in most of the case due to thin coatings, X-rays could penetrate material and gave an indication of the material. It could miss some coated or painted materials which can reduce its accuracy and efficiency. It needed high capital investment, but it is faster, especially in the case of automated sorting. Results showed that XRF helped classifying the material more efficiently compared to hand sorting, especially in the case of coated material and metals with the same aesthetic. Sometimes, metal surface conditions got too rough to be identified by hand sorting, but experiments showed that XRF gave an indication in that case about the metal. For the higher accuracy, high consistency in results, and for good classification of the same aesthetic metals XRF sorting was identified as more reliable sorting method than hand sorting.

In the graph, the XRF percentage showed the additional amount of brass separated with XRF along with hand sorting, XRF was also able to identify hand-sorted material.

Table 24 Graph shows the comparison between hand sorting and XRF sorting

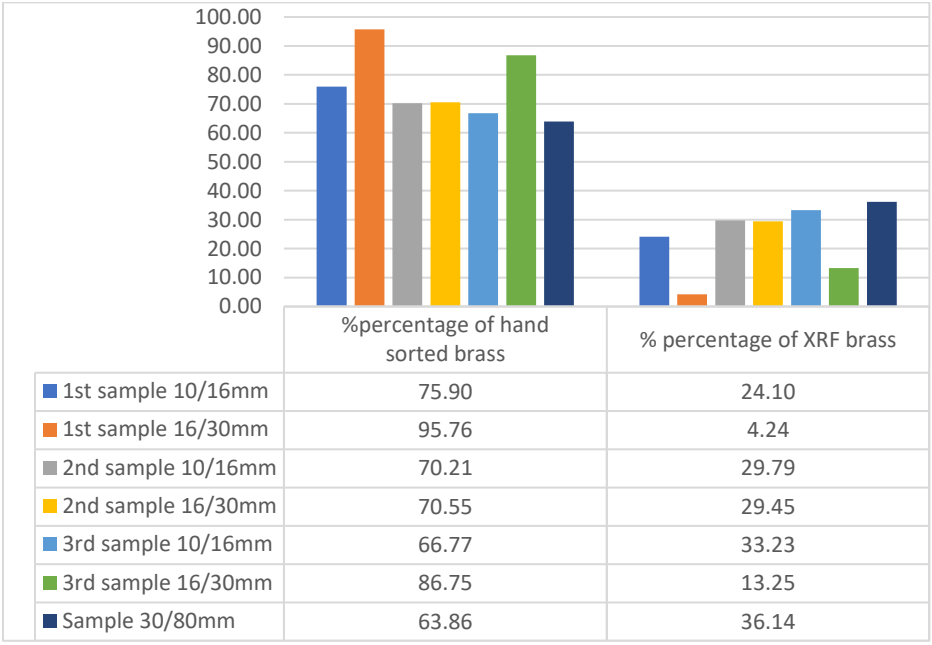

	%percentage of hand sorted brass	% percentage of XRF brass
1st sample 10/16mm	75.90	24.10
1st sample 16/30mm	95.76	4.24
2nd sample 10/16mm	70.21	29.79
2nd sample 16/30mm	70.55	29.45
3rd sample 10/16mm	66.77	33.23
3rd sample 16/30mm	86.75	13.25
Sample 30/80mm	63.86	36.14

6.6 Position of fluidized bed separator in processing plant

In a processing plant, the fluidized bed separator can be positioned before the eddy current separator to separate the lighter fraction which contains aluminum, magnesium, and polymers as per the analysis of the sample from the heavier fraction which contained copper, zinc, lead, iron, and rest of fraction. In this case, the lighter fraction will be processed with an eddy current

separator to get aluminum and magnesium from the lighter fraction. Whereas heavier fractions will be processed separately to sort required material like copper and its alloys from the rest of the heavier fractions. For this position, rubber could affect the efficiency of the fluidized bed separation due to abrasion of rubber and accumulation of fluidized media particles on the rubber surface. Due to its soft surface compared to the remaining material, it can change its apparent density and result in a loss of fluidized media. (Chikerema & Moys, 2012) For spherical shapes or nearly sphere-shaped particles, larger dead zones along the particles is reported by Prusti et al., 2015 that can change the effective density of a particle due to the fluidized medium deposition and fines accumulation in the dead zone. Due to this reason, particles attain a heavier apparent weight and are positioned more deeply in the bed than expected. Shredding behavior showed that metal alloys mostly had pointy corners or brittle breakage and had less sphericity than the rubber particles which means rubber could affect the efficiency of the fluidized bed.

Based on the observation of the material's shape after shredding, the best position of the fluidized bed will be after the eddy current separator. After the eddy current separator, the feed of the fluidized bed will mostly contain metals and it will not affect its performance. As in the case of metals, there will not be too much deviation in the shape of the feed which could be the case for the position of the fluidized bed before eddying current. For this position, the material will be separated into conductive material (metals) and non-conductive material (rubber) by the eddy current separator, then the metallic fraction will be introduced in a fluidized bed which separates aluminum and magnesium as the lighter fraction from the feed, and rest as the heavier fraction.

6.7 Density separation of eddy current magnetic reject feed.

Density separation of the sample showed that most of the metallic material in the feed fell in the density class of greater than 4.5 g/cm^3 else than aluminum composite material and magnesium composite material whereas almost all stones that were the biggest non-metallic fraction had density less than 4.5 g/cm^3. This density separation showed that metallic content in the sample can be upgraded with the density treatment using a fluidized bed separator. This metallic upgradation will increase the content of iron particles, copper composite particle and zinc composite in the feed and further separation of metals into their individual group will be easier and more efficient.

7 Conclusion

This research demonstrates the performance of a fluidized bed separator in separating the eddy current processed metals according to their densities. The fluidized bed separates the metals on the basis of their densities into heavier and lighter fractions based on the threshold density set for the separator. Efficiency of the fluidized bed was analyzed by liquid density fluids by further separating both fractions into different density classes. The fluidized bed was very efficient in separating materials based on their densities as the amount of the heavier material in the lighter fraction was very low and a similar trend was observed for the heavier fraction as well. Calculation of different metal fractions in the fluidized bed separator feed after classifying materials into their respective class showed that a fluidized bed can upgrade the metal content of a specific element like aluminum into specific fractions like in lighter fractions and copper in heavier fractions for the household and automobile scrap. A heavier fraction of the sample was used to analyze the hand sorting by sorting copper and brass to analyze the results of hand sorting in separating the target metals. XRF analysis was done on the remaining heavier fraction and the hand-sorted brass and copper to analyze the number of other elements present in the heavier fraction and made a comparison between hand sorting and XRF sorting. Results showed that XRF was very efficient in separating the materials, especially those which had the same appearance or had coated and painted surfaces. With the decrease in size, hand sorting became more labor-intensive, and difficult whereas an automatic XRF sorter could efficiently sort the material faster. Sample from the eddy current magnetic reject stream was analyzed with the efficiency of hand sorting, XRF sorting, and density sorting to calculate and upgrade the metal content of different metals in the sample. Density analysis showed that most of the metals else than aluminum composite particles fall in the density class greater than 4.0g/cm^3 which can be upgraded using a fluidized bed and then can be separated into different metal classes according to their nature using XRF.

8 References

Anantharaman, A., Cocco, R. A., & Chew, J. W. (2018). Evaluation of correlations for minimum fluidization velocity (Umf) in gas-solid fluidization. *Powder Technology*, *323*, 454–485. https://doi.org/10.1016/J.POWTEC.2017.10.016

Bowyer, D. J., Bratkovich, S., & Fernholz, K. (2015). *UNDERSTANDING STEEL RECOVERY AND RECYCLING RATES AND LIMITATIONS TO RECYCLING*. www.dovetailinc.org

Burkhard Beckhoff, habil. B. K. N. L. R. W. H. W. (2006). *Handbook of Practical X-Ray Fluorescence Analysis* (1st ed.). Springer Berlin, Heidelberg.

Capuzzi, S., & Timelli, G. (2018a). Preparation and Melting of Scrap in Aluminum Recycling: A Review. *Metals 2018, Vol. 8, Page 249*, *8*(4), 249. https://doi.org/10.3390/MET8040249

Capuzzi, S., & Timelli, G. (2018b). Preparation and Melting of Scrap in Aluminum Recycling: A Review. *Metals 2018, Vol. 8, Page 249*, *8*(4), 249. https://doi.org/10.3390/MET8040249

Chikerema, P., & Moys, M. (2012). Effects of Particle Size, Shape, and Density on the Performance of an Air Fluidized Bed in Dry Coal Beneficiation. *International Journal of Coal Preparation and Utilization*, *32*(2), 80–94. https://doi.org/10.1080/19392699.2011.640297

Copper Scrap Market: Global Industry Analysis and Forecast. (n.d.). Retrieved February 10, 2024, from https://www.maximizemarketresearch.com/market-report/copper-scrap-market/199960/

Corbeil, M.-C. (2009). Philip J. Potts and Margaret West (Eds.): Portable X-ray fluorescence spectrometry. Capabilities for in situ analysis. *Analytical and Bioanalytical Chemistry*, *393*(5), 1385–1386. https://doi.org/10.1007/s00216-008-2587-6

Crocombe, R. A. (2013). Handheld spectrometers: the state of the art. In M. A. Druy & R. A. Crocombe (Eds.), *Next-Generation Spectroscopic Technologies VI* (Vol. 8726, p. 87260R). SPIE. https://doi.org/10.1117/12.2017892

D. J.R. Davis. (2001). ASM Specialty Handbook, Copper and Copper Alloys. *ASM Handbook*, 133. https://www.asminternational.org/books-and-handbooks/results/-/journal_content/56/10192/16857723/PUBLICATION/

Donais, M. K., & George, D. B. (n.d.). *X-ray fluorescence spectrometry and its applications to archaeology : an illustrated guide*.

Grace, J. R., Bi, X., & Ellis, N. (2020). Essentials of fluidization technology. *Essentials of Fluidization Technology*, 1–604. https://doi.org/10.1002/9783527699483

Jujun, R., & Xu, Z. (2012). Approaches To Improve Separation Efficiency of Eddy Current Separation for Recovering Aluminum from Waste Toner Cartridges. *Environmental Science & Technology*, *46*, 6214–6221. https://doi.org/10.1021/es3008358

Kaas, A., Mütze, T., & Peuker, U. A. (2022). Review on Zigzag Air Classifier. *Processes 2022, Vol. 10, Page 764*, *10*(4), 764. https://doi.org/10.3390/PR10040764

Khan, W. S., Asmatulu, E., Uddin, M. N., & Asmatulu, R. (2022). Recycling and Reusing of Engineering Materials: Recycling for Sustainable Developments. *Recycling and Reusing of*

Engineering Materials: Recycling for Sustainable Developments, 1–351. https://doi.org/10.1016/C2019-0-04547-5

Khawaja, H., & Moatamedi, M. (2020). *Multiphysics modeling of fluid-particulate systems*. https://doi.org/10.1016/C2018-0-02737-1

Leopold, K. (2021). Michael Haschke, Jörg Flock, and Michael Haller: X-ray fluorescence spectroscopy for laboratory applications. *Analytical and Bioanalytical Chemistry*, *413*(26), 6455–6456. https://doi.org/10.1007/S00216-021-03592-1/METRICS

Loibl, A., & Tercero Espinoza, L. A. (2021). Current challenges in copper recycling: aligning insights from material flow analysis with technological research developments and industry issues in Europe and North America. *Resources, Conservation and Recycling*, *169*. https://doi.org/10.1016/J.RESCONREC.2021.105462

Meskers, C., Worrell, E., & Reuter, M. (2023a). *HANDBOOK OF RECYCLING State-of-the-art for Practitioners, Analysts, and Scientists SECOND EDITION*.

Meskers, C., Worrell, E., & Reuter, M. (2023b). *HANDBOOK OF RECYCLING State-of-the-art for Practitioners, Analysts, and Scientists SECOND EDITION*.

Meskers, C., Worrell, E., & Reuter, M. (2023c). *HANDBOOK OF RECYCLING State-of-the-art for Practitioners, Analysts, and Scientists SECOND EDITION*.

Metal Recycling Factsheet. (n.d.). Retrieved February 6, 2024, from https://circulareconomy.europa.eu/platform/sites/default/files/euric_metal_recycling_factsheet.pdf

Metals for Clean Energy: Pathways to solving Europe's raw materials challenge. (n.d.). Retrieved February 6, 2024, from https://eurometaux.eu/media/20ad5yza/2022-policymaker-summary-report-final.pdf

Michel, J. (2013). *Introduction to Copper and Copper Alloys*.

Mohanta, S., Rao, C. S., Daram, A. B., Chakraborty, S., & Meikap, B. C. (2013). Air Dense Medium Fluidized Bed for Dry Beneficiation of Coal: Technological Challenges for Future. *Particulate Science and Technology*, *31*(1), 16–27. https://doi.org/10.1080/02726351.2011.629285

Moraga, G., Huysveld, S., Mathieux, F., Blengini, G. A., Alaerts, L., Van Acker, K., de Meester, S., & Dewulf, J. (2019). Circular economy indicators: What do they measure? *Resources, Conservation and Recycling*, *146*, 452–461. https://doi.org/10.1016/J.RESCONREC.2019.03.045

Muchová, Lenka., Eder, Peter., Villanueva, Alejandro., & European Commission. Joint Research Centre. (n.d.). *End-of-waste criteria for copper and copper alloy scrap : technical proposals.*

Raabe, D., Ponge, D., Uggowitzer, P. J., Roscher, M., Paolantonio, M., Liu, C., Antrekowitsch, H., Kozeschnik, E., Seidmann, D., Gault, B., De Geuser, F., Deschamps, A., Hutchinson, C., Liu, C., Li, Z., Prangnell, P., Robson, J., Shanthraj, P., Vakili, S., … Pogatscher, S. (2022). Making sustainable aluminum by recycling scrap: The science of "dirty" alloys. *Progress in Materials Science*, *128*, 100947. https://doi.org/10.1016/J.PMATSCI.2022.100947

Reck, B. K., & Graedel, T. E. (2012). Challenges in metal recycling. *Science*, *337*(6095), 690–695. https://doi.org/10.1126/SCIENCE.1217501/SUPPL_FILE/690.MP3

S. He Y., W. H. D. C. & S. (2005). Airflow fields simulation on passive pulsing air classifiers . *Journal of the Southern African Institute of Mining and Metallurgy*, *105*(7), 525–531. https://doi.org/10.10520/AJA0038223X_3002

Sander, S., & Schubert, G. (2003). Size reduction of metals by means of swing-hammer shredders. *Chemical Engineering and Technology*, *26*(4), 409–415. https://doi.org/10.1002/CEAT.200390061

Sander, S., Schubert, G., & Timmel, G. (2002a). Characterisation of fragments produced by the comminution of metals especially considering the fragment shape. *Powder Technology*, *122*, 177–187. www.elsevier.comrlocaterpowtec

Sander, S., Schubert, G., & Timmel, G. (2002b). Characterisation of fragments produced by the comminution of metals especially considering the fragment shape. *Powder Technology*, *122*, 177–187. www.elsevier.comrlocaterpowtec

Scala, F., Horio, M., Wang, D., Fan, L.-S., Dennis, J. S., Grace, J. R., Lim, C. J., Di Natale, F., Nigro, R., Scala, F., Scala, F., Chirone, R., Salatino, P., Scala, F., Solimene, R., Montagnaro, F., Miccio, M., Miccio, F., Gulyurtlu, I., … Schratzer, B. (2013). Fluidized Bed Technologies for Near-Zero Emission Combustion and Gasification. In F. Scala (Ed.), *Fluidized Bed Technologies for Near-Zero Emission Combustion and Gasification* (pp. xv–xix). Woodhead Publishing. https://doi.org/https://doi.org/10.1016/B978-0-85709-541-1.50026-1

Schlesinger, M. (2013). Aluminum recycling: Second edition. In *Aluminum Recycling: Second Edition*. https://doi.org/10.1201/b16192

Schlesinger, M. E., King, M. J., Sole, K. C., & Davenport, W. G. (2011). Extractive Metallurgy of Copper. *Extractive Metallurgy of Copper*, 1–455. https://doi.org/10.1016/C2010-0-64841-3

Soulier, M., Glöser-Chahoud, S., Goldmann, D., & Tercero Espinoza, L. A. (2017). *Dynamic analysis of European copper flows*. https://doi.org/10.1016/j.resconrec.2017.10.013

The Future of Copper Will the looming supply gap short-circuit the energy transition? (2022). www.spglobal.com

The Importance of Recycling. (n.d.). Retrieved February 5, 2024, from https://copperalliance.org/wp-content/uploads/2022/02/ICA-RecyclingBrief-202201-A4-R2.pdf

XRF Analyzers | X-Ray Fluorescence Analyzers | Thermo Fisher Scientific - AT. (n.d.). Retrieved March 19, 2024, from https://www.thermofisher.com/at/en/home/industrial/spectroscopy-elemental-isotope-analysis/oes-xrd-xrf-analysis/x-ray-fluorescence/instruments.html

Yazici, E. Y., Deveci, H., Yazici, R., Greenway, R., & Akcil, A. (2011). Recovery of copper from scrap TV boards by eddy current separation. *Proceedings of the 15th Conference on Environment and Mineral Processing, Part I. VSB Tech. University of Ostrava, Czech Republic*, 27–33.

Zhou, X., Zhili, H. U., Yijun, T., Xunpeng, Q., & Lin, H. (n.d.). *CHINESE JOURNAL OF MECHANICAL ENGINEERING Failure Mechanisms and Structural Optimization of Shredder Hammer for Metal Scraps*. https://doi.org/10.3901/CJME.2016.0415.053

Appendix

Mass distribution -16mm +10mm (first sample)

Table 25 Mass distribution -16mm +10mm (first sample)

Probe		Sink/Float		Susceptibility		Fractions		hand sort	XRF (non-hand sorted)		XRF
Size class	Product	Density class	Mass	Mass (g)							
[mm]		[g/cm^3]	[g]	MP	UMP	Copper	Cu fraction (XRF)	brass	brass	Other	Cu in brass
10/16mm	Light fraction	> 3,0	5	0	5	0	0.00	0.00	0.00	0.00	0.00
		2.5	2343	16	2327	0	0.00	0.00	0.00	0.00	0.00
		1.4	339	10	329	0	0.00	0.00	0.00	0.00	0.00
		< 1,4	35	0	35	0	0.00	0.00	0.00	0.00	0.00
		Sum	2722	26	2696	0	0.00	0.00	0.00	0.00	0.00
	Heavy fraction	> 3,0	3227.83	172	3055.83	433.37	392.63322	1192.85	378.83	1060.15	825.4138
		2.5	13	0	13	0.77	0.00	0.00	0.00	0.00	0
		1.4	7	0	7	0	0.00	0.00	0.00	0.00	0
		< 1,4	0	0	0	0	0.00	0.00	0.00	0.00	0
		Sum	3247.83	172	3075.83	434.14	392.63322	1192.85	378.83	1060.15	825.4138

Mass distribution 16/30m (first sample)

Table 26 Mass distribution 16/30m (first sample)

Probe		Sink/Float		Susceptibility		Fractions		hand sort	XRF (non-hand sorted)		
Size class	Product	Density class	Mass	Mass (g)							
[mm]		[g/cm^3]	[g]	MP	UMP	Copper	Cu fraction (XRF)	brass	brass	Other	Cu in brass
16/30mm	Light fraction	> 3,0	11	0	11	0	0.00	0.00	0.00	0.00	0.00
		2.5	1032	0	1032	0	0.00	0.00	0.00	0.00	0.00
		1.4	81	0	81	0	0.00	0.00	0.00	0.00	0.00
		< 1,4	2	0	2	0	0.00	0.00	0.00	0.00	0.00
		Sum	1126	0	1126	0	0.00	0.00	0.00	0.00	0.00
	Heavy fraction	> 3,0	766.3	77	689.3	98	88.2	259.2	11.48	232.42	136.8692
		2.5	1	0	1	0	0	0	0	0	0
		1.4	0	0	0	0	0	0	0	0	0
		< 1,4	0	0	0	0	0	0	0	0	0
		Sum	767.3	77	690.3	98	88.2	259.2	11.48	232.42	136.8692

Copper content in lighter fraction (first sample)

Table 27 Copper content in lighter fraction (first sample)

Sort - Fluid	Size class		Sink/float	Susceptibility	Fractions				Content percentage								Density class Output%		
Mass percentage	Size class	Mass percentage	Density class	Masse [%]	masses [%]				IO,j				IO,0						
$r_{m,Sort-Fluid}$	[mm]	$r_{m,j}$	[g/cm³]	$m_{i,j}$	$g_{i,WP}$	$g_{i,UWP}$	$g_{i,Cu}$	$g_{i,brass}$	$g_{i,Cu+brass\_real}$	$r_{i,Cu}$	$r_{i,brass}$	$r_{i,Cu+brass\_real}$	$r_{i,Cu}$ *	$r_{i,brass}$ *	$r_{i,Cu+brass\_real}$ *	$r_{i,Cu}$ **	$r_{i,brass}$ **	$r_{i,Cu+brass\_real}$ **
Light fraction	10/16mm	70.74	> 3,0 (heavy metals)	0.18	0.00	100.00	0.00	0.00	0.00	0.00	0.00	0.00	0.00	0.00	0.00	0.00	0.00	0.00	0.00
			2,5 (Al)	86.08	0.68	99.32	0.00	0.00	0.00	0.00	0.00	0.00	0.00	0.00	0.00	0.00	0.00	0.00	0.00
			1,4 (Mg)	12.45	2.95	97.05	0.00	0.00	0.00	0.00	0.00	0.00	0.00	0.00	0.00	0.00	0.00	0.00	0.00
			< 1,4	1.29	0.00	100.00	0.00	0.00	0.00	0.00	0.00	0.00	0.00	0.00	0.00	0.00	0.00	0.00	0.00
			Summe	100.00	0.96	99.04	**0.00**	**0.00**	**0.00**	0.00	0.00	0.00	0.00	0.00	0.00				
	16/30mm	29.26	> 3,0	0.98	0.00	100.00	0.00	0.00	0.00	0.00	0.00	0.00	0.00	0.00	0.00	0.00	0.00	0.00	0.00
			2.5	91.65	0.00	100.00	0.00	0.00	0.00	0.00	0.00	0.00	0.00	0.00	0.00	0.00	0.00	0.00	0.00
			1.4	7.19	0.00	100.00	0.00	0.00	0.00	0.00	0.00	0.00	0.00	0.00	0.00	0.00	0.00	0.00	0.00
			< 1,4	0.18	0.00	100.00	0.00	0.00	0.00	0.00	0.00	0.00	0.00	0.00	0.00	0.00	0.00	0.00	0.00
			Summe	100.00	0.00	100.00	**0.00**	**0.00**	**0.00**	0.00	0.00	0.00	0.00	0.00	0.00				
77.82	Feed	100.00	> 3,0	0.42	0.00	100.00	0.00	0.00	0.00	0.00	0.00	0.00	0.00	0.00	0.00	0.00	0.00	0.00	0.00
			2.5	87.71	0.47	99.53	0.00	0.00	0.00	0.00	0.00	0.00	0.00	0.00	0.00	0.00	0.00	0.00	0.00
			1.4	10.91	2.38	97.62	0.00	0.00	0.00	0.00	0.00	0.00	0.00	0.00	0.00	0.00	0.00	0.00	0.00
			< 1,4	0.96	0.00	100.00	0.00	0.00	0.00	0.00	0.00	0.00	0.00	0.00	0.00	0.00	0.00	0.00	0.00
			Summe	100.00	0.68	99.32	**0.00**	**0.00**	**0.00**	0.00	0.00	0.00	0.00	0.00	0.00				

Copper content in heavier fractions (first sample)

Table 28 Copper content in heavier fractions (first sample)

Sort - Fluid		Size class		Sink/float	Susceptibility	Fractions			Content percentage						Density class Output%		
Mass percentage		Size class	Mass percentage	Density class	Masse [%]	masses [%]			I0,j			I0,0					
$r_{m,Sort-Fluid}$		[mm]	$r_{m,j}$	[g/cm³]	$m_{i,j}$	$g_{i,WP}$	$g_{i,LWP}$	$g_{i,Cu}$	$g_{i,brass}$	$g_{i,Cu+brass\ real}$	$r_{j,Cu}$	$r_{j,brass}$	$r_{j,Cu+brass\ real}$	$r_{i,Cu}$ *	$r_{i,brass}$ *	$r_{i,Cu+brass\ real}$	$r_{i,Cu}$ **	$r_{i,brass}$ **	$r_{i,Cu+brass\ real}$ **
Heavy fraction		10/16mm	80.89	>3,0	99.38	5.33	94.67	12.85	27.01	39.86	100.00	100.00	100.00	80.88	86.43	84.56	80.88	86.43	84.56
				2,5	0.40	0.00	100.00	0.00	0.00	0.00	0.00	0.00	0.00	0.00	0.00	0.00	0.00	0.00	0.00
				1,4	0.22	0.00	100.00	0.00	0.00	0.00	0.00	0.00	0.00	0.00	0.00	0.00	0.00	0.00	0.00
				<1,4	0.00	0.00	0.00	0.00	0.00	0.00	0.00	0.00	0.00	0.00	0.00	0.00	0.00	0.00	0.00
				Sum	100.00	5.30	94.70	**12.77**	**26.84**	**39.61**	100.00	100.00	100.00	80.88	86.43	84.56			
		16/30mm	**19.11**	>3,0	99.87	10.05	89.95	12.80	17.86	30.66	100.00	100.00	100.00	19.12	13.57	15.44	19.12	13.57	15.44
				2,5	0.13	0.00	100.00	0.00	0.00	0.00	0.00	0.00	0.00	0.00	0.00	0.00	#DIV/0!	0.00	0.000
				1,4	0.00	0.00	0.00	0.00	0.00	0.00	0.00	0.00	0.00	0.00	0.00	0.00	0.00	0.00	0.000
				<1,4	0.00	0.00	0.00	0.00	0.00	0.00	0.00	0.00	0.00	0.00	0.00	0.00	0.00	0.00	0.000
				Sum	100.00	10.04	89.96	**12.78**	**17.84**	**30.62**	100.00	100.00	100.00	19.12	13.57	15.44			
22.18		Feed	**100.00**	>3,0	99.48	6.23	93.77	12.84	25.26	38.09	100.00	100.00	100.00	100.00	100.00	100.00	100.00	100.00	100.00
				2,5	0.35	0.00	100.00	0.00	0.00	0.00	0.00	0.00	0.00	0.00	0.00	0.00	#DIV/0!	0.00	0.00
				1,4	0.17	0.00	100.00	0.00	0.00	0.00	0.00	0.00	0.00	0.00	0.00	0.00	0.00	0.00	0.00
				<1,4	0.00	0.00	0.00	0.00	0.00	0.00	0.00	0.00	0.00	0.00	0.00	0.00	0.00	0.00	0.00
				Sum	100.00	6.20	93.80	**12.77**	**25.12**	**37.89**	100.00	100.00	100.00	100.00	100.00	100.00			

Copper content in the feed (first sample)

Table 29 Copper content in the feed (first sample)

Sort.-Fluid	Size class		Sink/float		Susceptibility	Fractions				Content percentage						Density class Output%		
Mass percentage	Size class [mm]	Mass percentage	Density class [g/cm³]	Masse [%]	masses [%]					IO,j			IO,0					
$r_{m,Sort.-Fluid}$		$r_{m,j}$		$m_{i,j}$	$g_{j,MP}$	$g_{j,UMP}$	$g_{j,Cu}$	$g_{j,brass}$	$g_{j,Cu+brass,\ real}$	$r_{j,Cu}$	$r_{j,brass}$	$r_{j,Cu+brass,\ real}$	$r_{j,Cu}$ *	$r_{j,brass}$ *	$r_{j,Cu+brass,\ real}$ *	$r_{j,Cu}$ **	$r_{j,brass}$ **	$r_{j,Cu+brass,\ real}$ **
Feed	10/16mm	72.99	>3,0	24.56	5.30	94.70	12.78	26.86	39.63	100.00	100.00	100.00	80.88	86.43	84.56	80.88	86.43	84.56
			2.5	65.02	0.68	99.32	0.00	0.00	0.00	0.00	0.00	0.00	0.00	0.00	0.00	0.00	0.00	0.00
			1.4	9.45	2.93	97.07	0.00	0.00	0.00	0.00	0.00	0.00	0.00	0.00	0.00	0.00	0.00	0.00
			<1,4	0.97	0.00	100.00	0.00	0.00	0.00	0.00	0.00	0.00	0.00	0.00	0.00	0.00	0.00	0.00
			Sum	100.00	2.02	97.98	**3.14**	**6.60**	**9.74**	100.00	100.00	100.00	80.88	86.43	84.56			
	16/30mm	27.01	>3,0	16.49	9.55	90.45	12.16	16.97	29.13	100.00	100.00	100.00	19.12	13.57	15.44	19.12	13.57	15.44
			2.5	77.29	0.00	100.00	0.00	0.00	0.00	0.00	0.00	0.00	0.00	0.00	0.00	0.00	0.00	0.00
			1.4	6.06	0.00	100.00	0.00	0.00	0.00	0.00	0.00	0.00	0.00	0.00	0.00	0.00	0.00	0.00
			<1,4	0.15	0.00	100.00	0.00	0.00	0.00	0.00	0.00	0.00	0.00	0.00	0.00	0.00	0.00	0.00
			Sum	100.00	1.57	98.43	**2.01**	**2.80**	**4.80**	100.00	100.00	100.00	19.12	13.57	15.44			
100.00	Feed	**100.00**	>3,0	22.39	6.14	93.86	12.65	24.89	37.54	100.00	100.00	100.00	100.00	100.00	100.00	100.00	100.00	100.00
			2.5	68.33	0.47	99.53	0.00	0.00	0.00	0.00	0.00	0.00	0.00	0.00	0.00	0.00	0.00	0.00
			1.4	8.53	2.37	97.63	0.00	0.00	0.00	0.00	0.00	0.00	0.00	0.00	0.00	0.00	0.00	0.00
			<1,4	0.75	0.00	100.00	0.00	0.00	0.00	0.00	0.00	0.00	0.00	0.00	0.00	0.00	0.00	0.00
			Sum	100.00	1.90	98.10	**2.83**	**5.57**	**8.40**	100.00	100.00	100.00	100.00	100.00	100.00			

Density recovery for -16mm +10mm fraction (first sample)

Table 30 Density recovery for -16mm +10mm fraction (first sample)

Product	Mass	Mass	Density class	Mass	Density based recovery
		[%]	[g/cm^3]	[%]	[%]
Heavier fraction	1793.93	24.58		0	0
			>3	99.38	99.436
			3	0.40	0.151
			2.5	0.22	0.561
			1.4	0.00	0.000
			0	100.00	
Lighter fraction	5505.17	75.42		0.00	
			>3	0.18	0.56
			3	86.08	99.85
			2.5	12.45	99.44
			1.4	1.29	100.00
			0	100.00	
Feed	7299.10	100.00	> 3,0	24.56	
			2.5	65.02	
			1.4	9.45	
			< 1,4	0.97	
				100.00	

Density recovery for +16mm -30mm fraction (first sample)

Table 31 Density recovery for +16mm -30mm fraction (first sample)

Product	Mass	Mass	Density class	Mass	Density based recovery
		[%]	[g/cm^3]	[%]	[%]
Heavier fraction	423.81	15.69		0	
			>3	99.87	95.007
			3	0.13	0.026
			2.5	0.00	0.000
			1.4	0.00	0.000
			0	100.00	
Lighter fraction	2277.09	84.31		0.00	
			>3	0.98	4.99
			3	91.65	99.97
			2.5	7.19	100.00
			1.4	0.18	100.00
			0	100.00	
Feed	2700.90	100.00	> 3,0	16.49	
			2.5	77.29	
			1.4	6.06	
			< 1,4	0.15	
				100.00	

Mass distribution -16mm +10mm fraction (second sample)

Table 32 Mass distribution -16mm +10mm fraction (second sample)

Probe		Sink/Float		Susceptibility		Fractions		hand sort	XRF (non-hand sorted)		XRF
Size class	Product	Density class	Mass	Mass (g)							
[mm]		[g/cm^3]	[g]	MP	UMP	Copper	Cu fraction (XRF	brass	brass	Other	Cu in brass
10/16mm	Light fraction	> 3,0	5	0	5	0	0.00	0.00	0.00	0.00	0.00
		2.5	2343	16	2327	0	0.00	0.00	0.00	0.00	0.00
		1.4	339	10	329	0	0.00	0.00	0.00	0.00	0.00
		< 1,4	35	0	35	0	0.00	0.00	0.00	0.00	0.00
		Sum	2722	26	2696	0	0.00	0.00	0.00	0.00	0.00
	Heavy fraction	> 3,0	5239.21	247	4992.21	697.84	662.948	1778	754.49	1761.88	1327.1299
		2.5	31	0	31	0	0.00	0.00	0.00	0.00	0
		1.4	0	0	0	0	0.00	0.00	0.00	0.00	0
		< 1,4	0	0	0	0	0.00	0.00	0.00	0.00	0
		SUm	5270.21	247	5023.21	697.84	662.948	1778	754.49	1761.88	1327.1299

Mass distribution +16mm -30mm fraction (second sample)

Table 33 Mass distribution +16mm -30mm fraction (second sample)

Probe		Sink/Float		Susceptibility		Fractions		hand sort	XRF (non-hand sorted)		XRF
Size calss	Product	Density calss	Mass	Mass (g)							
[mm]		[g/cm^3]	[g]	MP	UMP	Copper	Cu fraction (XRF)	brass	brass	Other	Cu in brass
16/30mm	Light fraction	> 3,0	11	0	11	0	0.00	0.00	0.00	0.00	0.00
		2.5	1032	0	1032	0	0.00	0.00	0.00	0.00	0.00
		1.4	81	0	81	0	0.00	0.00	0.00	0.00	0.00
		< 1,4	2	0	2	0	0.00	0.00	0.00	0.00	0.00
		Sum	1126	0	1126	0	0.00	0.00	0.00	0.00	0.00
	Heavy fraction	> 3,0	1471.5	59	1412.5	197	189.12	409.31	170.9	635.29	312.9546
		2.5	4	0	4	0	0	0	0	0	0
		1.4	0	0	0	0	0	0	0	0	0
		< 1,4	0	0	0	0	0	0	0	0	0
		Sum	1475.5	59	1416.5	197	189.12	409.31	170.9	635.29	312.9546

Copper content in heavier fraction (second sample)

Table 34 Copper content in heavier fraction (second sample)

Sort - Fluid	Size class		Sink/float	Susceptibility	Fractions				Content percentage						Density class Output%			
Mass percentage	Size class	Mass per class	Density class	Masse [%]	masses [%]				I0,j				I0,0					
$r_{m,Sort-Fluid}$	[mm]	$r_{m,j}$	[g/cm³]	$m_{i,j}$	$g_{i,WP}$	$g_{i,UWP}$	$g_{i,Cu}$	$g_{i,brass}$	$g_{i,Cu+brass\ real}$	$r_{i,Cu}$	$r_{i,brass}$	$r_{i,Cu+brass\ real}$	$r_{i,Cu}$ *	$r_{i,brass}$ *	$r_{i,Cu+brass\ real}$ *	$r_{i,Cu}$ **	$r_{i,brass}$ **	$r_{i,Cu+brass\ real}$ *
Heavy fraction	10/16mm	78.13	>3,0	99.41	4.71	95.29	13.28	26.58	39.86	100.00	100.00	100.00	77.93	81.03	79.98	77.93	81.03	79.98
			2.5	0.59	0.00	100.00	0.00	0.00	0.00	0.00	0.00	0.00	0.00	0.00	0.00	0.00	0.00	0.00
			1.4	0.00	0.00	0.00	0.00	0.00	0.00	0.00	0.00	0.00	0.00	0.00	0.00	0.00	0.00	0.00
			<1,4	0.00	0.00	0.00	0.00	0.00	0.00	0.00	0.00	0.00	0.00	0.00	0.00	0.00	0.00	0.00
			Sum	100.00	4.69	95.31	**13.20**	**26.43**	**39.63**	100.00	100.00	100.00	77.93	81.03	79.98			
	16/30mm	21.87	>3,0	99.73	4.01	95.99	13.39	22.16	35.55	100.00	100.00	100.00	22.07	18.97	20.02	22.07	18.97	20.02
			2.5	0.27	0.00	100.00	0.00	0.00	0.00	0.00	0.00	0.00	0.00	0.00	0.00	0.00	0.00	0.000
			1.4	0.00	0.00	0.00	0.00	0.00	0.00	0.00	0.00	0.00	0.00	0.00	0.00	0.00	0.00	0.000
			<1,4	0.00	0.00	0.00	0.00	0.00	0.00	0.00	0.00	0.00	0.00	0.00	0.00	0.00	0.00	0.000
			Sum	100.00	4.00	96.00	**13.35**	**22.10**	**35.45**	100.00	100.00	100.00	22.07	18.97	20.02			
22.18	Feed	**100.00**	>3,0	99.48	4.56	95.44	13.30	25.61	38.92	100.00	100.00	100.00	100.00	100.00	100.00	100.00	100.00	100.00
			2.5	0.52	0.00	100.00	0.00	0.00	0.00	0.00	0.00	0.00	0.00	0.00	0.00	0.00	0.00	0.00
			1.4	0.00	0.00	0.00	0.00	0.00	0.00	0.00	0.00	0.00	0.00	0.00	0.00	0.00	0.00	0.00
			<1,4	0.00	0.00	0.00	0.00	0.00	0.00	0.00	0.00	0.00	0.00	0.00	0.00	0.00	0.00	0.00
			Sum	100.00	4.54	95.46	**13.23**	**25.48**	**38.71**	100.00	100.00	100.00	100.00	100.00	100.00			

Copper content in the feed of the second sample

Table 35 Copper content in the feed of the second sample

Sort.-Fluid	Size class		Sink/float	Susceptibility	Fractions				Content percentage						Density class Output%		
Mass percentage	Size class	Mass per.	Density class	Masse [%]	masses [%]				$I0_i$			$I0,0$					
$r_{m,Sort+Fluid}$	[mm]	$r_{m,i}$	[g/cm³]	$m_{i,}$	$\chi_{i,MP}$	$\chi_{i,MP}$	$\chi_{i,Cu}$	$\chi_{i,brass}$	$\chi_{i,Cu+brass\_real}$	$r_{i,Cu}$	$r_{i,brass}$	$r_{i,Cu+brass\_real}$	$r_{i,Cu}$ *	$r_{i,brass}$ *	$r_{i,Cu+brass\_real}$ *	$r_{i,Cu}$ **	$r_{i,brass}$ **	$r_{i,Cu+brass\_real}$ **
Feed	10/16mm	72.38	>3,0	23.94	4.69	95.31	13.20	26.43	39.63	100.00	100.00	100.00	77.93	81.03	79.98	77.93	81.03	79.98
			2.5	65.61	0.68	99.32	0.00	0.00	0.00	0.00	0.00	0.00	0.00	0.00	0.00	0.00	0.00	0.00
			1.4	9.47	2.95	97.05	0.00	0.00	0.00	0.00	0.00	0.00	0.00	0.00	0.00	0.00	0.00	0.00
			<1,4	0.98	0.00	100.00	0.00	0.00	0.00	0.00	0.00	0.00	0.00	0.00	0.00	0.00	0.00	0.00
			Sum	100.00	1.85	98.15	**3.16**	**6.33**	**9.49**	100.00	100.00	100.00	77.93	81.03	79.98			
	16/30mm	27.62	>3,0	18.32	3.83	96.17	12.80	21.18	33.98	100.00	100.00	100.00	22.07	18.97	20.02	22.07	18.97	20.02
			2.5	75.61	0.00	100.00	0.00	0.00	0.00	0.00	0.00	0.00	0.00	0.00	0.00	0.00	0.00	0.00
			1.4	5.93	0.00	100.00	0.00	0.00	0.00	0.00	0.00	0.00	0.00	0.00	0.00	0.00	0.00	0.00
			<1,4	0.15	0.00	100.00	0.00	0.00	0.00	0.00	0.00	0.00	0.00	0.00	0.00	0.00	0.00	0.00
			Sum	100.00	0.70	99.30	**2.34**	**3.88**	**6.22**	100.00	100.00	100.00	22.07	18.97	20.02			
100.00	Feed	**100.00**	>3,0	22.39	4.49	95.51	13.11	25.24	38.35	100.00	100.00	100.00	100.00	100.00	100.00	100.00	100.00	100.00
			2.5	68.37	0.47	99.53	0.00	0.00	0.00	0.00	0.00	0.00	0.00	0.00	0.00	0.00	0.00	0.00
			1.4	8.49	2.38	97.62	0.00	0.00	0.00	0.00	0.00	0.00	0.00	0.00	0.00	0.00	0.00	0.00
			<1,4	0.75	0.00	100.00	0.00	0.00	0.00	0.00	0.00	0.00	0.00	0.00	0.00	0.00	0.00	0.00
			Sum	100.00	1.53	98.47	**2.94**	**5.65**	**8.59**	100.00	100.00	100.00	100.00	100.00	100.00			

Density recovery for -16mm +10mm fraction (Second sample)

Table 36 Density recovery for -16mm +10mm fraction (Second sample)

Product	Mass	Mass	Density class	Mass	Density based recovery
		[%]	[g/cm^3]	[%]	[%]
Heavier fraction	1732.72	23.94		0	
			>3	99.41	99.416
			3	0.59	0.215
			2.5	0.00	0.000
			1.4	0.00	0.000
			0	100.00	
Lighter fraction	5505.17	76.06		0.00	
			3	0.18	0.58
			2.5	86.08	99.79
			1.4	12.45	100.00
			0	1.29	100.00
				100.00	
Feed	7237.89	100.00	> 3,0	23.94	
			2.5	65.61	
			1.4	9.47	
			< 1,4	0.98	
				100.00	

Density recovery for +16mm -30mm fraction (Second sample)

Table 37 Density recovery for +16mm -30mm fraction (Second sample)

Product	Mass	Mass	Density class	Mass	Density based recovery
		[%]	[g/cm^3]	[%]	[%]
Heavier fraction	485.02	17.56		0	
			>3	99.73	95.603
			3	0.27	0.063
			2.5	0.00	0.000
			1.4	0.00	0.000
			0	100.00	
Lighter fraction	2277.09	82.44		0.00	
			3	0.98	4.40
			2.5	91.65	99.94
			1.4	7.19	100.00
			0	0.18	100.00
				100.00	
Feed	2762.11	100.00	> 3,0	18.32	
			2.5	75.61	
			1.4	5.93	
			< 1,4	0.15	
				100.00	

Mass distribution of -16mm +10mm (third sample)

Table 38 Mass distribution of -16mm +10mm (third sample)

Probe		Sink/Float		Susceptibility		Fractions		hand sort	XRF (non-hand sorted)		XRF
Size class	Product	Density class	Mass	Mass (g)							
[mm]		[g/cm^3]	[g]	MP	UMP	Copper	Cu fraction (XRF)	brass	brass	Other	Cu in brass
10/16mm	Light fraction	> 3,0	5	0	5	0	0.00	0.00	0.00	0.00	0.00
		2.5	2343	16	2327	0	0.00	0.00	0.00	0.00	0.00
		1.4	339	10	329	0	0.00	0.00	0.00	0.00	0.00
		< 1,4	35	0	35	0	0.00	0.00	0.00	0.00	0.00
		Sum	2722	26	2696	0	0.00	0.00	0.00	0.00	0.00
	Heavy fraction	> 3,0	3034.1	247	2787.1	473	444.62	1006.17	500.74	807.19	838.956
		2.5	13	0	13	0	0.00	0.00	0.00	0.00	0
		1.4	0	0	0	0	0.00	0.00	0.00	0.00	0
		< 1,4	0	0	0	0	0.00	0.00	0.00	0.00	0
		SUm	3047.1	247	2800.1	473	444.62	1006.17	500.74	807.19	838.956

Mass distribution of +16mm -30mm (third sample)

Table 39 Mass distribution of +16mm -30mm (third sample)

Probe		Sink/Float		Susceptibility		Fractions		hand sort	XRF (non-hand sorted)		XRF
Size calss	Product	Density calss	Mass	Mass (g)							
[mm]		[g/cm^3]	[g]	MP	UMP	Copper	Cu fraction (XRF)	brass	brass	Other	Cu in brass
16/30mm	ight fractio	> 3,0	11	0	11	0	0.00	0.00	0.00	0.00	0.00
		2.5	1032	0	1032	0	0.00	0.00	0.00	0.00	0.00
		1.4	81	0	81	0	0.00	0.00	0.00	0.00	0.00
		< 1,4	2	0	2	0	0.00	0.00	0.00	0.00	0.00
		Sum	1126	0	1126	0	0.00	0.00	0.00	0.00	0.00
	eavy fractio	> 3,0	935.22	197	738.22	142	131.492	169.16	25.91	401.15	99.2266
		2.5	1	0	1	0	0	0	0	0	0
		1.4	0	0	0	0	0	0	0	0	0
		< 1,4	0	0	0	0	0	0	0	0	0
		Sum	936.22	197	739.22	142	131.492	169.16	25.91	401.15	99.2266

Copper content in heavier fractions (third sample)

Table 40 Copper content in heavier fractions (third sample)

Sort - Fluid	Size class		Sink/float	Susceptibility	Fractions				Content percentage						Density class		
					masses [%]				$l0_{,j}$			$l0,0$			Output%		
Mass percentage	Size class	Mass perc	Density class	Masse [%]													
$r_{m,Sort-Fluid}$	[mm]	$r_{m,j}$	[g/cm³]	m_{sj}	$g_{j,LMP}$	$g_{j,UMP}$	$g_{j,Cu}$	$g_{j,brass}$	$g_{j,CuHebrass\_real}$	$r_{j,Cu}$	$r_{j,brass}$	$r_{j,CuHebrass\_real}$	$r_{j,Cu}$ *	$r_{j,brass}$ *	$r_{j,CuHebrass\_real}$ *	$r_{j,Cu}$ **	$r_{j,brass}$ **	$r_{j,CuHebrass\_real}$ *
Heavyfraction	10/16mm	76.50	>3,0	99.57	8.14	91.86	15.95	30.10	46.05	100.00	100.00	100.00	74.40	87.90	82.70	74.40	87.90	82.70
			2.5	0.43	0.00	100.00	0.00	0.00	0.00	0.00	0.00	0.00	0.00	0.00	0.00	0.00	0.00	0.00
			1.4	0.00	0.00	0.00	0.00	0.00	0.00	0.00	0.00	0.00	0.00	0.00	0.00	0.00	0.00	0.00
			<1,4	0.00	0.00	0.00	0.00	0.00	0.00	0.00	0.00	0.00	0.00	0.00	0.00	0.00	0.00	0.00
			Sum	100.00	8.11	91.89	**15.88**	**29.97**	**45.86**	100.00	100.00	100.00	74.40	87.90	82.70			
	16/30mm	23.50	>3,0	99.89	21.06	78.94	17.81	13.44	31.25	100.00	100.00	100.00	25.60	12.10	17.30	25.60	12.10	17.30
			2.5	0.11	0.00	100.00	0.00	0.00	0.00	0.00	0.00	0.00	0.00	0.00	0.00	0.00	0.00	0.000
			1.4	0.00	0.00	0.00	0.00	0.00	0.00	0.00	0.00	0.00	0.00	0.00	0.00	0.00	0.00	0.000
			<1,4	0.00	0.00	0.00	0.00	0.00	0.00	0.00	0.00	0.00	0.00	0.00	0.00	0.00	0.00	0.000
			Sum	100.00	21.04	78.96	**17.79**	**13.43**	**31.22**	100.00	100.00	100.00	25.60	12.10	17.30			
22.18	Feed	**100.00**	>3,0	99.65	11.19	88.81	16.39	26.18	42.57	100.00	100.00	100.00	100.00	100.00	100.00	100.00	100.00	100.00
			2.5	0.35	0.00	100.00	0.00	0.00	0.00	0.00	0.00	0.00	0.00	0.00	0.00	0.00	0.00	0.00
			1.4	0.00	0.00	0.00	0.00	0.00	0.00	0.00	0.00	0.00	0.00	0.00	0.00	0.00	0.00	0.00
			<1,4	0.00	0.00	0.00	0.00	0.00	0.00	0.00	0.00	0.00	0.00	0.00	0.00	0.00	0.00	0.00
			Sum	100.00	11.15	88.85	**16.33**	**26.08**	**42.42**	100.00	100.00	100.00	100.00	100.00	100.00			

Copper content in the feed for the third sample

Table 41 Copper content in the feed for the third sample

Sort - Fluid	Mass percentage	Size class	Sink/float	Susceptibility	Fractions					Content percentage						Density class Output%		
					masses [%]				IO,j			IO,0						
$r_{m,Sort-Fluid}$	Size class [mm]	Mass perce r_{mj}	Density class [g/cm³]	Masse [%] m_{ij}	$\delta_{i,HP}$	$\delta_{i,LHP}$	$\delta_{i,Cu}$	$\delta_{i,brass}$	$\delta_{i,Cu+brass\_real}$	$r_{i,Cu}$	$r_{i,brass}$	$r_{i,Cu+brass\_real}$	$r_{i,Cu}$ *	$r_{i,brass}$ *	$r_{i,Cu+brass\_real}$ *	$r_{i,Cu}$ **	$r_{i,brass}$ **	$r_{i,Cu+brass\_real}$ **
Feed	10/16mm	72.02	>3,0	23.60	8.09	91.91	15.86	29.92	45.78	100.00	100.00	100.00	74.40	87.90	82.70	74.40	87.90	82.70
			2.5	65.90	0.68	99.32	0.00	0.00	0.00	0.00	0.00	0.00	0.00	0.00	0.00	0.00	0.00	0.00
			1.4	9.52	2.95	97.05	0.00	0.00	0.00	0.00	0.00	0.00	0.00	0.00	0.00	0.00	0.00	0.00
			<1,4	0.98	0.00	100.00	0.00	0.00	0.00	0.00	0.00	0.00	0.00	0.00	0.00	0.00	0.00	0.00
			Sum	100.00	2.64	97.36	**3.74**	**7.06**	**10.80**	100.00	100.00	100.00	74.40	87.90	82.70			
	16/30mm	27.98	>3,0	19.40	20.20	79.80	17.08	12.89	29.97	100.00	100.00	100.00	25.60	12.10	17.30	25.60	12.10	17.30
			2.5	74.60	0.00	100.00	0.00	0.00	0.00	0.00	0.00	0.00	0.00	0.00	0.00	0.00	0.00	0.00
			1.4	5.85	0.00	100.00	0.00	0.00	0.00	0.00	0.00	0.00	0.00	0.00	0.00	0.00	0.00	0.00
			<1,4	0.14	0.00	100.00	0.00	0.00	0.00	0.00	0.00	0.00	0.00	0.00	0.00	0.00	0.00	0.00
			Sum	100.00	3.92	96.08	**3.31**	**2.50**	**5.81**	100.00	100.00	100.00	25.60	12.10	17.30			
100.00	Feed	**100.00**	>3,0	22.42	11.02	88.98	16.15	25.80	41.95	100.00	100.00	100.00	100.00	100.00	100.00	100.00	100.00	100.00
			2.5	68.33	0.47	99.53	0.00	0.00	0.00	0.00	0.00	0.00	0.00	0.00	0.00	0.00	0.00	0.00
			1.4	8.49	2.38	97.62	0.00	0.00	0.00	0.00	0.00	0.00	0.00	0.00	0.00	0.00	0.00	0.00
			<1,4	0.75	0.00	100.00	0.00	0.00	0.00	0.00	0.00	0.00	0.00	0.00	0.00	0.00	0.00	0.00
			Sum	100.00	3.00	97.00	**3.62**	**5.78**	**9.41**	100.00	100.00	100.00	100.00	100.00	100.00			

Density recovery for -16mm +10mm fraction (Third sample)

Table 42 Density recovery for -16mm +10mm fraction (Third sample)

Product	Mass	Mass	Density class	Mass	Density based recovery
		[%]	[g/cm^3]	[%]	[%]
Heavier fraction	1696.57	23.56		0	
			>3	99.57	99.405
			3	0.43	0.153
			2.5	0.00	0.000
			1.4	0.00	0.000
			0	100.00	
Lighter fraction	5505.17	76.44		0.00	
			3	0.18	0.60
			2.5	86.08	99.85
			1.4	12.45	100.00
			0	1.29	100.00
				100.00	
Feed	7201.74	100.00	> 3,0	23.60	
			2.5	65.90	
			1.4	9.52	
			< 1,4	0.98	
				100.00	

Density recovery for +16mm -30mm fraction (Third sample)

Table 43 Density recovery for +16mm -30mm fraction (Third sample)

Product	Mass	Mass	Density class	Mass	Density based recovery
		[%]	[g/cm^3]	[%]	[%]
Heavier fraction	521.17	18.62		0	
			>3	99.89	95.902
			3	0.11	0.027
			2.5	0.00	0.000
			1.4	0.00	0.000
			0	100.00	
Lighter fraction	2277.09	81.38		0.00	
			3	0.98	4.10
			2.5	91.65	99.97
			1.4	7.19	100.00
			0	0.18	100.00
				100.00	
Feed	2798.26	100.00	> 3,0	19.40	
			2.5	74.60	
			1.4	5.85	
			< 1,4	0.14	
				100.00	

Mass distribution -90mm +30mm sample

Table 44 Mass distribution -90mm +30mm sample

[mm]	Fraction	density [g/cm^3]	Mass [g]	MP	UMP	Copper	Cu fraction (XRF)	Hand sort brass	XRF brass	Other	Cu in brass
30/80mm	Light fraction	>3.0	155.81	92.15	63.66	6.64	0	0.00	0.00	0.00	0.00
		2.5	5250	0	5250	0	0	0.00	0.00	0.00	0.00
		1.4	1574.93	0	1574.93	0	0	0.00	0.00	0.00	0.00
		<1.4	75.01	0	75.01	0	0	0.00	0.00	0.00	0.00
		Sum	7055.75	92.15	6963.6	6.64	0	0.00	0.00	0.00	0.00
	Heavy fraction	>3.0	7231.81	520	6711.81	1714.23	1559.9493	1886.73	1067.73	2042.4	1590.4338
		2.5	53.83	0	53.83	0	0	0.00	0.00	0.00	0
		1.4	19.34	0	19.34	0	0	0.00	0.00	0.00	0
		<1.4	0	0	0	0	0	0.00	0.00	0.00	0
		SUm	7304.98	520	6784.98	1714.23	1559.9493	1886.73	1067.73	2042.4	1590.4338

Density recovery of +30mm -90mm sample

Table 45 Density recovery of +30mm -90mm sample

Product	Mass	Mass	Density class	Mass	ty based re
		[%]	[g/cm^3]	[%]	[%]
Heavier fraction	20.17	20.17		0	
			>3	99.00	91.904
			3	0.74	0.250
			2.5	0.26	0.299
			1.4	0.00	0.000
			0	100.00	
Lighter fraction	79.83	79.83		0.00	
			>3	2.21	8.11
			3	74.41	99.75
			2.5	22.32	99.70
			1.4	1.06	100.00
			0	100.00	
Feed	100.00	100.00	3	21.73	
			2.5	59.55	
			1.4	17.87	
			0	0.85	
				100.00	

Copper content in -90mm +30mm fraction

Table 46 Copper content in -90mm +30mm fraction

Sort - Fluid																						
																					Density class Output%	
	product	Mass percentage	Sink/float	Susceptibility			Fractions						Content percentage									
							masses[%]						I0,j				I0,0					
		$r_{m,j}$	Density class [g/cm³]	$m_{j,j}$ mass [%]	$\delta_{L,WP}$	$\delta_{L,UWP}$	$\delta_{L,Cu}$	$\delta_{L,brass}$	$\delta_{L,Cu+brass,real}$	$r_{I,Cu}$	$r_{I,brass}$	$r_{I,Cu+brass,real}$	$r_{I,Cu}$ *	$r_{I,brass}$ *	$r_{I,Cu+brass,real}$ *	$r_{I,Cu}$ **	$r_{I,brass}$ **	$r_{I,Cu+brass,real}$ *
Fraction	Light fraction	79.83	>3,0	2.21	59.14	40.86	10.43	0.00	10.43	100.00	0.00	100.00	3.81	0.00	1.92	3.81	0.00	1.92
			2.5	74.41	0.00	100.00	0.00	0.00	0.00	0.00	0.00	0.00	0.00	0.00	0.00	0.00	0.00	0.00
			1.4	22.32	0.00	100.00	0.00	0.00	0.00	0.00	0.00	0.00	0.00	0.00	0.00	0.00	0.00	0.00
			<1,4	1.06	0.00	100.00	0.00	0.00	0.00	0.00	0.00	0.00	0.00	0.00	0.00	0.00	0.00	0.00
			Sum	100.00	1.31	98.69	0.23	0.00	0.23	100.00	0.00	100.00	3.81	0.00	1.92			
	heavy fraction	20.17	>3,0	99.00	7.19	92.81	23.24	23.70	46.94	100.00	100.00	100.00	96.19	100.00	98.08	96.19	100.00	98.08
			2.5	0.74	0.00	100.00	0.00	0.00	0.00	0.00	0.00	0.00	0.00	0.00	0.00	0.00	0.00	0.000
			1.4	0.26	0.00	100.00	0.00	0.00	0.00	0.00	0.00	0.00	0.00	0.00	0.00	0.00	0.00	0.000
			<1,4	0.00	0.00	0.00	0.00	0.00	0.00	0.00	0.00	0.00	0.00	0.00	0.00	0.00	0.00	0.000
			Sum	100.00	7.12	92.88	23.01	23.46	46.47	100.00	100.00	100.00	96.19	100.00	98.08			
	Feed	100.00	>3,0	21.73	11.41	88.59	22.20	21.77	43.98	100.00	100.00	100.00	100.00	100.00	100.00	100.00	100.00	100.00
			2.5	59.55	0.00	100.00	0.00	0.00	0.00	0.00	0.00	0.00	0.00	0.00	0.00	0.00	0.00	0.00
			1.4	17.87	0.00	100.00	0.00	0.00	0.00	0.00	0.00	0.00	0.00	0.00	0.00	0.00	0.00	0.00
			<1,4	0.85	0.00	100.00	0.00	0.00	0.00	0.00	0.00	0.00	0.00	0.00	0.00	0.00	0.00	0.00
			Sum	100.00	2.48	97.52	4.82	4,73	9.55	100.00	100.00	100.00	100.00	100.00	100.00			

Mass distribution of different fractions in eddy current magnetic reject sample

Table 47 Mass distribution of different fractions in eddy current magnetic reject sample

Eddy current magnetic separated feed			
10/16mm fraction			
Material	Mass		Percentage of each fraction
Ceramics	2155	g	31.24161877
Rubber	462	g	6.697739151
Metals	3626	g	52.56710424
Residual	385	g	5.581449292
Non magnetic fraction	111	g	1.609197069
Copper encooperated material	158.85	g	2.302891481
Sum	6897.85		100
16/30 mm fraction			
Material	Mass		Percentage of each fraction
Ceramics	644	g	24.20779611
Rubber	221	g	8.307333759
Cast metallic material	1425	g	53.56538736
Residual	183	g	6.87892343
Non magnetic fraction	35	g	1.315641093
Copper encooperated material	152.3	g	5.724918242
Sum	2660.3		100

XRF analysis of metallic fraction in eddy current magnetic reject sample

Table 48 XRF analysis of metallic fraction in eddy current magnetic reject sample

10/16mm magnetic metallic fraction					
XRF separation of non cast material	mass	%	XRF separation of cast material	mass	%
Iron and its alloys	1725	92.05	Iron and its alloys	1580.00	90.18
Aluminium with iron parts	28	1.49	Aluminium with iron parts	82.00	4.68
copper with iron parts	57	3.04	copper with iron parts	22.00	1.26
Nickel and its alloys	56	2.99	Zn and its alloys	68.00	3.88
others	8	0.43		1752.00	100.00
	1874	100.00			
16/30 mm magnetic metallic fraction					
XRF separation of non cast material	mass	%	XRF separation of cast material	mass	%
Iron and its alloys	633	98.91	Iron and its alloys	438.00	55.80
Aluminium with iron parts	4	0.63	Aluminium with iron parts	259.00	32.99
copper with iron parts	3	0.47	copper with iron parts	21.00	2.68
	640	100.00	Zn and its alloys	67.00	8.54
				785.00	100.00

Masses of different fractions are used for density measurements.

Table 49 Masses of different fractions are used for density measurements

	Total mass
Stone	285.42
Iron	903.05
Copper+iron	376.16
Al+iron	234.86
Zn+iron	122.12
Mg+iron	3.98
	1925.59

Density analysis of metallic fraction and stones in the sample

Table 50 Density analysis of magnetic metallic fraction and stones in the sample

Particle Nr.	mParticle+Water +Sieve [g]	mParticle [g]	Buoyancy [g]	DmWater [g]	VParticle [g]	Density [g/cm3]	
1	805.11	5.11	802	2	1.994	2.562688	stones
2	805.47	5.47	801.58	1.58	1.57526	3.472443	stones
3	803.21	3.21	801.26	1.26	1.25622	2.555285	stones
4	804.32	4.32	801.65	1.65	1.64505	2.62606	stones
5	803.7	3.7	801.26	1.26	1.25622	2.945344	stones
6	804.04	4.04	801.41	1.41	1.40577	2.87387	stones
7	802.53	2.53	801.02	1.02	1.01694	2.487856	stones
8	803.55	3.55	801.36	1.36	1.35592	2.618149	stones
9	803.75	3.75	801.29	1.29	1.28613	2.915724	stones
10	808.91	8.91	802.57	2.57	2.56229	3.477358	stones
11	807.28	7.28	801.88	1.88	1.87436	3.883992	stones
12	802.57	2.57	801.27	1.27	1.26619	2.029711	stones
13	804.2	4.2	801.19	1.19	1.18643	3.540032	stones
14	803.9	3.9	801.61	1.61	1.60517	2.429649	stones
15	803.24	3.24	800.93	0.93	0.92721	3.494354	stones
16	802.89	2.89	800.98	0.98	0.97706	2.957853	stones
17	807.53	7.53	802.12	2.12	2.11364	3.562575	stones
18	803.58	3.58	800.97	0.97	0.96709	3.701827	stones
19	802.91	2.91	800.95	0.95	0.94715	3.072375	stones
20	809.2	9.2	803.31	3.31	3.30007	2.78782	stones
21	810.06	10.06	802.97	2.97	2.96109	3.397398	stones
22	803.51	3.51	801.4	1.4	1.3958	2.514687	stones
23	802.67	2.67	800.83	0.83	0.82751	3.226547	stones
24	803.35	3.35	801.01	1.01	1.00697	3.326812	stones

25	803.6	3.6	800.64	0.64	0.63808	5.641926	stones
26	819.29	19.29	806.14	6.14	6.12158	3.151147	stones
27	806.63	6.63	802.86	2.86	2.85142	2.325157	stones
28	819.93	19.93	805.98	5.98	5.96206	3.342804	stones
29	809.05	9.05	803.4	3.4	3.3898	2.669774	stones
30	813.76	13.76	805.21	5.21	5.19437	2.649022	stones
31	815.2	15.2	804.13	4.13	4.11761	3.691462	stones
32	810.35	10.35	803.74	3.74	3.72878	2.775707	stones
33	807.71	7.71	802.84	2.84	2.83148	2.722958	stones
34	808.25	8.25	802.56	2.56	2.55232	3.232353	stones
35	808.76	8.76	802.5	2.5	2.4925	3.514544	stones
36	807.64	7.64	802.4	2.4	2.3928	3.192912	stones
37	807.62	7.62	803.22	3.22	3.21034	2.37358	stones
38	809.95	9.95	803.47	3.47	3.45959	2.876063	stones
39	806.96	6.96	802.91	2.91	2.90127	2.398949	stones
40	819.24	19.24	805.96	5.96	5.94212	3.237902	stones
41	803.9	3.9	800.76	0.76	0.75772	5.14702	non-cast iron
42	814.36	14.36	802.5	2.5	2.4925	5.761284	non-cast iron
43	810.51	10.51	801.81	1.81	1.80457	5.824102	non-cast iron
44	804.47	4.47	800.82	0.82	0.81754	5.467622	non-cast iron
45	804.78	4.78	800.7	0.7	0.6979	6.849119	non-cast iron
46	809.9	9.9	801.37	1.37	1.36589	7.248021	non-cast iron
47	807.58	7.58	801.39	1.39	1.38583	5.469646	non-cast iron
48	810.94	10.94	801.87	1.87	1.86439	5.867871	non-cast iron
49	804.49	4.49	800.84	0.84	0.83748	5.361322	non-cast iron
50	805.75	5.75	801.16	1.16	1.15652	4.971812	non-cast iron
51	806.54	6.54	801.78	1.78	1.77466	3.685213	non-cast iron
52	808.71	8.71	801.36	1.36	1.35592	6.423683	non-cast iron
53	805.26	5.26	800.99	0.99	0.98703	5.329119	non-cast iron
54	812.07	12.07	802.06	2.06	2.05382	5.876854	non-cast iron
55	812.37	12.37	801.73	1.73	1.72481	7.171804	non-cast iron
56	807.52	7.52	801.07	1.07	1.06679	7.049185	non-cast iron
57	804.8	4.8	800.95	0.95	0.94715	5.067835	non-cast iron
58	807.42	7.42	801.23	1.23	1.22631	6.050672	non-cast iron
59	807.75	7.75	801	1	0.997	7.77332	non-cast iron
60	805	5	800.93	0.93	0.92721	5.392522	non-cast iron
61	803.98	3.98	801.8	1.8	1.7946	2.217764	Mg particle
62	803.4	3.4	800.42	0.42	0.41874	8.119597	Copper
63	831.14	31.14	804.45	4.45	4.43665	7.018809	Iron cast material
64	825.12	25.12	803.6	3.6	3.5892	6.998774	Iron cast material
65	809.89	9.89	801.62	1.62	1.61514	6.123308	Iron cast material
66	828.92	28.92	803.85	3.85	3.83845	7.534291	Iron cast material

67	813.51	13.51	801.84	1.84	1.83448	7.364485	Iron cast material
68	809.7	9.7	801.54	1.54	1.53538	6.317654	Iron cast material
69	813.44	13.44	802.06	2.06	2.05382	6.543904	Iron cast material
70	819.63	19.63	803.21	3.21	3.20037	6.133666	Iron cast material
71	821.71	21.71	802.97	2.97	2.96109	7.33176	Iron cast material
72	828.95	28.95	803.97	3.97	3.95809	7.314134	Iron cast material
73	829.97	29.97	804.38	4.38	4.36686	6.863055	Iron cast material
74	830.38	30.38	804.39	4.39	4.37683	6.941097	Iron cast material
75	818.48	18.48	802.72	2.72	2.71184	6.814561	Iron cast material
76	819.99	19.99	802.75	2.75	2.74175	7.290964	Iron cast material
77	809.1	9.1	801.21	1.21	1.20637	7.543291	Iron cast material
78	818.84	18.84	806.5	6.5	6.4805	2.907183	Al+iron
79	812.87	12.87	804.64	4.64	4.62608	2.782053	Al+iron
80	814.89	14.89	805.06	5.06	5.04482	2.951542	Al+iron
81	816.4	16.4	805.26	5.26	5.24422	3.127252	Al+iron
82	808.94	8.94	803.37	3.37	3.35989	2.660801	Al+iron
83	820.18	20.18	806.95	6.95	6.92915	2.912334	Al+iron
84	808.16	8.16	802.44	2.44	2.43268	3.354325	Al+iron
85	824.5	24.5	808.62	8.62	8.59414	2.85078	Al+iron
86	821.22	21.22	806.34	6.34	6.32098	3.357074	Al+iron
87	816.98	16.98	806.12	6.12	6.10164	2.782858	Al+iron
88	807.83	7.83	802.69	2.69	2.68193	2.919539	Al+iron
89	828.24	28.24	806.42	6.42	6.40074	4.41199	Zn+iron
90	820.71	20.71	803.1	3.1	3.0907	6.700747	Zn+iron
91	806.97	6.97	801.72	1.72	1.71484	4.064519	Zn+iron
92	820.44	20.44	802.67	2.67	2.66199	7.678466	brass+iron
93	820.79	20.79	802.67	2.67	2.66199	7.809947	non-cast iron
94	811.17	11.17	801.53	1.53	1.52541	7.322621	non-cast iron
95	806.99	6.99	800.97	0.97	0.96709	7.227869	non-cast iron
96	812.35	12.35	801.66	1.66	1.65502	7.462145	non-cast iron
97	821.07	21.07	802.75	2.75	2.74175	7.684873	non-cast iron
98	814.7	14.7	801.93	1.93	1.92421	7.639499	non-cast iron
99	812.51	12.51	801.84	1.84	1.83448	6.819371	non-cast iron
100	810.75	10.75	801.37	1.37	1.36589	7.870326	non-cast iron
101	813.27	13.27	802.05	2.05	2.04385	6.492649	non-cast iron
102	818.04	18.04	802.38	2.38	2.37286	7.60264	non-cast iron
103	809.19	9.19	801.27	1.27	1.26619	7.257994	non-cast iron
104	811.78	11.78	801.55	1.55	1.54535	7.622869	non-cast iron
105	804.68	4.68	800.76	0.76	0.75772	6.176424	non-cast iron
106	815.69	15.69	802.11	2.11	2.10367	7.458394	non-cast iron
107	805.23	5.23	800.69	0.69	0.68793	7.602518	non-cast iron
108	813.44	13.44	801.84	1.84	1.83448	7.326327	non-cast iron

109	808.12	8.12	801.19	1.19	1.18643	6.844062	non-cast iron
110	806.17	6.17	800.99	0.99	0.98703	6.251076	non-cast iron
111	808.26	8.26	801.2	1.2	1.1964	6.904045	non-cast iron
112	813.29	13.29	801.82	1.82	1.81454	7.32417	non-cast iron
113	817.18	17.18	802.32	2.32	2.31304	7.427455	non-cast iron
114	805.75	5.75	800.7	0.7	0.6979	8.239003	non-cast iron
115	806.82	6.82	800.99	0.99	0.98703	6.909618	non-cast iron
116	809.92	9.92	801.37	1.37	1.36589	7.262664	non-cast iron
117	808.57	8.57	801.15	1.15	1.14655	7.474598	non-cast iron
118	810.1	10.1	801.37	1.37	1.36589	7.394446	non-cast iron
119	807.89	7.89	801.03	1.03	1.02691	7.683244	non-cast iron
120	805.56	5.56	800.7	0.7	0.6979	7.966757	non-cast iron
121	808.83	8.83	801.23	1.23	1.22631	7.200463	non-cast iron
122	813	13	801.95	1.95	1.94415	6.686727	non-cast iron
123	812.23	12.23	801.69	1.69	1.68493	7.258462	non-cast iron
124	812.4	12.4	801.95	1.95	1.94415	6.378109	non-cast iron
125	812.78	12.78	801.7	1.7	1.6949	7.540268	non-cast iron
126	816.67	16.67	802.53	2.53	2.52241	6.608759	non-cast iron
127	805.36	5.36	800.78	0.78	0.77766	6.892472	non-cast iron
128	807.6	7.6	800.96	0.96	0.95712	7.940488	non-cast iron
129	816.76	16.76	802.24	2.24	2.23328	7.504657	non-cast iron
130	809.62	9.62	801.41	1.41	1.40577	6.843225	non-cast iron
131	806.39	6.39	800.87	0.87	0.86739	7.366928	non-cast iron
132	802.66	2.66	801.41	1.41	1.40577	1.892201	non-cast iron
133	805.42	5.42	800.81	0.81	0.80757	6.711493	non-cast iron
134	807.81	7.81	802.81	2.81	2.80157	2.787723	Al+iron
135	804.33	4.33	801.49	1.49	1.48553	2.914785	Al+iron
136	806.62	6.62	802.68	2.68	2.67196	2.477582	Al+iron
137	806.33	6.33	802.3	2.3	2.2931	2.760455	Al+iron
138	803.53	3.53	801.02	1.02	1.01694	3.471198	Al+iron
139	804.53	4.53	801.84	1.84	1.83448	2.469365	Al+iron
140	805.03	5.03	801.8	1.8	1.7946	2.802853	Al+iron
141	806.19	6.19	802.31	2.31	2.30307	2.687717	Al+iron
142	804.21	4.21	801.55	1.55	1.54535	2.724302	Al+iron
143	803.66	3.66	801.35	1.35	1.34595	2.719269	Al+iron
144	801.83	1.83	800.73	0.73	0.72781	2.514392	Al+iron
145	803.09	3.09	801.07	1.07	1.06679	2.89654	Al+iron
146	803.99	3.99	801.49	1.49	1.48553	2.68591	Al+iron
147	802.9	2.9	801.01	1.01	1.00697	2.879927	Al+iron
148	827.57	27.57	804.34	4.34	4.32698	6.37165	Zn+iron
149	814.69	14.69	802.42	2.42	2.41274	6.088513	Zn+iron
150	808.05	8.05	801.53	1.53	1.52541	5.27727	Zn+iron

151	802.3	2.3	801.2	1.2	1.1964	1.922434	Zn+iron
152	803.85	3.85	800.53	0.53	0.52841	7.286009	Zn+iron
153	807.29	7.29	801.03	1.03	1.02691	7.098967	Zn+iron
154	802.45	2.45	800.4	0.4	0.3988	6.14343	Zn+iron
155	815.31	15.31	802.07	2.07	2.06379	7.41839	Cu+iron
156	803.09	3.09	800.61	0.61	0.60817	5.080816	Cu+iron
157	803.45	3.45	800.53	0.53	0.52841	6.529021	Cu+iron
158	801.25	1.25	800.2	0.2	0.1994	6.268806	Cu+iron
159	804.67	4.67	800.66	0.66	0.65802	7.097049	Cu+iron
160	805.32	5.32	800.85	0.85	0.84745	6.277656	Cu+iron
161	803.06	3.06	800.49	0.49	0.48853	6.263689	Cu+iron
162	803.75	3.75	800.64	0.64	0.63808	5.877006	Cu+iron
163	802.76	2.76	800.6	0.6	0.5982	4.613842	Cu+iron
164	803.65	3.65	800.45	0.45	0.44865	8.135518	Cu+iron
165	803.16	3.16	800.42	0.42	0.41874	7.546449	Cu+iron
166	803.28	3.28	800.65	0.65	0.64805	5.061338	Cu+iron
167	803.73	3.73	800.51	0.51	0.50847	7.335733	Cu+iron
1	1318.09	29.09	1293.3	4.3	4.2871	6.785473	Cu+iron
2	1295.31	6.31	1290.26	1.26	1.25622	5.023006	Hand-sorted copper
3	1300.31	11.31	1293.62	4.62	4.60614	2.455418	Hand-sorted copper
4	1320.57	31.57	1293.39	4.39	4.37683	7.212983	Hand-sorted copper
5	1294.9	5.9	1289.9	0.9	0.8973	6.575281	Hand-sorted copper
6	1302	13	1291.1	2.1	2.0937	6.209104	Hand-sorted copper
7	1310.15	21.15	1293	4	3.988	5.30341	Hand-sorted copper
8	1305.85	16.85	1292.26	3.26	3.25022	5.184264	Hand-sorted copper
9	1294.84	5.84	1291	2	1.994	2.928786	Hand-sorted copper
10	1300.52	11.52	1291.26	2.26	2.25322	5.112683	Hand-sorted copper
11	1304.85	15.85	1291.03	2.03	2.02391	7.831376	Hand-sorted copper
12	1304.34	15.34	1290.98	1.98	1.97406	7.770787	Hand-sorted copper
13	1296.42	7.42	1289.97	0.97	0.96709	7.672502	Hand-sorted copper
14	1298.58	9.58	1290.76	1.76	1.75472	5.45956	Hand-sorted copper
15	1303.9	14.9	1291.09	2.09	2.08373	7.150639	Hand-sorted copper
16	1295.11	6.11	1290	1	0.997	6.128385	Hand-sorted copper
17	1295.66	6.66	1289.89	0.89	0.88733	7.505663	Hand-sorted copper
18	1294.12	5.12	1290	1	0.997	5.135406	Hand-sorted copper
19	1295.98	6.98	1290.06	1.06	1.05682	6.60472	Hand-sorted copper
20	1297.81	8.81	1290.12	1.12	1.11664	7.889741	Hand-sorted copper
21	1291.74	2.74	1289.81	0.81	0.80757	3.392895	Hand-sorted copper
22	1296.89	7.89	1290.17	1.17	1.16649	6.763881	Hand-sorted copper
23	1294.89	5.89	1289.85	0.85	0.84745	6.950263	Hand-sorted copper
24	1291.27	2.27	1289.39	0.39	0.38883	5.838027	Hand-sorted copper
25	1290.03	1.03	1289.27	0.27	0.26919	3.826294	Hand-sorted copper

26	1293.75	4.75	1289.7	0.7	0.6979	6.806133	Hand-sorted copper
27	1292.75	3.75	1289.79	0.79	0.78763	4.761119	Hand-sorted copper
28	1293.01	4.01	1289.85	0.85	0.84745	4.731843	Hand-sorted copper
29	1291	2	1289.4	0.4	0.3988	5.015045	Hand-sorted copper
30	1291.74	2.74	1289.42	0.42	0.41874	6.54344	Hand-sorted copper
31	1292.25	3.25	1290	1	0.997	3.259779	Hand-sorted copper
32	1291.7	2.7	1289.4	0.4	0.3988	6.770311	Hand-sorted copper
33	1292.51	3.51	1289.54	0.54	0.53838	6.519559	Hand-sorted copper
		1925.59					

Mass distribution of material in density classes

Table 51 Mass distribution of material in density classes

mass	density	cumulative mass	% cumulative mass
4.96	1.75	4.96	0.257583
6.55	2	11.51	0.597739
50.1	2.25	61.61	3.199539
79.04	2.5	140.65	7.304255
195.3	2.75	274.34	14.24706
76.4	3	412.35	21.41422
89.86	3.25	502.21	26.08084
45.81	3.5	548.02	28.45985
8.31	3.75	556.33	28.8914
6.97	4	563.3	29.25337
28.24	4.25	591.54	30.71994
6.77	4.5	598.31	31.07152
9.5	4.75	607.81	31.56487
56.87	5	664.68	34.51825
65.58	5.25	730.26	37.92396
3.6	5.5	733.86	38.11092
53.9	5.75	782.8	40.65248
77.87	6	865.63	44.95401
87.45	6.25	953.08	49.49548
91.82	6.5	1044.9	54.26389
209.74	6.75	1254.64	65.15613
135.18	7	1389.82	72.17632
246.57	7.25	1636.39	84.98123
183.95	7.5	1820.34	94.53414
92.45	7.75	1912.79	99.33527
12.8	8	1925.59	100
1925.59			

Table 52 Mass of metallic material and stones use for density analysis

Density class	Mass of stones	mass of iron particles	Mass of iron+Cu composite	Mass of iron+Al composite	Mass of iron+Zn composite	Mass of mg+iron composite
1.75		2.66			2.3	
2	2.57					3.98
2.25	27.64		11.31	11.15		
2.5	50.22			28.82		
2.75	43.88		5.84	145.58		
3	60			16.4		
3.25	50.96		5.99	32.91		
3.5	39.27		1.03			
3.75	7.28	6.54				
4					6.97	
4.25					28.24	
4.5			6.77			
4.75		5.75	3.75			
5		8.7	48.17			
5.25		26.8	30.73		8.05	
5.5	3.6					
5.75		47.88	6.02			
6		41.62	19.11		17.14	
6.25		50.25	9.63		27.57	
6.5		48.53	22.58		20.71	
6.75		159.42	50.32			
7		76.75	51.14		11.14	
7.25		223.68	19.04			
7.5		146.27	9.82			
7.75		52.45	67.86			
8		5.75	7.05			
	285.42	903.05	376.16	234.86	122.12	3.98

8.1 Appendix 2

Table 53 Generic classification of copper and its alloys

Generic name	**UNS No.**	**Composition**
Wrought alloys		
Coppers(a)	C10100-C15815	>99% Cu
High-copper alloys(b)	C16200-C19900	>96% Cu
Brasses	C20100-C28000	Cu-Zn
Leaded brasses	C31200-C38500	Cu-Zn-Pb
Tin brasses	C40400-C48600	Cu-Zn-Sn-Pb
Phosphor bronzes	C50100-C52480	Cu-Sn-P
Leaded phosphor bronzes	C53400-C54400	Cu-Sn-Pb-P
Copper-phosphorus and copper-silver-phosphorus alloys(c)	C55180-C55284	Cu-P-Ag
Aluminum bronzes	C60800-C64210	Cu-Al-Ni-Fe-Si-Sn
Silicon bronzes	C64700-C66100	Cu-Si-Sn

Other copper-zinc alloys	C66300-C69710	Cu-Zn-Mn-Fe-Sn-Al-Si-Co
Copper nickels	C70100-C72950	Cu-Ni-Fe
Nickel silvers	C73500-C79830	Cu-Ni-Zn
Cast alloys		
Coppers(a)	C80100-C81200	>99% Cu
High-copper alloys(d)	C81400-C82800	>94% Cu
Red and leaded red brasses	C83300-C83810	Cu-Sn-Zn-Pb (82-94% Cu)
Semi-red and leaded semi-red brasses	C84200-C84800	Cu-Sn-Zn-Pb (75-82% Cu)
Yellow and leaded yellow brasses	C85200-C85800	Cu-Zn-Pb
Manganese bronzes and leaded manganese bronzes(e)	C86100-C86800	Cu-Zn-Mn-Fe-Pb
Silicon brasses/bronzes	C87300-C87800	Cu-Zn-Si
Copper-bismuth and copper-bismuth-selenium alloys	C89320-C89940	Cu-Sn-Zn-Bi-Se
Tin bronzes	C90200-C91700	Cu-Sn-Zn
Leaded tin bronzes	C92200-C94500	Cu-Sn-Zn-Pb
Nickel-tin bronzes	C94700-C94900	Cu-Ni-Sn-Zn-Pb
Aluminum bronzes	C95200-C95900	Cu-Al-Fe-Ni
Copper nickels	C96200-C96950	Cu-Ni-Fe
Nickel silvers	C97300-C97800	Cu-Ni-Zn-Pb-Sn
Leaded coppers	C98200-C98840	Cu-Pb
Special alloys	C99300-C99750	Cu-Zn-Mn-Al-Fe-Co-Sn-Pb

(D. J.R. Davis, 2001)

Table 54 European specification on the quality of the copper and its alloy scrap

ID	**Type**	**Source**	**Cu content according to EN 12861**	**Metal content according to EN 12861**	**Foreign materials according to the ECI (% (m/m))**	
					Total	**Thereof humidity (moisture, oil, emulsion, etc)**
B.1	S-Cu-1	Production scrap from P-free electrolytic copper	99.9	-	max. 0.25	max. 0.2

B.2	S-Cu-2	Old scrap from P-free pure electrolytic copper	99.9	-	max. 0.25	max. 0.2
B.3	S-Cu-3	Lacquered wire, P-free	99.9	-	lacquer + humidity	max. 0.2
B.4	S-Cu-4	Production scrap from tubes, sheets, coils, etc., pure copper, P-containing	99.9	-	max0.25	max. 0.2
B.5	S-Cu-5	Old scrap from tubes, sheets, coils etc., pure copper, P-containing	99.9	-	max0.25	max. 0.2
B.6	S-Cu-6	Old scrap from fire-stripped coated wires, pure copper	99.7	>98.5	max. 1.5	max. 0.2
B.7	S-Cu-7	Old scrap from varying copper products may contain non-metallic sediments	99.5	>98	max. 2.0	max. 0.2
B.8	S-Cu-8	Old scrap from varying copper products, no radiators or vessels	98	>96	max. 4.0	max. 0.2
B.9	S-Cu-9	Old scrap, which does not fit into categories B.1 to B.8 due to enhanced impurities, emulsion impurities should be within limits after melting	96	>92	max. 8.0	max. 0.2
B.10	S-Cu-10	Chopped copper wire, coated and uncoated	min. 97.5 (S-Cu-10D) to min. 99.90 (S-Cu-10A)	-	max. 0.4	max. 0.2
C.1	S-CuZn-1	Production scrap from copper-zinc alloy (CuZn5 to CuZn40), lead-free, iron-free, coated material depends on the agreement	63.5	-	max. 0.25	max. 0.2
C.2	S-CuZn-2	Copper-zinc alloy scrap from shells without primer, coated material depends on the agreement	69	-	max. 0.25	max. 0.2

C.3	S-CuZn-3	Copper-zinc alloy scrap from cartridges	69	-	max. 0.25	max. 0.2
C.4	S-CuZn-4	Copper-zinc-lead alloy scrap does not contain other alloys and is free of iron	57	-	max. 0.25	max. 0.2
C.5	S-CuZn-5	Turnings from copper-zinc-lead alloys do not contain other alloys and free iron	57 and min 91% metal yield	-	max. 9	max. 7
C.6	S-CuZn-6	Valves and taps from copper-zinc alloys, chromium and nickel coating shall be accepted, no manganese and silicon-bearing brass and free iron	57	>97	max. 3[1]	max. 0.2
C.7	S-CuZn-7	Scrap from copper-zinc alloys, varying sources, no aluminum, manganese, and silicon-bearing alloy	57	>95	max. 5	max. 0.2

(Muchová et al., n.d.) (***Source: ECI, 2010)***